Drag Measurements on a Laminar Flow Body of Revolution in Langley's 13" Magnetic Suspension and Balance System

by

David A. Dress

BS in Aerospace and Ocean Engineering
Virginia Polytechnic Institute & State University
1981

A Thesis submitted to
the Faculty of
The School of Engineering and Applied Science
of The George Washington University in partial satisfaction
of the requirements for the degree of Master of Science

April 1988

Abstract

Low-speed wind tunnel drag force measurements were taken on a laminar flow body of revolution free of support interference. This body was tested at zero incidence in the NASA Langley 13″ Magnetic Suspension and Balance System. The primary objective of these tests was to substantiate the drag force measuring capabilities of the 13″ MSBS. A secondary objective was to obtain support interference free drag measurements on an axisymmetric body of interest.

Both objectives were met. The drag force calibrations and wind-on repeatability data provide a means of assessing the drag force measuring capabilities of the 13″ MSBS. The measured drag coefficients for this body are of interest to researchers actively involved in designing minimum drag fuselage shapes.

Additional investigations included:

a) the effects of fixing transition

b) the effects of fins installed in the tail

c) surface flow visualizations using both liquid crystals and oil flow and

d) base pressure measurements using a one-channel telemetry system.

Two drag prediction codes were used to assess their usefulness in estimating overall body drag. These theoretical results did not compare well with the measured values because of the following:

a) incorrect or non-existent modeling of a laminar separation bubble on the body and

b) incorrect or non-existent estimates of base pressure drag

Acknowledgements

The author extends his gratitude to the NASA Langley Research Center for supporting this thesis. Special thanks go to all of the members of the MSBS research team at Langley. This includes Bob Kilgore, Rich Boyden, Colin Britcher, Bill Johnson, Pierce Lawing, Charles Alcorn, and Phil Arcara. Your continual support throughout these tests is greatly appreciated. Appreciation is also expressed to my advisor, Dr. John Whitesides, Professor, The George Washington University, for his support during this project.

Table of Contents

List of Tables

List of Figures

a	speed of sound, ft/sec
A_m	maximum cross-sectional area of model, in^2
b	tunnel width, in
C_f	skin-friction coefficient
C_D	drag coefficient
C_{D0}	drag coefficient at zero lift
C'_{D0}	afterbody drag coefficient at zero angle of attack
C_m	pitching moment coefficient
C_{n_r}	yaw damping coefficient
$C_{p,\ base}$	base pressure coefficient
D	drag force, $grams_f$
h	tunnel height, in
i_t	incidence angle of tail, deg
I	electromagnet current, amperes
k	height of roughness particles, in
l	length, in
L	model length, in
M	free-stream Mach number
p	pressure, $\frac{lb}{ft^2}$
q	dynamic pressure, $\frac{lb}{ft^2}$
R	Reynolds number
R_k	Reynolds number based on roughness height and local flow conditions at top of roughness
$R_{x'}$	Reynolds number based on x′ and on conditions outside boundary layer

s	distance along body contour, in
S	reference area, in^2
t	maximum model thickness, in
T	temperature, ^oR
v	local surface velocity, $\frac{ft}{sec}$
V	free-stream velocity, $\frac{ft}{sec}$
x	body abcissa, in
x′	distance from tip of model nose to roughness station, in
z	body ordinate, in
$\mathfrak{R}$	gas constant for air, $\frac{ft^2}{sec^2\ ^oR}$
α	angle of attack, deg
β	$\sqrt{1 - M^2}$
γ	ratio of specific heats
Δ	prefix denoting change in value
ϵ	blockage factor
η_k	nondimensional height in boundary layer based on roughness height, $\frac{k}{2x'}\sqrt{R_{x'}}$
λ	body shape factor
μ	viscosity, $\frac{lb_f\ sec}{ft^2}$
ρ	density, $\frac{slugs}{ft^3}$
τ	tunnel shape parameter

Subscripts:

b	due to blockage
base	measured at base of model
B	due to buoyancy
c	corrected value
L	based on model length

o	based on zero axial load
s	static condition
s′	due to solid blockage
t	total condition
w	due to wake blockage
wet	based on wetted surface area
wo	wind on
woff	wind off

Chapter I

Introduction

Support interference is a serious problem in testing models in wind tunnels (refs. 1 and 2). Figure 1 shows three examples of model support problems. In each case, the sting support required a model geometry different from the aircraft geometry. The presence of the sting also distorted the base flow in each case. This combination of geometry modification and distorted base flow produced the errors shown. Using a Magnetic Suspension and Balance System (MSBS) is the only way to eliminate completely support interference. With the elimination of the support, not only will the flow distortion produced by the sting be eliminated, but many other advantages accrue such as:

a) elimination of model modifications to accomodate the sting

b) ease of model movement for dynamic testing

c) fast, efficient testing at any attitude and

d) improvement in productivity by elimination of stings and struts.

Other, more exotic advantages are predicted in reference 3.

A MSBS is a device capable of both suspending a model in space and measuring the forces and moments acting upon it. This is accomplished through the use of controlled magnetic fields interacting with a magnetized core placed in the model. In a wind tunnel setting, a MSBS uses electromagnets positioned external to the test section. The core is either a permanent magnet, magnetized soft iron, or a solenoid within the model. The position of the suspended model is inherently unstable, and a closed-loop feedback control system which incorporates a method of sensing the model position and attitude is therefore required to stabilize the model by actively controlling the applied magnetic fields (refs. 4 and 5). The MSBS can counteract a range of external forces and moments applied to the body while maintaining the model at any arbitrary position. The amount of electrical current flowing in each of the external electromagnets is used to determine the forces and moments acting on the suspended

model.

The French at ONERA first demonstrated a wind tunnel MSBS in the mid-1950's (ref. 6). Since that time, considerable research efforts have been devoted to MSBSs and many improvements have been made (ref. 7). Today, applying MSBSs to routine wind tunnel testing of aircraft models is practical; however, they are still not widely used. This is principally a result of the small size of all existing systems.

Recent technical advances have removed some of the barriers to building large MSBSs. One example is progress with large superconducting electromagnets which would be needed to support the weight of the model and also to counteract the large aerodynamic loads. Another is the use of a superconducting solenoid as a model core (ref. 8) which would produce a model with the highest possible magnetic moment. Using this type of core would reduce the overall system cost by minimizing the required size of the external electromagnets. In addition to these advances, feasibility and conceptual design studies (refs. 9, 10, and 11) have produced innovative MSBS designs. These new designs significantly reduce the cost of large systems, making them more affordable for large wind tunnels. Simultaneously, the cryogenic wind tunnel concept was developed by Langley researchers as a way of increasing the Reynolds number in small wind tunnels equipped with MSBSs without an attendant increase in model loads. The cryogenic tunnel concept is a success and it provides the same benefits for a large tunnel at even larger Reynolds numbers (refs. 12 and 13).

Since the late 1970s, in-house activity with MSBSs has steadily increased at NASA Langley. In 1979 the United States Air Force loaned the MSBS at the Arnold Engineering Development Center (AEDC) (ref. 14) to Langley. The system was initially used to gain operational experience with a working MSBS. Ownership of the 13″ system has since transferred to NASA from the Air Force.

Early in 1984 this 13″ MSBS was combined with a small low-speed, $M \leq 0.5$, wind tunnel. The primary goal was to gain some practical experience with this system with the emphasis placed on using and understanding the MSBS rather than on obtaining aerodynamic data. The 13″ MSBS was then modified in several respects. The original AEDC X-ray position sensors were replaced with an electro-

optical system using solid-state linear photodiode arrays, and the original analog control system was replaced with a digital controller using a PDP-11/23+ minicomputer (ref. 15). These and other improvements make the system easier to use.

However, several limitations still exist. One is a limited angle of attack capability ($\pm 5^{o}$). Another is difficulty in suspending irregular shaped three dimensional models. Both of these limitations arise because of the design and nature of the electro-optical position sensing system. Despite these limitations, the emphasis at the present time is on using the 13″ MSBS to obtain useful aerodynamic data. The existing position sensing system works well with most axisymmetric shapes. Therefore, a program is underway to obtain accurate drag data on various axisymmetric shapes at zero incidence.

This program takes advantage of two previously mentioned improvements offered by MSBSs. One is the complete elimination of support interference error due to flow distortion and the other is the elimination of model modifications to accomodate the sting. For many configurations the flow distortion error manifests itself in the base pressure coefficient. There can also be errors due to distortion of the wake flow.

For this thesis, low-speed wind tunnel drag force measurements were taken on a laminar flow body of revolution free of support interference in the Langley 13″ MSBS. The primary objective of these tests was to substantiate the drag force measuring capabilities of the 13″ MSBS. Generally, a multi-component strain-gage balance is accurate to $\pm 0.5\%$. The basic accuracy of a multi-component magnetic balance should equal or exceed that of a standard multi-component strain-gage balance; however, the obvious advantage of a MSBS is the total elimination of support interference. In this context, aerodynamic data from a MSBS is more accurate than data obtained from a conventionally supported model using a strain-gage balance. A secondary objective of these tests was to obtain accurate drag measurements on an axisymmetric body of interest. The measured drag coefficients for this body are of interest to researchers actively involved in designing minimum drag fuselage shapes where drag reduction is achieved by exploiting natural laminar flow on a body. This is accomplished primarily by altering the fuselage shape.

Chapter II

Description of 13″ MSBS

This system was constructed at the United States Air Force's Arnold Engineering Development Center (AEDC) in the early 1960's. Researchers at AEDC used the system primarily for wake studies with axisymmetric models at hypersonic Mach numbers (ref. 14). For this system, motion is controlled in five degrees of freedom with no provision for generation of controlled magnetic roll torque on the model. X-ray beams that penetrated the aluminum wind tunnel walls were used to sense the position of the model in the test section of the AEDC tunnel in order to avoid problems with window joints disturbing the flow in the model wake. The AEDC MSBS, despite its 20-year vintage, was relocated to Langley in 1979 to provide some needed in-house MSBS capability. Langley personnel renamed the system the 13″ MSBS to reflect the approximate size of the test section used with the system.

Figure 2(a) shows a sketch of the arrangement of the 13″ system. Figure 2(b) shows a photograph of the system. This system has four lift electromagnets, arranged in a "V" configuration above the wind tunnel test section, that provide the lift force, pitching moment, side force, and yawing moment. The 13″ MSBS has a lift force capability of about six pounds depending on the size and shape of the iron core in the model. The drag solenoid provides the drag force. The test section for the tunnel passes through the drag solenoid.

Figure 3 shows a block diagram of the 13″ MSBS hardware as it was during these tests. All of the electromagnets have conventional copper windings. The drag electromagnet is fed from a bipolar thyristor power supply while the other electromagnets were fed from a mix of unipolar thyratron supplies and rectified motor-driven variacs. The bipolar supply used with the drag electromagnet enables it both to push and pull on the model. Note that each of the four main electromagnets was composed of two sets of windings per pole, a set of bias windings and a set of control windings. The bias windings supplied a steady current necessary to suspend a model. This reduced the amount of

control current needed during actual operation.

The control system is completely digitized with a PDP 11-23+ minicomputer handling all of the control functions (ref. 15). Feedback control of the power amplifiers supplying the electromagnets must be used in all magnetic suspension systems to stabilize the position and attitude of the model. Typical feedback loop repetition rates for this system are on the order of 256 cycles per second. Electromagnet currents are monitored using conventional shunts and a purpose-built isolation amplifier system. 12-bit A/D converters receive the outputs from these amplifiers. These amplifiers are also used as the interface between the D/A converters and the electromagnet power supplies. The minicomputer houses both the A/D and D/A converters.

The optical position sensing system is based on solid-state linear photodiode arrays. The five arrays are each composed of 1024 separate, photodiode elements. These elements are spaced 0.001″ apart. Simple thresholding techniques are used, yielding an ultimate precision of around one spacing (0.001″). The angle of attack limitation of $\pm 5^{o}$, mentioned earlier, is primarily a function of the array size; larger arrays would allow testing at higher angles of attack. Figure 4 illustrates the hardware arrangement. Laser light sheets are directed across the test section to illuminate the arrays. The model position and attitude are inferred by locating the shadow of the model on the arrays. This technique is very geometry dependent. Abrupt changes in shadow positions are generally not tolerated by the control system; therefore, it is difficult to suspend many non-axisymmetric shapes, especially bodies with wings at various pitch and/or yaw angles. Reference 16 gives more details on this optical position sensing system.

Chapter III

Description of Wind Tunnel

A small, low-speed wind tunnel was adapted to use with the 13″ MSBS. This tunnel consists of sections of a flow apparatus originally constructed to study portions of the U.S. National Transonic Facility (NTF). As shown in figure 5, the tunnel is an open circuit design with air drawn into the tunnel from outside the building through a large bellmouth protected from birds and leaves by a screen enclosure. Constant diameter ducting extends the circuit to the first turn. The turn has 16 vanes constructed of rolled aluminum. Following the first turn, a quick diffuser and settling chamber with screens and honeycomb prepare the flow for entry into the contraction and test section. The contraction ratio is 8.43.

The clear lexan test section is a modified octagon shape with major and minor axes of 12.56 and 10.68 inches, respectively (See figure 6.). The three shaded sections in figure 4 represent the new tunnel sections constructed for use with this layout. The transition section was designed so the extended contraction and diffuser would have the same geometry. These identical sections were fitted between the test section (see figure 5) and other existing portions of the tunnel circuit. The transition design consists of straight line elements from a 17.2 inch diameter to the modified octagon shape of the test section. Following the main diffuser, a section of 2.5 inch thick honeycomb is used to protect the fan. A turn identical to the inlet turn directs the flow to the fan section and then to the exit outside the building. The fan has 14 compressor blades (each approximately 3.75 inches long) and 15 stators. A water-cooled, 200 hp, 6000 rpm, variable frequency electric motor drives the fan. Reference 17 gives full details on the tunnel layout and calibration.

The flow quality in the tunnel is as follows:

a) a maximum deviation of $\pm$ 0.25% in dynamic pressure across the test section

b) a freestream turbulence level of 0.1% or less depending on the dynamic pressure and

c) flow angularity in pitch of -0.52^{o} relative to the test section floor.

Chapter IV

Description of Model

Figure 7 shows a photograph of the model which has a long favorable pressure gradient forebody. The body profile was generated from an eight-parameter class of rounded-nose, tailboom bodies described in reference 18. This class of bodies was developed to verify a method of shaping axisymmetric bodies to produce minimum drag in incompressible, nonseparating flow at zero incidence. An optimization scheme constrained to exclude turbulent separation is used to minimize C_D. This scheme achieves drag reduction by body shape modification. Drag reduction was accomplished computationally by extending the laminar flow region on the body.

A sting mounted version of this shape was previously tested in a towing tank at the United States Naval Academy by Hansen & Hoyt (H & H) (refs. 19 and 20). The model tested by the Navy was slightly modified from the design shape in the tail region in order to accomodate the sting. Figure 8 shows a sketch of the test setup used by the Navy. One of the goals of these tests was to quantify the hydrodynamic performance of this body. Drag measurements on this shape are of interest to researchers involved in computational design procedures for fuselage body shaping for minimum drag (refs. 21 and 22). The ultimate objective of this research is to reduce the drag of aircraft by increasing the extent of natural laminar flow on fuselages.

The model used for the present study is 12 inches long with a maximum diameter of 2.68 inches. The model, which weighs about 2 pounds, was made in two longitudinal halves using a fiberglas skin that is foam filled around an embedded soft iron core. This ultra-low carbon iron core is magnetized by the applied magnetic fields. The core is 1 inch in diameter by 6 inches long and it is centered in the model. Because of the lack of roll control for the 13″ MSBS, the model was weighted to provide a constant roll position. This was done during fabrication by placing a 20 gram brass weight against the inside surface of the model's skin.

Table I lists the eight nondimensional parameters used to generate this body of revolution according to the method described in reference 18. Table II lists the coordinates of the model.

Chapter V

Description of Surface Flow Visualization Techniques

5.1 *Liquid crystals.* - A liquid crystal surface flow visualization technique was used to determine transition and/or separation locations. This technique is discussed in detail in references 23, 24, and 25. Liquid crystals are a substance with properties of both liquid-phase and solid-phase materials. They can display the optical properties of solid crystals by scattering light very selectively. These optical characteristics can be displayed by altering the molecular structure of liquid crystals. The molecular structure is primarily influenced by temperature and shear stress which cause the liquid crystals to selectively reflect various colors.

A wide temperature bandwidth formulation of liquid crystals was chosen for this study so that shear stress would dominate in determining the liquid crystal color response. This sheer stress response can be used to visualize various boundary layer flows including transition and separation. Liquid crystals indicate transition by changing colors in response to the large shear stress change through the transitional region (See figure 9.). Separation is indicated by a change from "color" to "no color" at a point on a body because C_f is zero in a separated region.

For the present study, the models were painted flat black. As noted in reference 25, this provides the best background surface for visualizing liquid crystals. The liquid crystals were thinned with a solvent and applied by spraying a thin coat on the model surface. A good application results in a coating thickness of approximately 0.0005 to 0.001 inches. One coat could be used for several tunnel runs at different Reynolds numbers.

5.2 *Pigmented oil.* - A pigmented oil surface flow visualization technique was also used to determine separation locations. This is a type of oil flow which uses a mixture of titanium dioxide (TiO_2) suspended in refined mineral oil. A small amount of oleic acid is added as an anti-coagulant. After

brushing the mixture on the black model surface, the model was placed in the tunnel and suspended. The tunnel was then brought to test conditions, and, after the oil dried, the TiO_2 was left deposited on the surface.

Chapter VI

Test Procedure

A specific routine is followed each time a model is suspended in the 13″ MSBS. First, the alignment of each position sensor channel is checked. The hardware components for the position sensor system are very susceptable to slight movements that may occur between runs; therefore, the alignment is checked frequently. The model is then placed on the support arms in the test section. These support arms are two retractable rods each with a very thin piece of aluminum plate attached to the end that form a v-shaped cradle to hold the model in place. The model is positioned on the support arms so that its shadow is picked up on each of the five arrays. The door is then secured to the test section.

Following a power-on sequence, the model is slowly lifted off the support arms with the aid of software position error integrators. This lift off sequence is performed through keyboard control from a terminal connected to the PDP 11/23+ minicomputer in the control room (See figure 10.). The error integrators then aid in moving the model to the desired position. The support arms are retracted until the aluminum plates are flush against the inside of the test section. All model movements are initiated from the keyboard.

For this study, the model was tested at zero incidence. The pitch attitude, vertical position, and horizontal position of the model were verified using an optical cathetometer. This is a remote fixed device used to measure relative vertical and horizontal displacements (See figure 11.). The pitch attitude, vertical position, and horizontal position were accurate to approxmately $\pm$ 0.02^{o}, 0.002″, and 0.002″, respectively. The model pitch attitude was not corrected for the flow angularity mentioned in Chapter III. The yaw attitude and lateral model position relative to the test section sidewall were verified by using a laser light sheet shining longitudinally across the top of the model. This light sheet was positioned prior to suspending the model. The position of the model relative to the light sheet was checked by using a miniature CCD video camera and monitor which provided a view from above the

model showing the intersection of the laser light sheet with the top of the model. It is estimated that the yaw attitude and lateral position were accurate to $\pm$ 0.6^{o} and 0.1$''$, respectively.

To land the model, the support arms are reinserted and the model is slowly lowered. Before the model touches the plates, the position error integrators are turned off, and the model is then lowered further until contact is made with the plates. The electromagnet power supplies are subsequently turned off.

For this study, the initial phase of testing for each model consisted of a drag force calibration. The calibration involved suspending the model with no wind and loading it in the axial direction. For this type of calibration, the lift electromagnets suspend the model by supporting its weight. The drag electromagnet works to counteract the applied load. The loading was performed using the traditional string, pulley, and weight pan combination as shown in figure 12. Each model was fabricated with a threaded insert at the rear that provided an attachment point for the line used to pull on the model.

A data acquisition unit (DAU) and a microcomputer were used to read and record the data (See figure 10). Figure 3 shows the DAU tied directly into the shunts which provide a means of measuring the current in the electromagnets. For a given weight or load, shunt voltages and magnet currents were recorded using the microcomputer. Voltages were converted on-line to obtain equivalent currents using a shunt voltage versus current calibration performed earlier. The computer software continuously updates and displays the last five values and the average values of both shunt voltages and magnet currents on the screen. These values were also recorded as the model was unloaded to check for hysteresis. The drag electromagnet current was plotted against the load to determine a calibration curve for the model.

To record wind-on drag measurements, the model was suspended at the same location where the calibration was performed. For a given Mach number, shunt voltages and magnet currents as well as the tunnel conditions (p_s, p_t, and T_t) were recorded using the DAU and the microcomputer. A typical data point contains the last five readings of the voltages, currents, and tunnel parameters. An additional check on the consistency of the drag electromagnet current values was also performed by the

computer operator for each data point. The DAU reads reference static pressure and tunnel total pressure from signal conditioners used with two highly accurate Datametrics Barocel pressure transducers. The total temperature was also read by the DAU from a thermocouple in the settling chamber.

Chapter VII

Data Reduction and Corrections

7.1 *Data Reduction.* - All of the data were recorded on 5 1/4 inch floppy disks used with the microcomputer. Most of the data reduction was done off-line with the on-line data reduction consisting only of the shunt voltage to electromagnet current conversion mentioned earlier. After a data run, the wind-on axial currents were converted to equivalent drag forces using the second order polynomial curve fit from the drag calibration. The "averaged" drag electromagnet current data were used. The raw voltage data were inspected for inconsistent values. If an inconsistent value was found for a particular data point, this value was removed and the remaining ones were re-averaged to obtain a new "averaged" value for that data point. Occassionally, an inconsistent value was present as a result of an inadvertent model movement caused by electrical noise on the position sensing system.

7.11 *Tunnel flow parameter equations.* - The measured tunnel pressures (p_t and p_s) and temperature (T_t) were used to calculate the following flow parameters.

Mach number

The free-stream Mach number is calculated using the static-to-total pressure expression for isentropic flow of an ideal gas which is defined as

$$\frac{p_t}{p_s} = \left[1 + \frac{\gamma - 1}{2} M^2\right]^{\frac{\gamma}{\gamma - 1}} \tag{1}$$

with M then defined as

$$M = \sqrt{\frac{2}{\gamma - 1}\left[\left(\frac{p_t}{p_s}\right)^{\frac{\gamma - 1}{\gamma}} - 1\right]} \tag{2}$$

Static temperature

The static temperature, T_s, is calculated using the static-to-total temperature expression for isentropic flow of an ideal gas which is defined as

$$T_s = \frac{T_t}{1 + \frac{\gamma - 1}{2} M^2} \tag{3}$$

Velocity

Velocity is defined as

$$V = Ma \tag{4}$$

The ideal gas value for the speed of sound is defined as

$$a = \sqrt{\gamma \Re T_s} \tag{5}$$

so that

$$V = M\sqrt{\gamma \Re T_s} \tag{6}$$

Dynamic pressure

Dynamic pressure is defined as

$$q = \tfrac{1}{2}\rho V^2 \tag{7}$$

By using the ideal gas equation of state, $\rho = \frac{p_s}{\Re T_s}$, and equation (6), the dynamic pressure can be expressed as

$$q = \tfrac{1}{2}\gamma p_s M^2 \tag{8}$$

Viscosity

The viscosity is calculated from

$$\mu = 2.270\left[\frac{T_s^{1.5}}{T_s + 198.6}\right] \times 10^{-8} \tag{9}$$

This equation is from reference 26.

Reynolds number

Reynolds number is defined as

$$R = \frac{\rho V L}{\mu} \tag{10}$$

Expressing R in terms of q gives

$$R = \frac{2qL}{V\mu} \tag{11}$$

Substituting for V and q from equations (6) and (8) gives

$$R = \frac{\gamma p_s ML}{\mu\sqrt{\gamma \mathfrak{R} T_s}} \tag{12}$$

R is calculated in terms of known parameters (p_t, p_s, and T_t) using equations (2), (3), (9), and (12).

7.12 *Drag force and coefficient equations*

When using a soft iron core, a drag force calibration curve fit from the 13″ MSBS takes the following form:

$$D = AI^2 + BI + C \tag{13}$$

The coefficients, A, B, and C, change for different models or cores and/or different locations of the model or core in the electromagnetic fields.

During a typical drag force calibration for this study, the first data point was taken using a 5 gram weight attached to the calibration line. To get the drag electromagnetic current value for a zero axial load, equation (13) was solved using the quadratic formula. This formula is defined as

$$I = \frac{-B \pm \sqrt{B^2 - 4AC}}{2A} \tag{14}$$

The positive root, I_o, is the drag electromagnet current value for a zero axial load.

When converting the wind-on drag currents to equivalent forces, a delta current is initially obtained for each data point using

$$\Delta I = I_{wo} - I_{woff,0} \tag{15}$$

The corrected current for each data point is then defined as

$$I_c = I_o + \Delta I \tag{16}$$

The drag force was computed by using I_c in equation (13). This corrected current was used to compensate for possible wind-off current zero shifts.

Drag coefficient is defined as

$$C_D = \frac{D}{qS} \tag{17}$$

Substituting for q from equation (8)

$$C_D = \frac{D}{\frac{1}{2}\gamma p_s M^2 S} \tag{18}$$

7.2 *Buoyancy corrections.* - Three-dimensional buoyancy corrections were applied to the drag force data using the following equation from reference 27

$$\Delta D_B = -\frac{\pi}{4}\lambda t^3 \frac{dp}{dl} \tag{19}$$

The λ term for a body of revolution is defined as

$$\lambda = 4\int \frac{v}{V}\frac{[z(s)]^2}{t^3}ds \tag{20}$$

This constant term was calculated using the potential solution results from the computer code SANDRAG which will be discussed later. The value of λ for the laminar flow body is 2.6994. For the $\frac{dp}{dl}$ term, tunnel empty pressure measurements were taken along the centerline of one of the vertical test section walls. This pressure gradient varied with tunnel speed; therefore, a curve fit of $\frac{dp}{dl}$ as a function of M was used when applying these corrections to the data.

7.3 *Blockage Corrections.* - Both solid and wake blockage corrections (ref. 28) were applied to the results of this study. The blockage factor is defined as

$$\epsilon_b = \epsilon_{s'} + \epsilon_w \tag{21}$$

The solid blockage term, $\epsilon_{s'}$, for three dimensional models in rectangular test sections is defined as

$$\epsilon_{s'} = \tau\left[\frac{A_m}{bh}\right]^{3/2}\frac{1}{\beta^3}\lambda \tag{22}$$

The τ term is defined as

$$\tau = \frac{1}{2\pi^{3/2}}\sum_{-\infty}^{\infty}\sum_{-\infty}^{\infty}\left[\frac{bh}{m^2b^2 + n^2h^2}\right]^{3/2} \quad \text{except for (m,n) = (0,0)} \tag{23}$$

This equation gives a value of τ for a rectangular test section of width, b and height, h. For this investigation, the test section shape was a modified octagon which can be considered a rectangle with

fillets. In reference 29, Batchelor showed that the value of τ for a $7'$ by $9'$ rectangular test section with fillets (similar to the shape used with this investigation) is very close to the value of τ for the basic rectangle. For the $7'$ by $9'$ tunnel, the basic rectangle value is 0.71, and the approximate value with fillets is 0.75. Batchelor approximated the interference due to the fillets by introducing sources and sinks along with the doublet used to represent the model to satisfy a boundary condition of no flow across the fillets. For this study, the value of τ is assumed to be the value for the basic rectangle. The basic rectangle is $12.56''$ by $10.68''$ and τ is 0.818.

The wake blockage term, ϵ_W, for three dimensional models in rectangular test sections is defined as

$$\epsilon_W = \frac{1}{4}\left[\frac{S}{bh}\right]\left[\frac{1 + 0.4M^2}{\beta^2}\right]C_{D0} \tag{24}$$

For this study, equations (22) and (24) are used with bh replaced by the cross-sectional area of the test section. This modification is suggested in reference 28 as an approximation for octagonal test sections.

Chapter VIII

Discussion of Experimental Results

8.1 *Drag force calibration.* - As mentioned in Chapter VI, the calibration was performed using the setup shown in figure 12. Electromagnet current measurements were recorded as the model was loaded from 5 to 242.5 grams. Current measurements were also recorded as the model was unloaded to check for hysteresis. The results from this calibration, shown in figure 13, indicate that there is practically no hysteresis in this data. The data were fitted with a second order polynomial. Figure 14 shows a residual plot for this drag force calibration. A residual is the difference between the output from the magnetic balance and the calculated output from the polynomial equation. The standard deviation for this calibration is 0.27 grams or 0.11% of the full-scale calibration load of 242.5 grams.

This small uncertainty may be attributable to a small amount of magnetic hysteresis present in the model core. Another possible cause is intermittent vibrations of the model due to slight vibrations of the optical position sensing system. Prior to these tests, a study was performed in the 13″ MSBS comparing the effects of core material on calibration results. Two different core materials were used, mild steel and the same ultra-low carbon iron used with the present study. The ultra-low carbon iron exhibited much less magnetic hysteresis than the mild steel.

Following the wind-on data runs for the laminar flow body, an additional drag force calibration was performed with the same loading range repeated. Figure 15 shows the results of this calibration as compared to the first calibration from figure 13. This second calibration was also fitted with a second order polynomial. The two curve fits from the calibrations were compared and the differences or residuals are plotted in figure 16. The standard deviation between the two curve fits is 1.2 grams or 0.49% of the full-scale calibration load. These differences can be attributed to the following two factors:

1) Inaccurracies in locating the model at the same location for both calibrations which is

primarily due to the yaw attitude and lateral position. Recall that the yaw attitude and lateral position were accurate to $\pm$ 0.6° and 0.1″, respectively.

2) Inaccuracies in the pitch angle of the calibration line used to pull on the model. This angle, which was also measured by the cathetometer, was approximately $\pm$ 0.75° from 0° in pitch.

8.2 *Drag force characteristics and repeatability of data.* - Figures 17, 18, and 19 are photographs of this model in suspension. Figure 17 is a view of the 13″ MSBS from the control room. Figure 18 is a closeup of the laminar flow body in suspension, and figure 19 is a view from the contraction section of the tunnel looking at the nose of the body while in suspension. Wind-on drag force measurements were taken for this body over the Mach number range from approximately 0.05 to 0.2. The results, presented in figure 20, indicate that $C_{D,wet}$ decreases as R_L increases. Table III lists these corrected drag coefficients. Theoretical drag coefficients for laminar and turbulent flat plates are shown in this and many subsequent figures to provide a familiar reference. The following equations from reference 30 were used to generate these flat plate results:

$$C_D = \frac{1.328}{\sqrt{R_L}} \qquad \text{(laminar)} \qquad (25)$$

$$C_D = \frac{0.074}{R_L^{1/5}} \qquad \text{(turbulent for } R_L < 10^7\text{)} \qquad (26)$$

$$C_D = \frac{0.455}{(\log R_L)^{2.58}} \qquad \text{(turbulent for } R_L < 10^9\text{)} \qquad (27)$$

Figure 21 shows a repeat run comparison; there is excellent repeatability of the data. The standard deviation of these two sets of data in terms of drag force is approximately 1.4 grams or 0.58% of the maximum calibration load of 242.5 grams. The deviation from the mean is larger at the higher Mach numbers due to vibrations exhibited by the model at these speeds. If the last four data points are not used, the standard deviation reduces to 0.6 grams or 0.25% of the maximum load. Also note

that the standard deviation of these two sets of data in terms of $C_{D,wet}$ is 0.00015.

In reference 31, Hoerner shows the general drag coefficient versus Reynolds number trends for streamlined bodies of revolution (see figure 22). In the Reynolds number region from 10^4 to 10^5, Hoerner has estimated the drag coefficient assuming there is laminar boundary layer separation without reattachment as in the case of flow over a spheroid. From $R = 10^5$ to 10^6, C_D decreases drastically due to the onset of transition and turbulent flow. The turbulent flow energizes the boundary layer and carries the flow further around the body resulting in a smaller wake and thus a lower drag coefficient than was present with laminar separation. From $R = 10^5$ to around 10^7, transition is moving forward. At around 10^7, there is fully turbulent flow over the bodies. Note that the data from the present study follow some of the same trends shown in figure 22 in the Reynolds number range from 10^4 to 10^6.

Figure 23 is an oil flow photograph from the present study showing a laminar separation bubble at $R_L = 1.2 \times 10^6$. Figure 24 is a liquid crystal flow visualization photograph† also showing this laminar separation region at the same R_L. A laminar separation line and turbulent reattachment line are shown in both figures. At lower values of R_L it was observed that the separation line was at a more forward station on the body. It is estimated that this separation line originated between $x/L = 0.50$ and $x/L = 0.55$, and it was observed that this separation line moved rearward as R_L increased. It was also observed that the reattachment line originated near the tail of the body at a lower R_L. This reattachment line moved forward as R_L increased. Thus, this separation bubble decreased in size as R_L increased.

Based on these flow visualization observations and the drag coefficient results, the following deductions are made:

a) As R_L increased up to approximately 7×10^5, the laminar separation line moved very slowly rearward with either no reattachment or reattachment close to the tail. The increasing length of the attached laminar boundary layer would decrease the skin-

† Note that the photographs in figures 24 and 28 were artificially enhanced to highlight the "colored" regions. This was necessary due to poor contrast on the original negatives.

friction drag. This, combined with the reduction in wake size due to the rearward moving separation line, may account for the gradual decrease in $C_{D,\ wet}$ in this region.

b) For $R_L > 7 \times 10^5$, the reattachment line moved forward from the tail as the separation line moves rearward. $C_{D,\ wet}$ subsequently decreased significantly as R_L increased through this region. This drastic decrease may be attributable to the decreasing size of the separation bubble and/or the decreasing size of the wake.

The development and progression of the laminar separation bubble in this study is consistent with separation bubbles on airfoils as noted in reference 32. In reference 32, Roberts lists four possible flow regimes for airfoils with separation bubbles. These are:

a) complete laminar separation at low values of R_L

b) long bubble region as R_L increases

c) short bubble region as R_L increases further

d) transition prior to separation as R_L increases further

As noted, the first three regimes appeared to be present during this study.

References 32 and 33 point out that the velocity and pressure distributions on a body are increasingly affected as the bubble size increases. In addition, reference 34 points out that the turbulent boundary layer behind a separation bubble is thicker than the turbulent boundary layer for the case where there is smooth attached flow without a bubble. This was also pointed out by Holmes (ref. 35). These factors help to substantiate the deduction above which relates the drastic decrease in $C_{D,\ wet}$ to decreasing bubble size.

8.3 *Comparison with other data.* - As mentioned earlier, this shape was also tested by H & H (refs. 19 and 20). For the present study, the desire was to test the model in the 13″ MSBS up to M = 0.5 to overlap the lower Reynolds number data of H & H. However, static aerodynamic stability problems exhibited by the model would not allow testing above M = 0.2. As a result, only one data point from

this study overlaps the H & H data. However, an attempt is made to compare the data by looking at the relative drag coefficient levels as shown in figure 25. Note the large discrepancy in $C_{D,wet}$ at $R = 1 \times 10^6$. The author attributes this discrepancy to the fact that the H & H data was not corrected for cavity pressure. In reference 20, Hoyt states that the corrections were not performed; however, he gives the necessary information to correct the data for cavity pressure. Hoyt suggests using the following equation:

$$D_{corr} = D_{meas} - p_b(\text{Area inside tail piece} = 45 \text{ in}^2) \tag{28}$$

D_{meas} and D_{corr} are the measured and corrected drag forces, respectively. This author corrected the H & H data using equation (28) with the results shown in figure 26. Note that the corrected data are more in line with the results from the present study. The author attributes the difference that still exists at $R = 1 \times 10^6$ to one or more of the following:

a) The sting at the rear of the H & H body may act as an extension of the body. This would result in a higher fineness ratio shape which would reduce the overall drag coefficient. (See figure 22.).

b) The sting would divide and alter the wake region at the tail of the model, possibly reducing the overall drag.

c) The rear portion of the H & H model was slightly modified to accommodate the sting. The H & H model does not have the slight flair at the tail as in the 13″ MSBS model. This slight modification may have altered the wake pattern.

Note that there are unexplained discrepancies when comparing the H & H data given in references 19 and 20. These data should be the same. During a private communication with Hoyt (ref. 36), he stated that the data in reference 20 are correct. Therefore, the data from reference 20 are used in this paper.

8.4 *Comparison of free and fixed transition.* - Several fixed transition runs were performed in an effort to assess the effect of fixing transition on the laminar separation bubble (ref. 37). Transition was fixed

at two different locations using different trip sizes. Three-dimensional abrasive grain transition grit was used with transition fixed at the 17% and 50% locations. The trip sizes used were grit numbers 100, 80, 60, and 40 which correspond to nominal trip sizes of 0.006, 0.008, 0.012, and 0.020 inches, respectively.

Initially, the following equation from reference 38 was used to properly size the grit

$$k = \frac{(2x')\eta_k}{\sqrt{R_{x'}}} \tag{29}$$

Figure 4 from reference 38 was used to determine η_k with a value of 600 assumed for R_k. Since $R_{x'}$ changes with M, a different value for k could be calculated for each M. For this study, k was calculated for both M = 0.1 and M = 0.2. Using this technique, the values of k for M = 0.1 are 0.012 and 0.015 at the 17% and 50% stations, respectively, and the values of k for M = 0.2 are 0.007 and 0.009. Based on these results, grit numbers of 60 and 80 were chosen for the 17% station. In addition, grit numbers 40 and 100 were used at this station for comparison. Grit numbers 40 and 80 were chosen for the 50% station.

Figure 27 shows a free and fixed transition comparison. The fixed transition data are for the number 60 grit at the 17% station. At the lowest Reynolds number, the boundary layer is thick and the grit has no effect. However, as R_L increases to 5 x 10^5, $C_{D,\ wet}$ decreases drastically. This is a transitional region where the boundary layer is not yet fully turbulent beyond the grit. However, there is enough energy imparted from the grit to keep the boundary layer attached beyond the laminar separation line. Rearward movement of the separation line results in a lower $C_{D,\ wet}$. For $R_L > 10^5$, the boundary layer is fully turbulent beyond the grit and the turbulent separation point moves much more slowly rearward with increasing R_L. This results in a much slower decrease in $C_{D,\ wet}$ with increasing R_L. Figure 28 shows liquid crystal flow visualization results for this fixed transition case. Note the turbulent separation stations. The location is further back on the model for the higher Reynolds number case. As a comparison, the laminar separation station from figure 24 is x/L = 0.63.

Figure 29 shows a fixed transition comparison at the 17% station using all four grit sizes. As the grit size decreases (grit number increases), the significant reduction in $C_{D,\ wet}$ occurs at successively higher values of R_L because the smaller grit is less effective in fully tripping the thicker boundary layer at the lower Reynolds numbers. As R_L increases, the boundary layer thins and the smaller grit effectively trips the boundary layer to turbulent flow.

Figure 30 shows a free and fixed transition comparison at the 50% station using two grit sizes. Transition was fixed at this location in order to retain laminar flow over a large portion of the body while avoiding laminar separation by making the boundary layer turbulent just ahead of the separation bubble. It was also envisioned that tripping the boundary layer in this region would allow the turbulent boundary layer to remain attached further on the body, thus resulting in a lower $C_{D,\ wet}$. The data in figure 30 show the same trends as shown in figure 29. The smaller grit (number 80) did not trip the boundary layer to fully turbulent flow until $R_L = 1 \times 10^6$. The larger grit (number 40) appears to have effectively tripped the boundary layer through the entire Reynolds number range. In fact, at R_L above 8×10^5 the boundary layer has thinned to the point where the number 40 grit is too large. This results in grit drag for Reynolds numbers greater than 8×10^5 where $C_{D,\ wet}$ is larger for the number 40 grit data as compared to the number 80 grit data. This grit drag is defined as the drag resulting from the thicker boundary layer, which leads to a larger momentum deficit, imposed by the number 40 grit.

8.5 *Comparison with and without fins.* - A set of fins were installed in the tail of the model (see figure 31) to assess their effectiveness in overcoming the static aerodynamic instabilities exhibited by the model at the higher Mach numbers. The fins did allow testing at higher speeds (up to M = 0.3), thus verifying that the instabilities were aerodynamic. The increase in drag coefficient when compared to the model without fins is shown in figure 32. The change in $C_{D,\ wet}$ is relatively constant except at the higher Reynolds numbers where the increase is greater.

Figure 33 shows a free and fixed transition comparison for the finned model. Transition was fixed at the 50% station with number 80 grit. A comparison of this data with fixed transition (same grit size) data from figure 30 shows large differences, especially at the higher Reynolds numbers. One would expect these differences to be the same magnitude as those in figure 32. These larger differences may be due to inconsistent applications of the grit from one run to the next.

8.6 *Base pressure measurements.* - Personnel in the Instrument Research Division at Langley developed a one-channel infrared telemetry system for use with the 13″ MSBS (ref. 39). This system was built to fit inside the model used with this study. An additional model was made in two longitudinal halves that can be easily disassembled to provide access to the telemetry system. Figure 34 shows a photograph of the model halves with the telemetry system installed. This system includes a pressure transducer, a signal conditioning circuit, an infrared light emitting diode, and a battery package. A receiver located outside the test section was used to pick up the frequency signals from the diode. The system is activated in the presence of a magnetic field; therefore, a signal was continuously transmitted.

The transducer is a 2 psi piezo-resistive differential type. The transducer vent tube was filled with argon gas at atmospheric pressure and sealed. The pressure reading is the difference between the base pressure and the pressure in the vent tube. Calibrations of the transducer and electronics were performed over a range of temperatures to account for the change in vent tube pressure with temperature. The calibrations of frequency versus pressure were linear and repeatable with the overall system precision stated to be better than 0.5% (ref. 39).

The base pressure measurement results are shown in figure 35. The base pressure coefficient is defined as

$$C_{p,base} = \frac{p_{base} - p_s}{q} \tag{30}$$

where p_s and q are the free-stream values of static and dynamic pressure. These $C_{p,\,base}$ values are

corrected for blockage as described in reference 28.

These base pressure results should be viewed cautiously. One reason for this is the lack of temperature data from inside the model during a run. It was assumed that the transducer and associated electronics were at the total temperature of the stream. This assumption gets poorer with time due to heating from the electronics inside the model. Another inaccuracy may result because the numerator in equation (30) is determined by subtracting a large number from another large number. In this case it would be better to have a more accurate differential transducer with a smaller pressure range. This particular shape is especially sensitive because the base pressure is very close in value to the free-stream static pressure.

Chapter IX

Description of Drag Prediction Codes

9.1 *SANDRAG code.* - A simple and efficient drag prediction code, SANDRAG, was used to obtain a theoretical estimate of $C_{D,\ wet}$ for this body (refs. 40 and 41). SANDRAG calculates the flow field and drag of bodies of revolution at zero angle of attack in incompressible flow by using a combination of a potential flow method and boundary layer techniques. This code has been used successfully to predict drag for some simple axisymmetric projectile shapes. The goal here was to verify the usefulness of this code in predicting drag for the more complicated axisymmetric shape used in the present study. An axial distribution of source and sink elements is used to form the body for the potential solution with the equations applying to both open and closed bodies. The body used for this study is considered an open body because the surface does not return to the axis at the tail. The laminar and turbulent boundary layer solutions use momentum integral techniques which account for the effects of surface roughness. Transition is modeled by taking into account the effects of pressure gradient and surface roughness. Separation is also modeled by predicting separation locations and estimating the drag based on the pressure in the separated region (separation drag). In the laminar boundary layer, separation is based only on the pressure gradient while in the turbulent boundary layer, separation is based on the value of the shape factor. Finally, the base pressure coefficient is estimated by using data correlations from various afterbody shapes.

9.2 *Nakayama and Patel code.* - A simple code was developed by Nakayama and Patel to calculate the viscous resistance or skin-friction drag of a streamlined body of revolution at zero angle of attack in incompressible flow (ref. 42). This code calculates the flow field and drag of bodies of revolution at zero angle of attack in incompressible flow by using a combination of a potential flow method and momentum integral boundary layer techniques. The Nakayama and Patel code has been used to

calculate fairly accurate drag coefficients for simple airship shapes in cases where the transition point is known or is predicted accurately (ref. 42). Once again, the goal here was to verify the usefulness of this code in predicting drag for the more complicated axisymmetric shape used in the present study.

Several empirical correlations are used to predict transition. In addition, the experimental transition location can be used. This code was primarily developed to evaluate the flow in the tail region. The turbulent boundary layer calculations are made using Patel's integral method (ref. 43) which accounts for thick turbulent boundary layers. Separation is not modeled by this code; in addition, this code does not provide estimates of base pressure drag.

Chapter X

Comparison of Experimental and Computational Results

10.1 *SANDRAG code.* - The potential flow pressure distribution for this body from SANDRAG is shown in figure 36. A comparison of the results from SANDRAG with the free transition data, shown in figure 37, generally indicates a large discrepancy between the theory and experiment. Further insight into the computational results is given in figure 38 which shows a breakdown of the various drag coefficient components and their contributions to the overall drag coefficient. For a given shape, SANDRAG breaks up the overall drag into four components: skin-friction drag, base pressure drag, pressure drag, and separation drag. The base pressure drag term is simply the base pressure coefficient multiplied by the ratio of the base area to the reference area. The pressure drag term is the drag based on the pressure distribution around the portion of the body that is not separated. Note that there is not a separation drag component for the laminar flow body in figure 38. At the lower Reynolds numbers ($R_L < 7 \times 10^5$), part of the discrepancy in figure 37 may be attributable to the lack of a separation drag in the computation. This is the drag based on the pressure in the separated region. Recall from previous discussions that the boundary layer may have separated completely in this Reynolds number region. Also note that the experimental and computational results approach each other as R_L increases as shown in figure 37. This may be attributable to the decreasing bubble size with increasing R_L. From previous discussions, it appeared that $C_{D,\ wet}$ decreased as the bubble size decreased because of a decreasing separation drag component.

The code did predict a separation bubble on the body in the turbulent boundary layer region following transition. However, it does not calculate a pressure drag contribution from this bubble. (Separation drag is apparently calculated only when the flow does not reattach.) It appeared from the flow visualizations that the separation point was in the laminar region, in which case transition actually occurs on the bubble (ref. 33). Incorrect prediction of transition and separation locations leads

to incorrect modeling of the shape factor and momentum thickness. Correct modeling of these factors is necessary to predict drag accurately.

The code also predicted that the bubble would decrease in size as R_L increases. This trend was also observed with the oil flow visualization. Figure 39 shows the predictions of turbulent separation and reattachment points for this bubble. Note the differences between the locations of the experimental and computational bubbles by comparing the oil flow results from figure 20 with the computational results from figure 39. The oil flow separation line is at x/L = 0.67 and the reattachment line is at x/L = 0.73. The computational separation point is x/L = 0.835 and the reattachment point is x/L = 0.878.

Part of the discrepancy in figure 37 may also be attributable to the calculation of base pressure coefficent. Recall that SANDRAG uses data correlations from various afterbody shapes to determine $C_{p,base}$. This code assumes a constant $C_{p,base}$ with changing Reynolds number. For this model, the code estimates that $C_{p,base} = -0.1964$. Comparisons with the base pressure measurements from figure 35 show a great discrepancy. The measured base pressure coefficients (corrected for blockage) are positive, whereas the estimate from the code is negative. As mentioned before, these measurements should be viewed with caution. However, the differences between the estimated base pressure and the measurements are great enough to question both results. Further experimental work is needed to verify $C_{p,\ base}$ for this model.

10.2 *Nakayama and Patel code.* - As noted in Chapter IX, this code calculates the skin-friction portion of the drag. It does not account for pressure drag, such as separation and base drag. Because of this, the predicted $C_{D,\ wet}$ values are low, as shown in figure 40. These predicted $C_{D,\ wet}$ values are very close to the skin-friction drag coefficient values from SANDRAG shown in figure 38.

For this study, correlations by Granville (ref. 44) and van Driest and Blumer (ref. 45) for transition prediction were used to compare with the free transition data. Using Granville's criterion, this code predicted laminar separation prior to transition with a laminar separation location of

$x/L = 0.67$ predicted for the entire Reynolds number range. The code assumes immediate reattachment of the turbulent boundary layer. Using van Driest and Blumer's criterion, the code predicted transition at $x/L = 0.66$ for the entire Reynolds number range. The code did not predict separation using this criterion. As shown in figure 40, both criteria give essentially the same drag coefficient results.

A comparison is also made with some of the fixed transition data by incorporating the experimental transition location into the code. This comparison is shown in figure 41 where the data are from figure 30 (number 40 grit at $x/L = 0.50$) and the computational results are based on a transition location of $x/L = 0.50$. The predicted $C_{D,\ wet}$ values are close to the experimental data. The differences are greater at the higher Reynolds numbers due to increasing grit drag for the experimental data. It is interesting to note that the computational results are fairly accurate in this case even though the code calculates skin-friction drag only. The flow is not fully attached in this case, as can be seen in figure 42, which is a liquid crystal flow visualization photograph showing turbulent separation at $x/L = 0.80$. In the absence of additional data to clarify these results, the author speculates that:

a) The drag for this fixed transition case is so skin-friction dominant that the base and separation drag components are very small in comparison and/or

b) The base pressure coefficients are positive as measured. This would correspond to a negative drag or thrust at the base. If this is true, then this base drag component may be offsetting the drag due to turbulent separation.

Chapter XI

Conclusions

The primary objective of this research was met by substantiating the drag force measuring capabilities of the 13″ MSBS. The drag force calibrations are very repeatable with practically no hysteresis. The standard deviation for the initial calibration is very small at 0.11% of the full-scale load. Wind-on drag force measurements showed excellent repeatability with the standard deviation between two sets of data at only 0.58% of the full-scale load.

The secondary objective of this research was also met by obtaining support interference free drag measurements on an axisymmetric body of interest. The free transition values of drag coefficient generally decreased with increasing Reynolds number. The drastic drop in $C_{D,\ wet}$ at the higher R_L values appears to be directly related to the decreasing size of the laminar separation bubble through this Reynolds number region. Comparisons of this data with data on general streamlined bodies show similar trends. Comparisons with other data (corrected for cavity pressure) on the same shape (Hansen & Hoyt) show a consistent level and trend with Reynolds number.

Tests with transition fixed generally showed a reduction in drag coefficient due to elimination of the laminar separation bubble. Fixing transition at the 50% station with number 80 grit gave the lowest $C_{D,\ wet}$ value for these investigations. This value occurred at $R_L = 1.3 \times 10^6$. A further reduction in $C_{D,\ wet}$ may be obtained by fixing transition just ahead of the laminar separation line. This lower drag coefficient would result from a longer run of laminar flow on the body prior to transition.

The model exhibited aerodynamic instabilities that did not allow testing above M = 0.2. A set of fins installed in the model's tail allowed testing up to M = 0.3, thus verifying that the instabilities were aerodynamic. As expected, the drag coefficients with fins are higher.

Base pressure measurements were taken using a one-channel infrared telemetry system. The technique works and gives repeatable calibration data. However, the accuracy of the wind-on measurements is questionable because of the following:

a) the lack of temperature readings for the transducer and associated electronics inside the model. (The frequency output is a strong function of temperature.)

b) very small pressure differences ($p_{base} \simeq p_s$) determined by subtracting a large number from another large number

c) a differential transducer with a pressure range of 2 psi, which is too large considering $p_{base} \simeq p_s$.

Surface flow visualization using both liquid crystals and pigmented oil flow verified the existence and location of the laminar separation bubble. The oil flow was especially useful in highlighting the separation and reattachment lines.

Comparisons with two simple computational drag prediction schemes were generally poor. These codes were developed to predict drag for simple axisymmetric shapes; they were not designed to accurately predict drag for complicated axisymmetric shapes with separated flow such as the one used in this study. Proper modeling of the laminar separation bubble and the transition location on this bubble are essential to achieve accurate drag prediction in this case.

Suggestions for future work using the model from the present study include:

a) More detailed oil flow studies through the Reynolds number range to better define the separation and reattachment locations.

b) Additional experimental measurements of base pressure to resolve discrepancies between estimates and measurements.

c) Moving the center of gravity of the model to study aerodynamic instabilities without using fins. This may allow testing at higher Reynolds numbers to extend the data base.

d) Fixing transition just ahead of the laminar separation bubble to quantify the lowest drag coefficient obtainable on this body.

Chapter XII

Future of MSBS

The future of Magnetic Suspension and Balance Systems is very promising. Recent conceptual design studies have produced innovative MSBS designs for an 8-foot system to use with a transonic wind tunnel. The cost estimate for the most recent design is approximately 21 million dollars. This design takes advantage of the superconducting model core concept as well as superconducting electromagnets placed efficiently in a single dewar around the test section. It is envisioned that the position sensing system of the future will be a hybrid system incorporating features of both advanced optical position sensing systems and electromagnetic postion sensing systems. This hybrid system would be much more flexible than the present optical systems, allowing the testing of complicated configurations at any attitude. Finally, the improvement in data accuracy by using a MSBS is the result of the elimination of the support interference. The problem of support interference is especially critical at transonic speeds where the model supports are large to handle the high loads.

References

1. Tuttle, M.H.; and Gloss, B.B.: Support Interference of Wind Tunnel Models - A Selective Annotated Bibliography. NASA TM-81909, 1981.

2. Tuttle, M.H.; and Lawing, P.L.: Support Interference of Wind Tunnel Models - A Selective Annotated Bibliography. Supplement to NASA TM-81909, 1984.

3. Lawing, P.L.; Dress, D.A.; and Kilgore, R.A.: Potential Benefits of Magnetic Suspension and Balance Systems. NASA TM-89079, 1987.

4. Basmajian, V.V.; Copeland, A.B.; and Stephens, T.: Studies Related to the Design of a Magnetic Suspension and Balance System. NASA CR-66233, 1966.

5. Boyden, R.P.; Britcher, C.P.; and Tcheng, P.: Status of Wind Tunnel Magnetic Suspension Research. SAE TP-851898, 1985.

6. Tournier, M.; and Laurenceau, P.: Suspension Magnetique d'une Maquette en Soufflierie. La Recherche Aeronautique, No. 59, July-Aug. 1957, pp. 21-27.

7. Tuttle, M.H.; Kilgore, R.A.; and Boyden, R.P.: Magnetic Suspension and Balance Systems - A Selected, Annotated Bibliography. NASA TM-84661, 1983.

8. Britcher, C.; Goodyer, M.J.; Scurlock, R.G.; and Wu, Y.Y.: A flying superconducting magnet and cryostat for magnetic suspension of wind-tunnel models. Cryogenics, vol. 24, no. 4, 1984, pp. 185-189.

9. Bloom, H.L.; et al: Design Concepts and Cost Studies for Magnetic Suspension and Balance Systems. NASA CR-165917, 1982.

10. Boom, R.W.; Eyssa, Y.M.; McIntosh, G.E.; and Abdelsalam, M.K.: Magnetic Suspension and Balance System Study. NASA CR-3082, 1984.

11. Boom, R.W.; Eyssa, Y.M.; McIntosh, G.E.; and Abdelsalam, M.K.: Magnetic Suspension and Balance System Advanced Study. NASA CR-3937, 1985.

12. Kilgore, R.A.; Goodyer, M.J.; Adcock, J.B.; and Davenport, E.E.: The Cryogenic Wind-Tunnel Concept for High Reynolds Number Testing. NASA TN D-7762, 1974.

13. Dress, D.A.; Kilgore, R.A.: Cryogenic wind tunnel research: a global perspective. Cryogenics, vol. 28, no. 1, 1988, pp. 10-21.

14. Matthews, R.K.; Brown, M.D.; and Langford, J.M.: Description and Initial Operation of the AEDC Magnetic Model Suspension Facility Hypersonic Wind Tunnel (E). AEDC TR-70-80, May 1970.

15. Britcher, C.P.: User Guide for the Digital Control System of the NASA/Langley Research Center's 13-Inch Magnetic Suspension and Balance System. NASA CR-178210, 1987.

16. Tcheng, P.; and Schott, T.D.: A Five Component Electro-Optical Positioning System. ICIASF 87CH2449-7, 1987, pp. 322-333.

17. Johnson, W.G., Jr.; and Dress, D.A.: The 13-inch Magnetic Suspension and Balance System Wind Tunnel. Proposed NASA TM, 1988.

18. Parsons, J.S.; Goodson, R.E.; and Goldschmied, F.R.: Shaping of Axisymmetric Bodies for Minimum Drag in Incompressible Flow. Journal of Hydronautics, vol. 8, no. 3, 1974, pp. 100-107.

19. Hansen, R.J.; and Hoyt, J.G.: Laminar-To-Turbulent Transition on a Body of Revolution With an Extended Favorable Pressure Gradient Forebody. Journal of Fluids Engineering, vol. 106, June 1984, pp. 202-210.

20. Hoyt, J.G.: Preliminary Resistance Test of Laminar Flow Submersible. Vol. 1, Hydromechanics Laboratory, U.S. Naval Academy, 1982.

21. Dodbele, S.S.; van Dam, C.P.; Vijgen, P.M.H.W.; and Holmes, B.J.: Shaping of Airplane Fuselages for Minimum Drag. AIAA-86-0316, 1986.

22. Dodbele, S.S.; van Dam, C.P.; and Vijgen, P.M.H.W.: Design of Fuselage Shapes for Natural Laminar Flow. NASA CR-3970, 1986.

23. Holmes, B.J.; Gall, P.D.; Croom, C.C.; Manuel, G.S.; and Kelliher, W.C.: A New Method for Laminar Boundary Layer Transition Visualization in Flight - Color Changes in Liquid Crystal Coatings. NASA TM-87666, 1986.

24. Gall, P.D.; and Holmes, B.J.: Liquid Crystals for High-Altitude In-Flight Boundary Layer Flow Visualization. AIAA-86-2592, 1986.

25. Holmes, B.J.; and Obara, C.J.: Advances in Flow Visualization Using Liquid-Crystal Coatings. SAE TP-871017, 1987.

26. Ames Research Staff: Equations, Tables, and Charts for Compressible Flow. NACA Report 1135, 1953.

27. Glauert, H.: Wind Tunnel Interference on Wings, Bodies and Airscrews. ARC R&M 1566, 1933.

28. Garner, H.C.; Rogers, E.W.E.; Acum, W.E.A.; and Maskell, E.C.: Subsonic Wind Tunnel Wall Corrections. AGARDograph 109, 1966.

29. Batchelor, G.K.: Interference on Wings, Bodies and Airscrews in a Closed Tunnel of Octagonal Section. Report ACA-5, 1944.

30. Fox, R.W.; McDonald, A.T.: Introduction to Fluid Mechanics. Third ed., John Wiley & Sons, Inc., 1985.

31. Hoerner, S.F.: Fluid-Dynamic Drag. Second ed., Published by the author, 1965.

32. Roberts, W.B.: Calculation of Laminar Separation Bubbles and Their Effect on Airfoil Performance. AIAA-79-0285, 1979.

33. Horton, H.P.: Laminar Separation Bubbles in Two and Three Dimensional Incompressible Flow. Ph. D. Thesis, Univerisity of London (Queen Mary College), 1968.

34. Weibust, E.; Bertelrud, A.; and Ridder, S.O.: Experimental and Theoretical Analysis of Laminar Separation Bubbles. AIAA-84-2201, 1984.

35. Holmes, B.J.; Obara, C.J.; and Pfenninger, W.: Private Communication, NASA Langley Research Center, March 1988.

36. Hoyt, J.G.: Private Phone Communication, July 1987.

37. Mueller, T.J.; and Batill, S.M.: Experimental Studies of Separation on a Two-Dimensional Airfoil at Low Reynolds Numbers. AIAA Journal, vol. 20, no. 4, 1982, pp. 457-463.

38. Braslow, A.L.; Knox, E.C.: Simplified Method for Determination of Critical Height of Distributed Roughness Particles for Boundary-Layer Transition at Mach Numbers from 0 to 5. NACA Technical Note 4363, 1958.

39. Tcheng, P.; Schott, T.D.; and Bryant, E.L.: A Miniature, Infrared Pressure Telemetry System. To be presented at the 34th International Instrumentation Symposium, Albuquerque, New Mexico, May 1988.

40. Wolfe, W.P.; and Oberkamph, W.L.: Drag Prediction for Projectiles and Finned Bodies in Incompressible Flow. AIAA-85-0104, 1985.

41. Wolfe, W.P.; and Oberkamph, W.L.: SANDRAG - A Computer Code for Predicting Drag of Bodies of Revolution at Zero Angle of Attack in Incompressible Flow. SAND85-0515, April 1985.

42. Nakayama, A.; and Patel, V.C.: Calculation of the Viscous Resistance of Bodies of Revolution. Journal of Hydronautics, vol. 8, no. 4, 1974, pp. 154-162.

43. Patel, V.C.: A Simple Integral Method for the Calculation of Thick Axisymmetric Turbulent Boundary Layers. The Aeronautical Quarterly, vol. 25, 1974, pp. 47-58.

44. Granville, P.S.: The Calculation of Viscous Drag of Bodies of Revolution. Rept. 849, David Taylor Model Basin, Washington, D.C., 1953.

45. van Driest, E.R.; and Blumer, C.B.: Boundary Layer Transition: Freestream Turbulence and Pressure Gradient Effects. AIAA Journal, vol. 1, no. 6, June 1963, pp. 1303-1306.

Table I

List of nondimensional parameters that define the shape of the laminar flow body of revolution

$r_n = 0.50$	$x_i = 0.80$
$f_n = 4.5$	$r_i = 0.50$
$x_m = 0.5555$	$s_i = 2.0$
$k_i = 1.50$	$t = 0.3$

Table II
Laminar flow body of revolution model coordinates

x, in	z, in
0.0000	0.0000
0.0010	0.0163
0.0020	0.0231
0.0040	0.0327
0.0060	0.0400
0.0080	0.0462
0.0100	0.0517
0.0150	0.0634
0.0200	0.0732
0.0250	0.0819
0.0300	0.0898
0.0400	0.1037
0.0500	0.1161
0.0600	0.1273
0.0700	0.1377
0.0800	0.1474
0.0900	0.1565
0.1000	0.1651
0.2000	0.2359
0.3000	0.2917
0.4000	0.3399
0.5000	0.3832
0.6000	0.4232
0.7000	0.4605
0.8000	0.4958
0.9000	0.5293
1.0000	0.5614
1.2000	0.6218
1.4000	0.6781
1.6000	0.7308
1.8000	0.7805
2.0000	0.8274
2.2000	0.8717
2.4000	0.9136
2.6000	0.9532
2.8000	0.9907
3.0000	1.0259
3.2000	1.0592
3.4000	1.0904
3.6000	1.1196
3.8000	1.1468
4.0000	1.1722
4.2000	1.1956
4.4000	1.2172
4.6000	1.2369
4.8000	1.2547
5.0000	1.2707
5.2000	1.2849
5.4000	1.2972
5.6000	1.3077

x, in	z, in
5.8000	1.3164
6.0000	1.3243
6.2000	1.3284
6.4000	1.3317
6.6000	1.3332
6.6660	1.3333
6.8000	1.3329
7.0000	1.3297
7.2000	1.3225
7.4000	1.3100
7.6000	1.2910
7.8000	1.2645
8.0000	1.2300
8.2000	1.1868
8.4000	1.1348
8.5000	1.1055
8.6000	1.0740
8.7000	1.0404
8.8000	1.0048
8.9000	0.9673
9.0000	0.9280
9.1000	0.8872
9.2000	0.8449
9.3000	0.8015
9.4000	0.7571
9.4500	0.7346
9.5000	0.7120
9.5500	0.6894
9.6000	0.6667
9.6500	0.6440
9.7000	0.6215
9.7500	0.5994
9.8000	0.5778
9.8500	0.5569
9.9000	0.5368
10.0000	0.4994
10.1000	0.4663
10.2000	0.4378
10.3000	0.4141
10.4000	0.3953
10.5000	0.3811
10.6000	0.3713
10.7000	0.3654
10.8000	0.3629
11.0000	0.3659
11.2000	0.3752
11.4000	0.3861
11.6000	0.3947
11.8000	0.3992
12.0000	0.4000

Table III

Corrected drag coefficients for laminar flow body of revolution

$R_L \times 10^{-5}$	$C_{D,\ wet} \times 10^2$
3.645	1.179
4.376	1.201
5.047	1.155
5.608	1.121
6.894	1.050
7.290	1.023
7.972	0.969
8.482	0.922
8.964	0.854
9.406	0.786
10.071	0.675
10.775	0.594
11.159	0.546
11.538	0.523
12.199	0.485
12.575	0.451
12.979	0.465
13.405	0.451

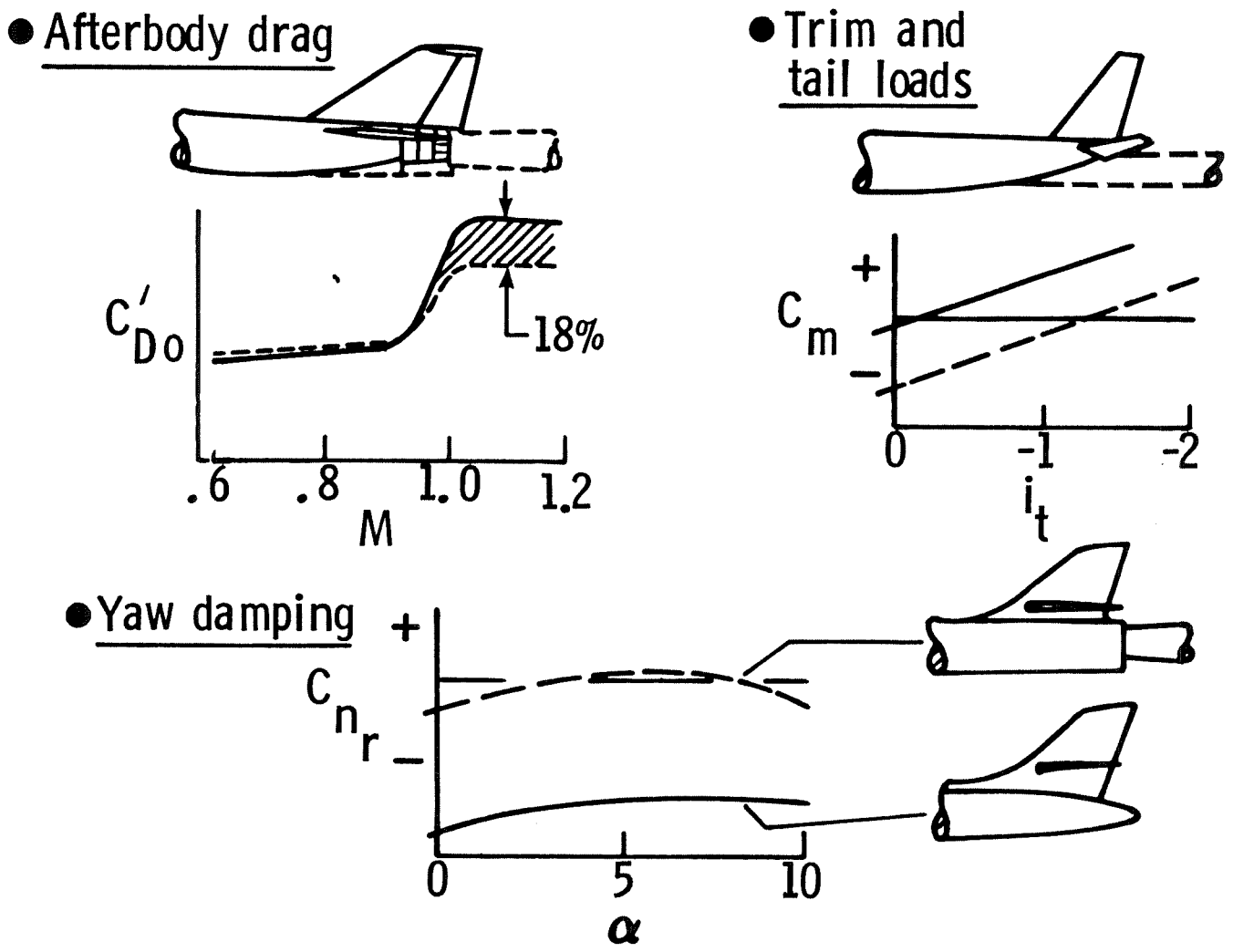

Figure 1. - Examples of model support problems.

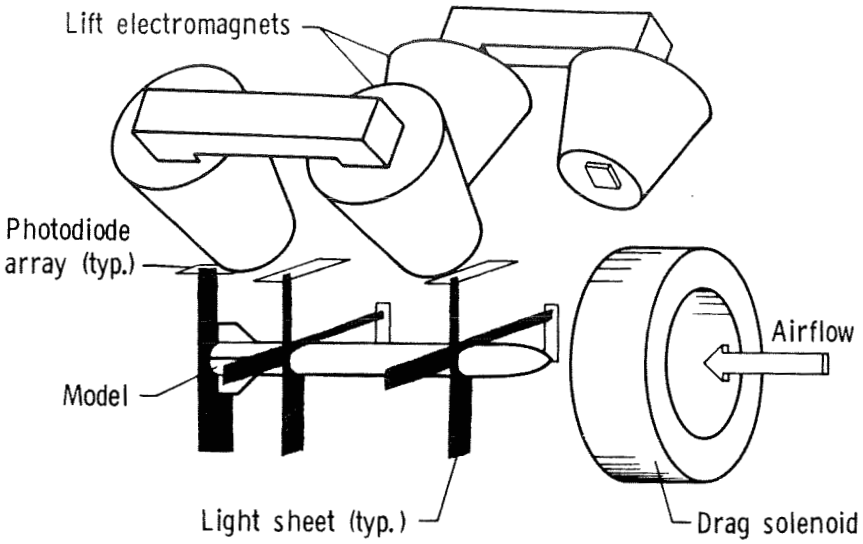

a) Sketch.

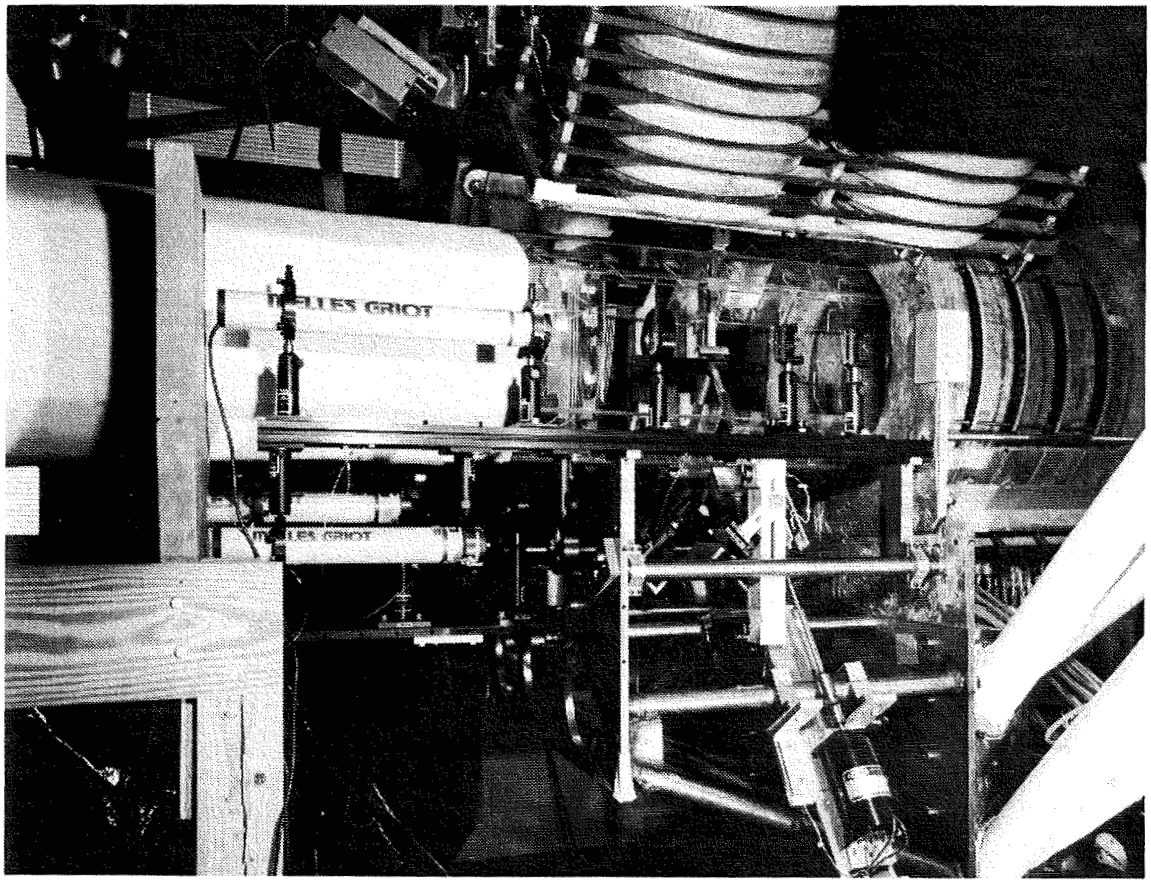

b) Photograph.

Figure 2. - Sketch and photograph of 13″ MSBS.

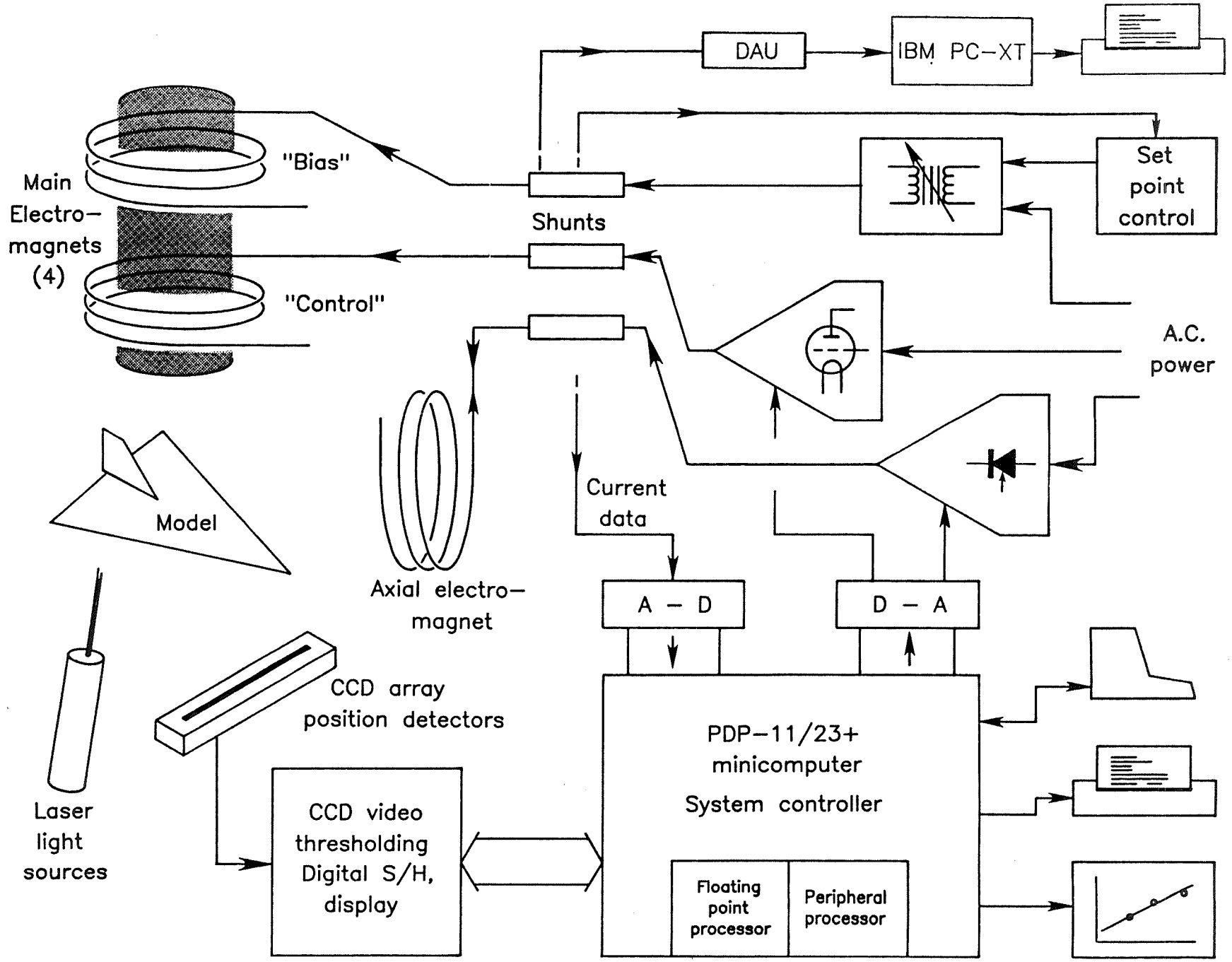

Figure 3. - Block diagram of 13" MSBS hardware.

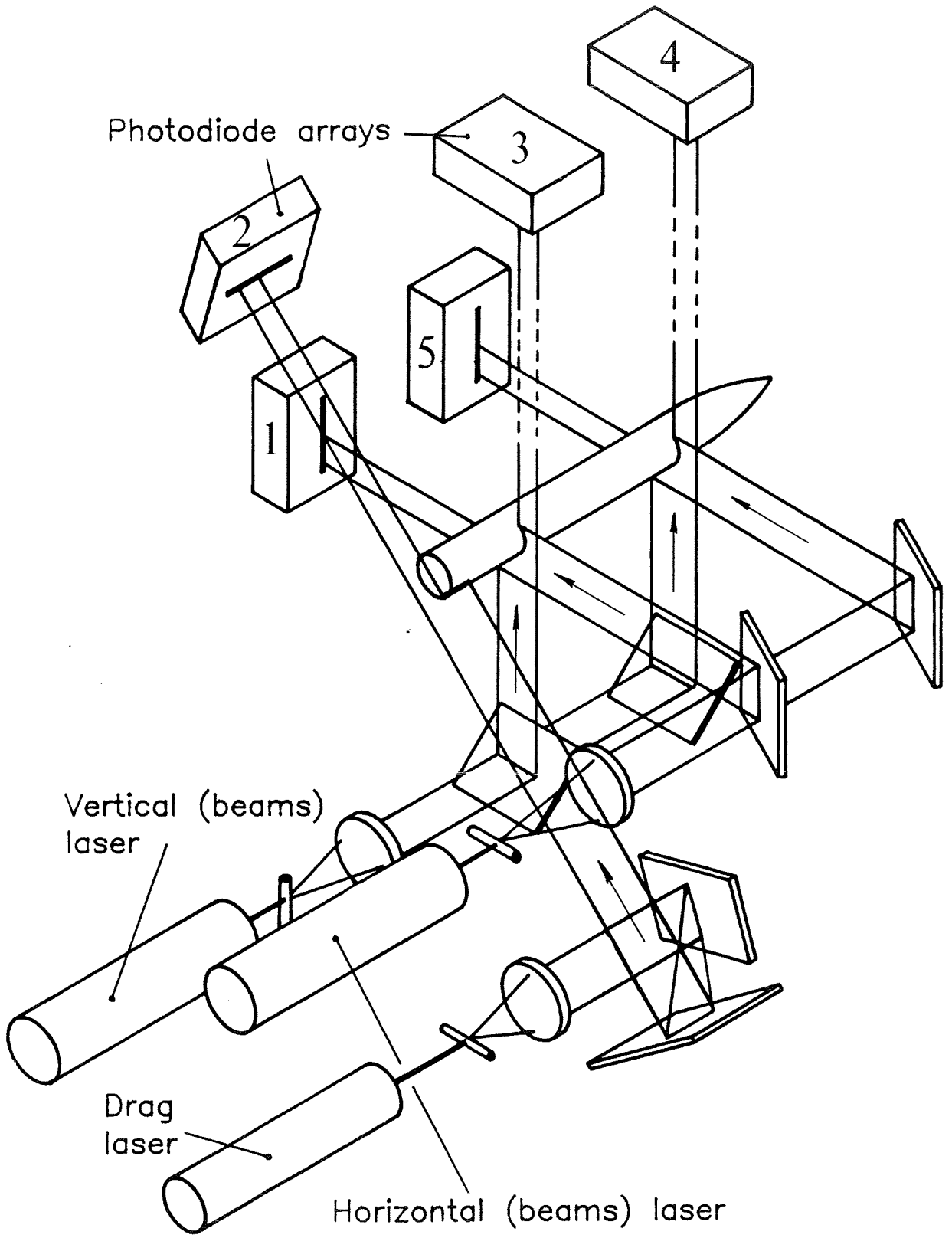

Figure 4. - Schematic diagram of position sensor system.

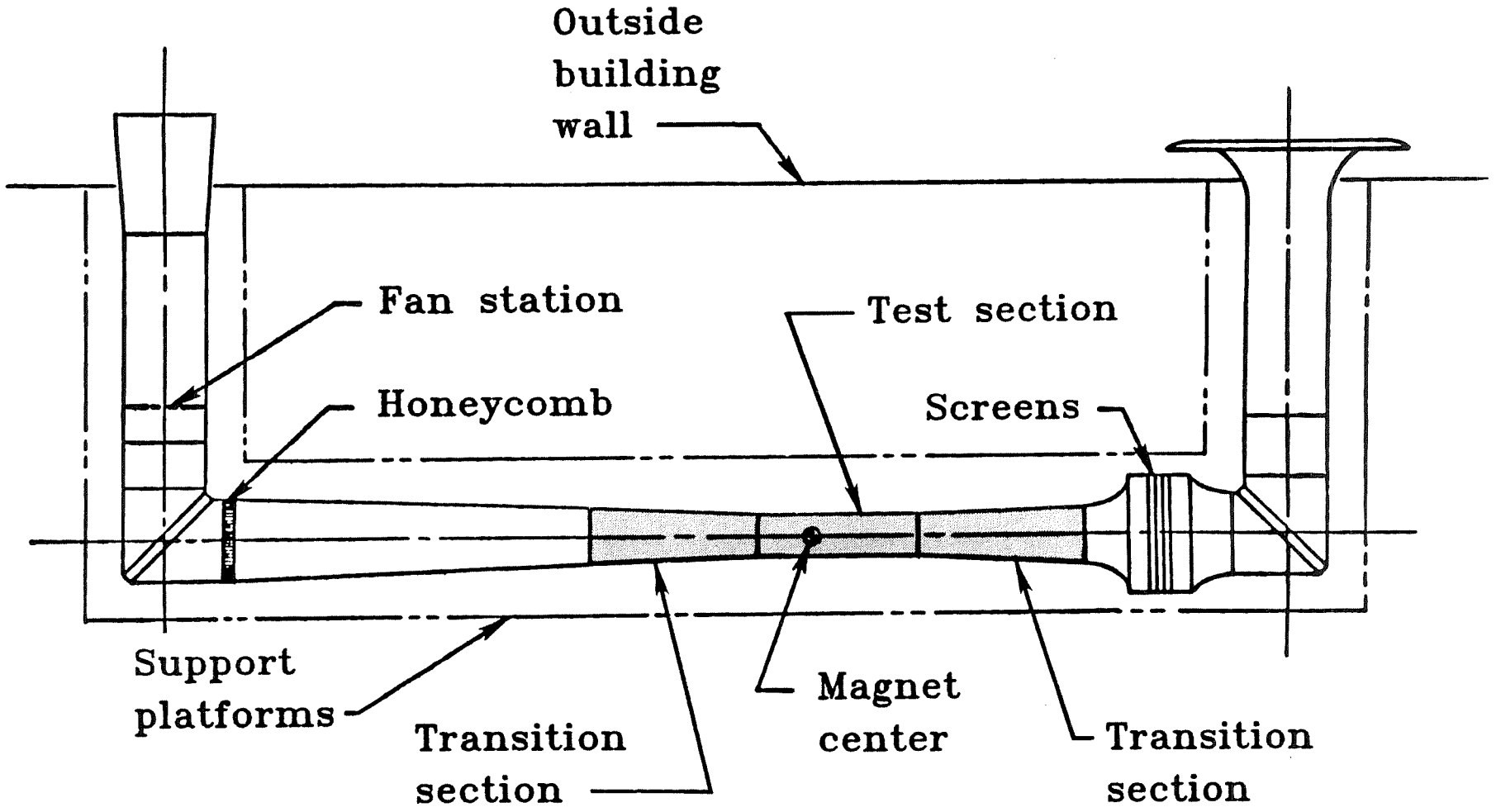

Figure 5. - 13" MSBS wind tunnel layout.

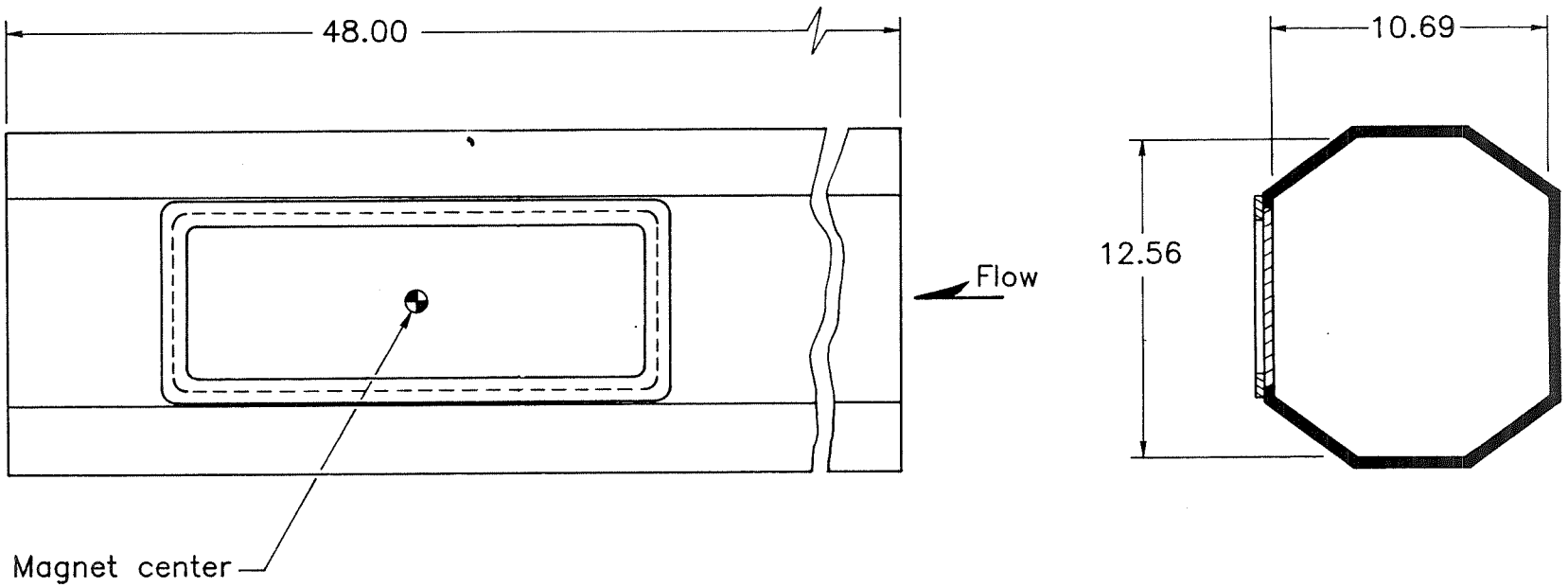

Figure 6. - Sketch of 13" MSBS wind tunnel test section.
(Dimensions are in inches.)

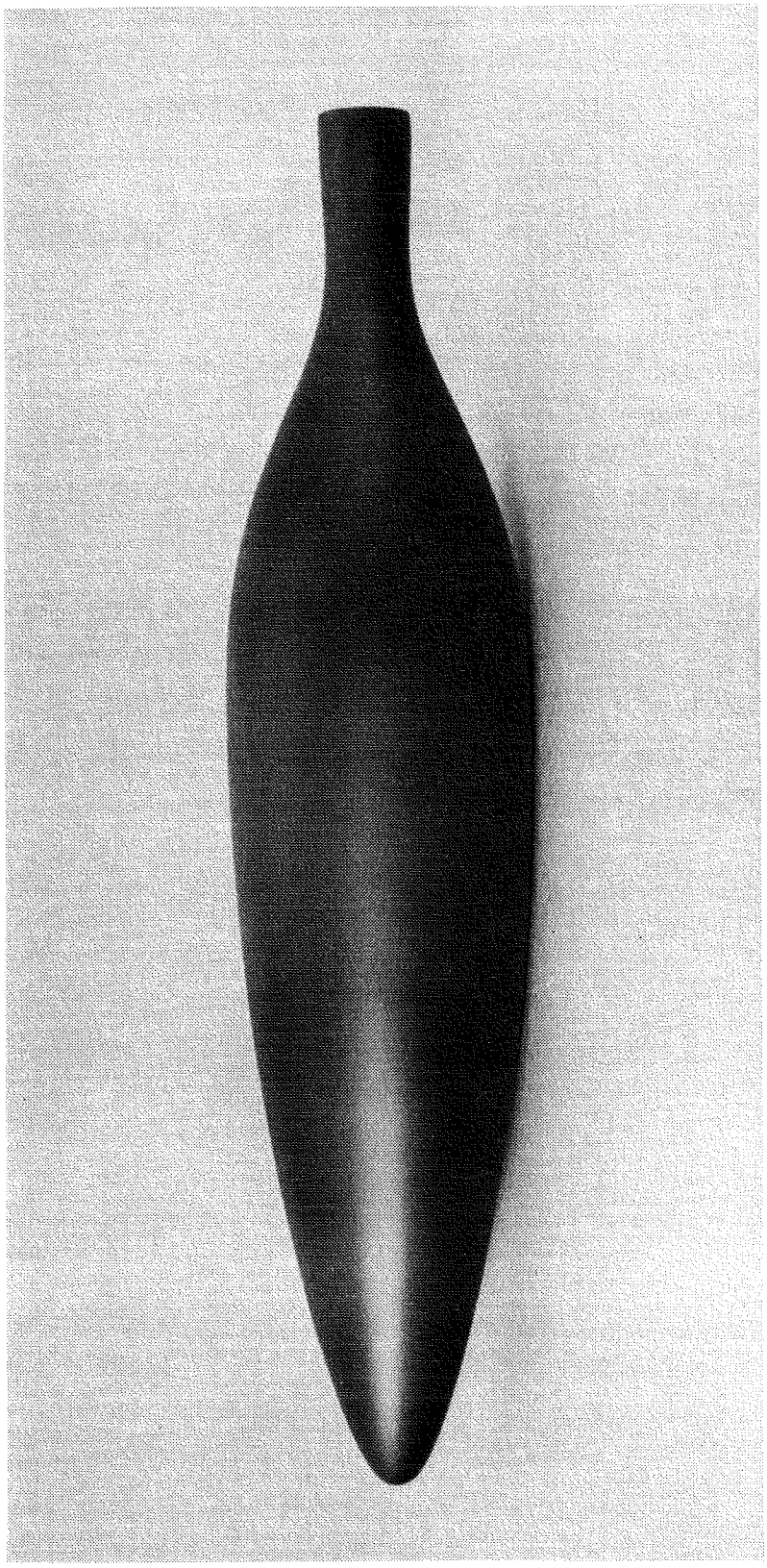

Figure 7. - Photograph of model.

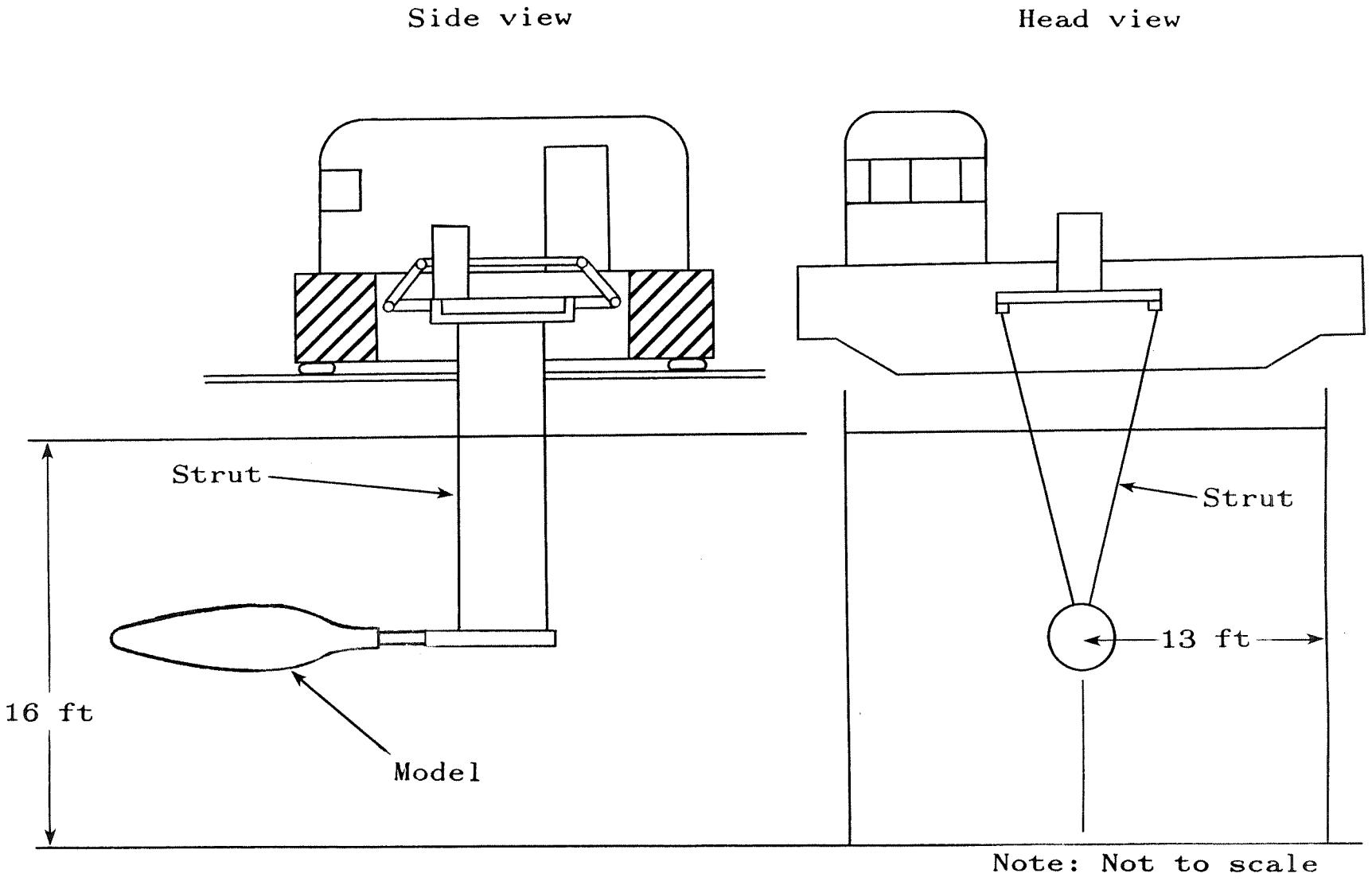

Figure 8. - Sketch of Navy test setup for laminar flow body of revolution. (From reference 20).

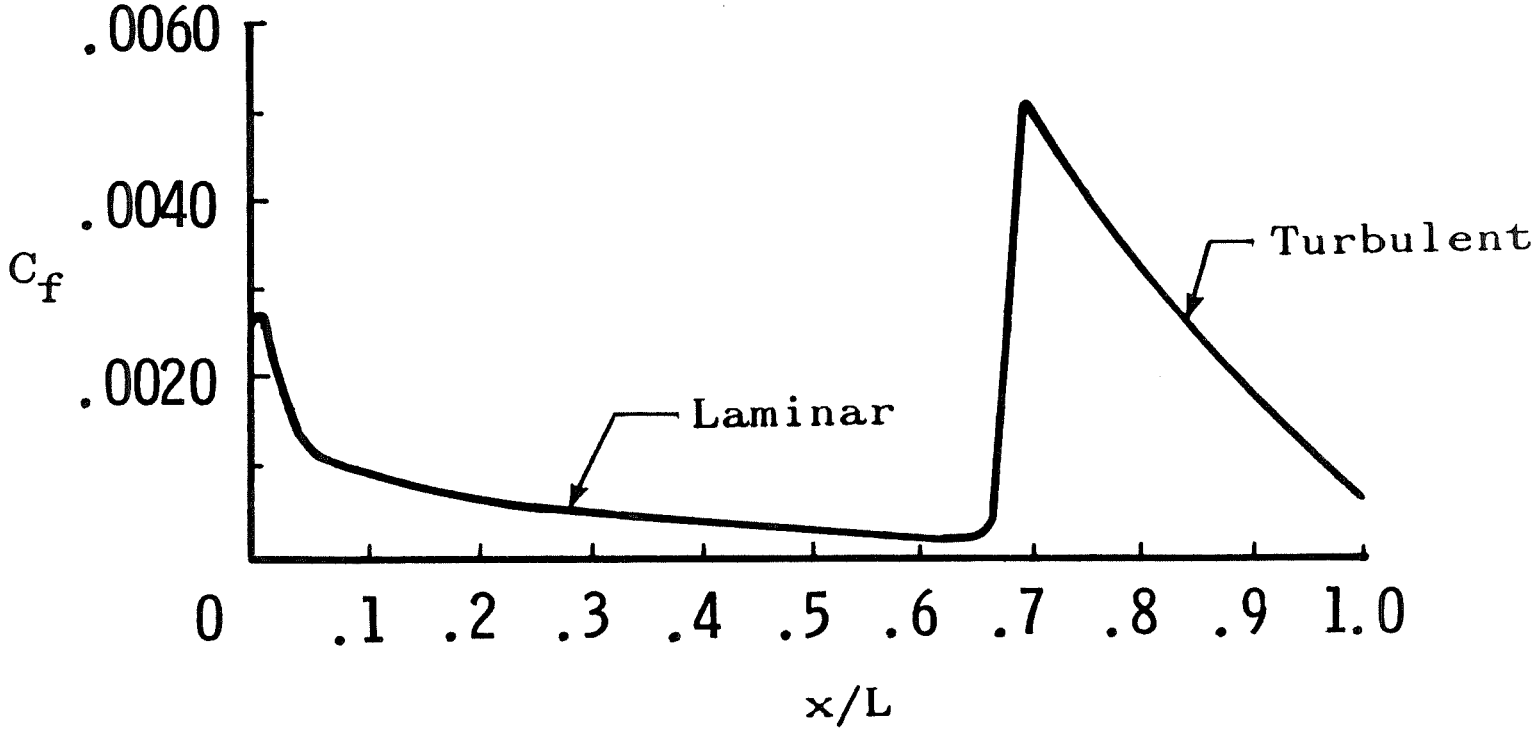

Figure 9. - Skin-friction coefficient for a typical natural laminar flow airfoil. (From reference 24).

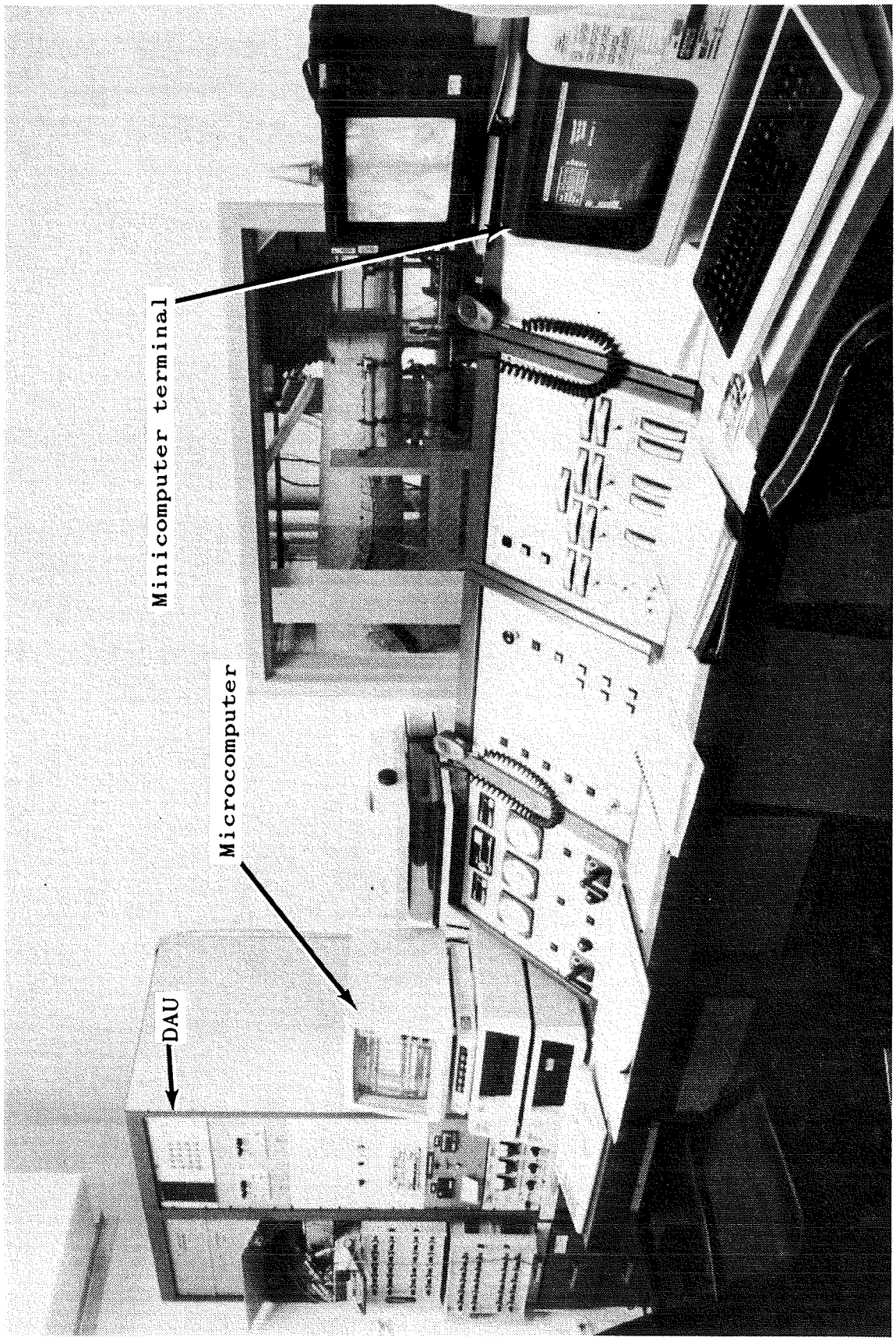

Figure 10. - Photograph of control room.

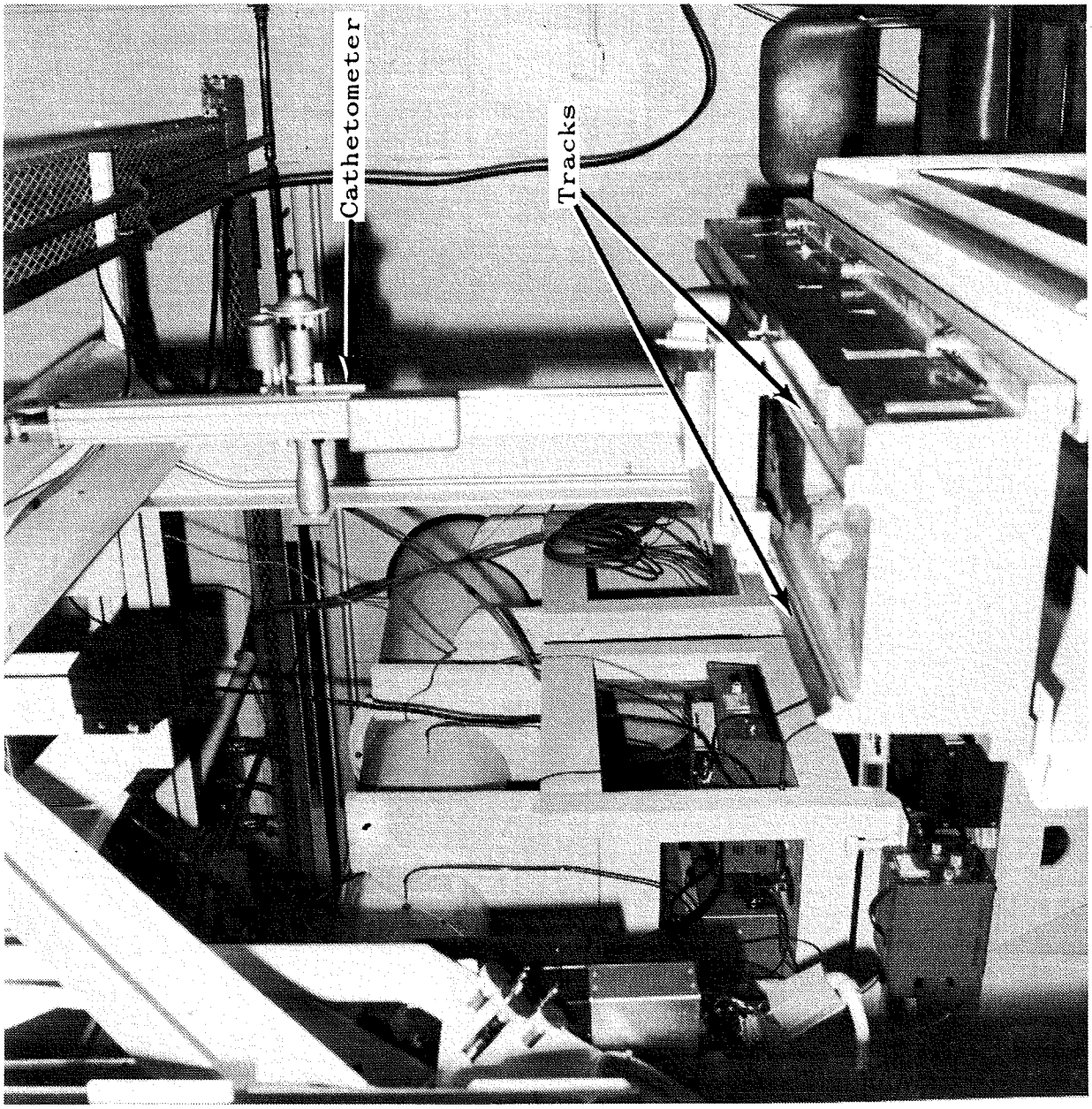

Figure 11. - Photograph of optical cathetometer on tracks.

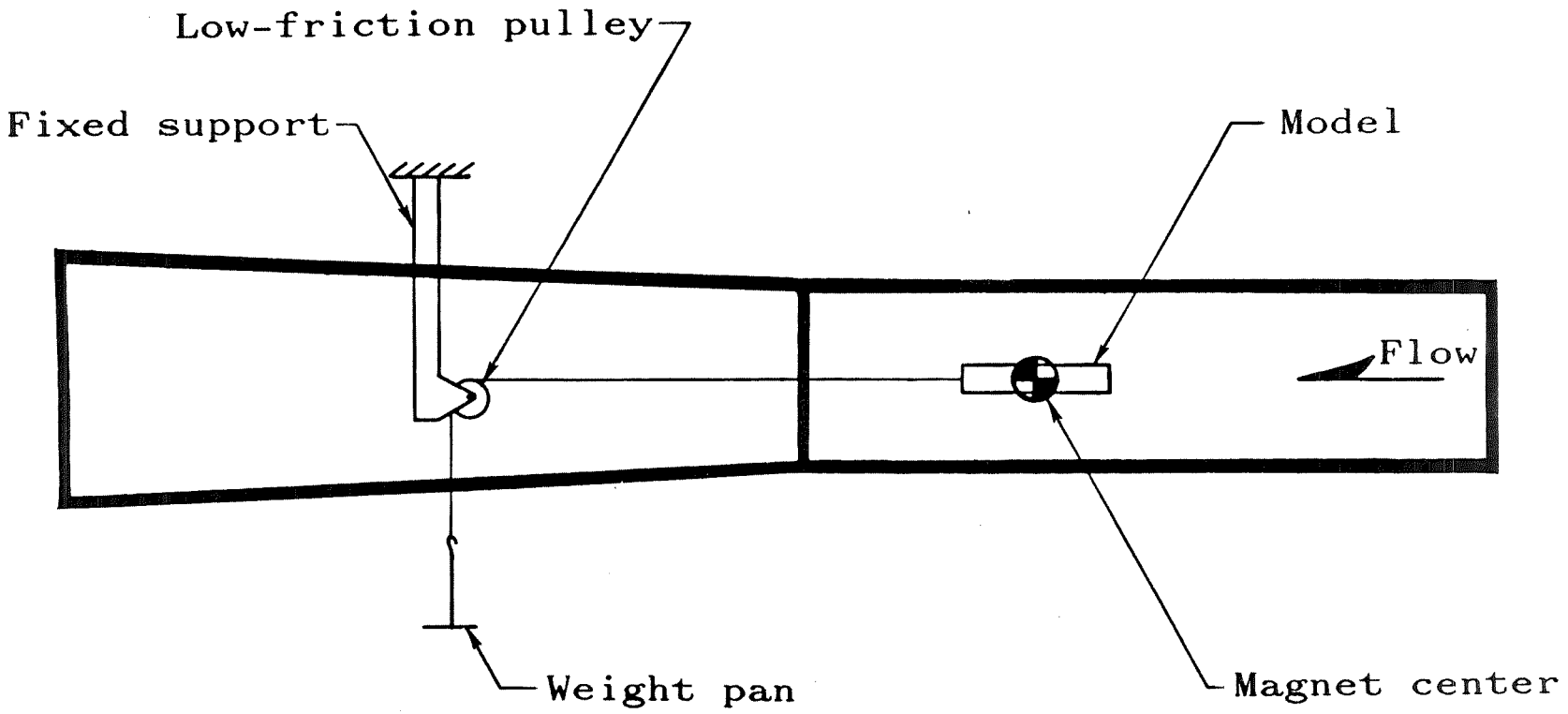

Figure 12. - Sketch of drag calibration setup.

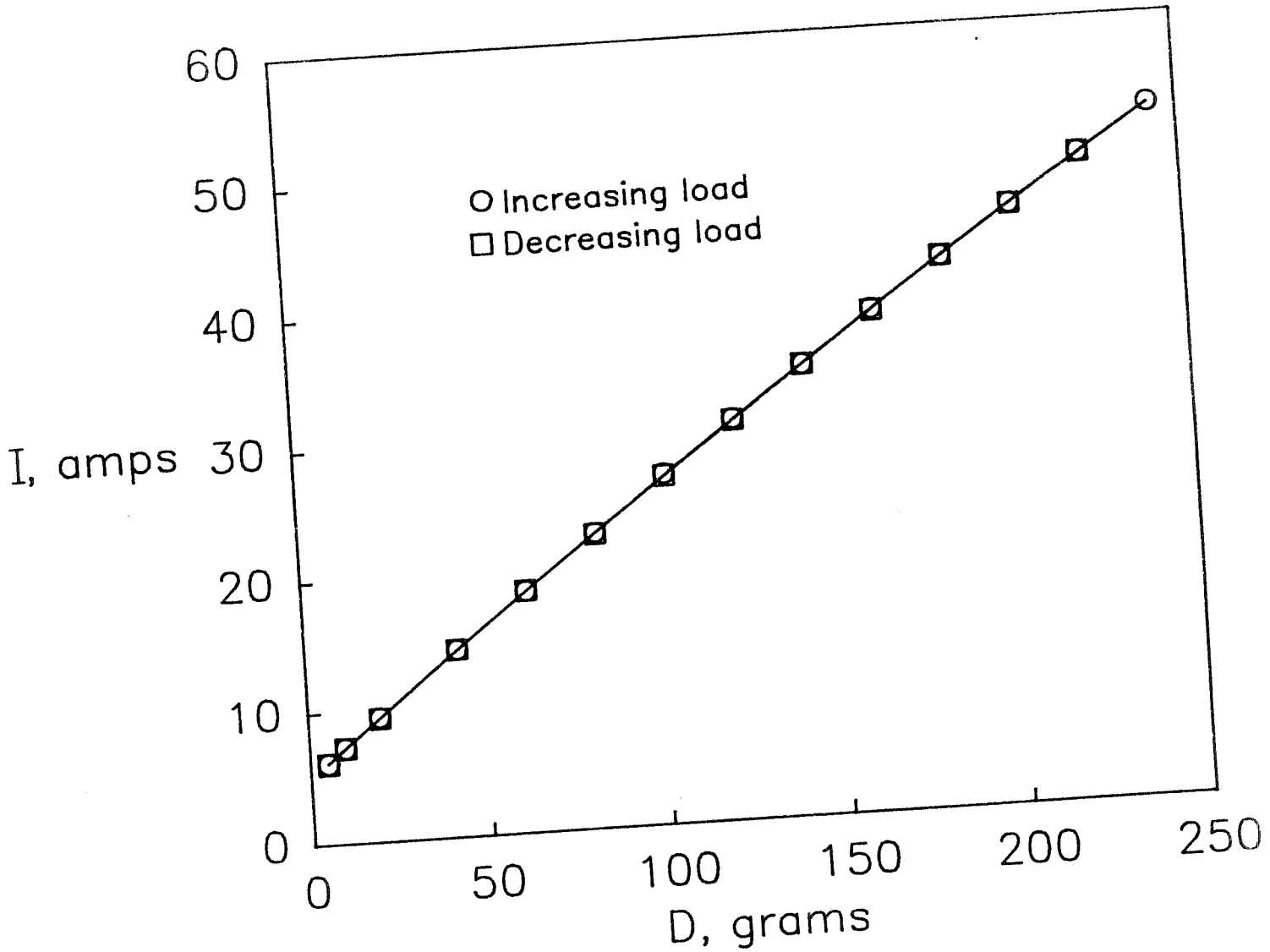

Figure 13. - Drag force calibration for laminar flow body.

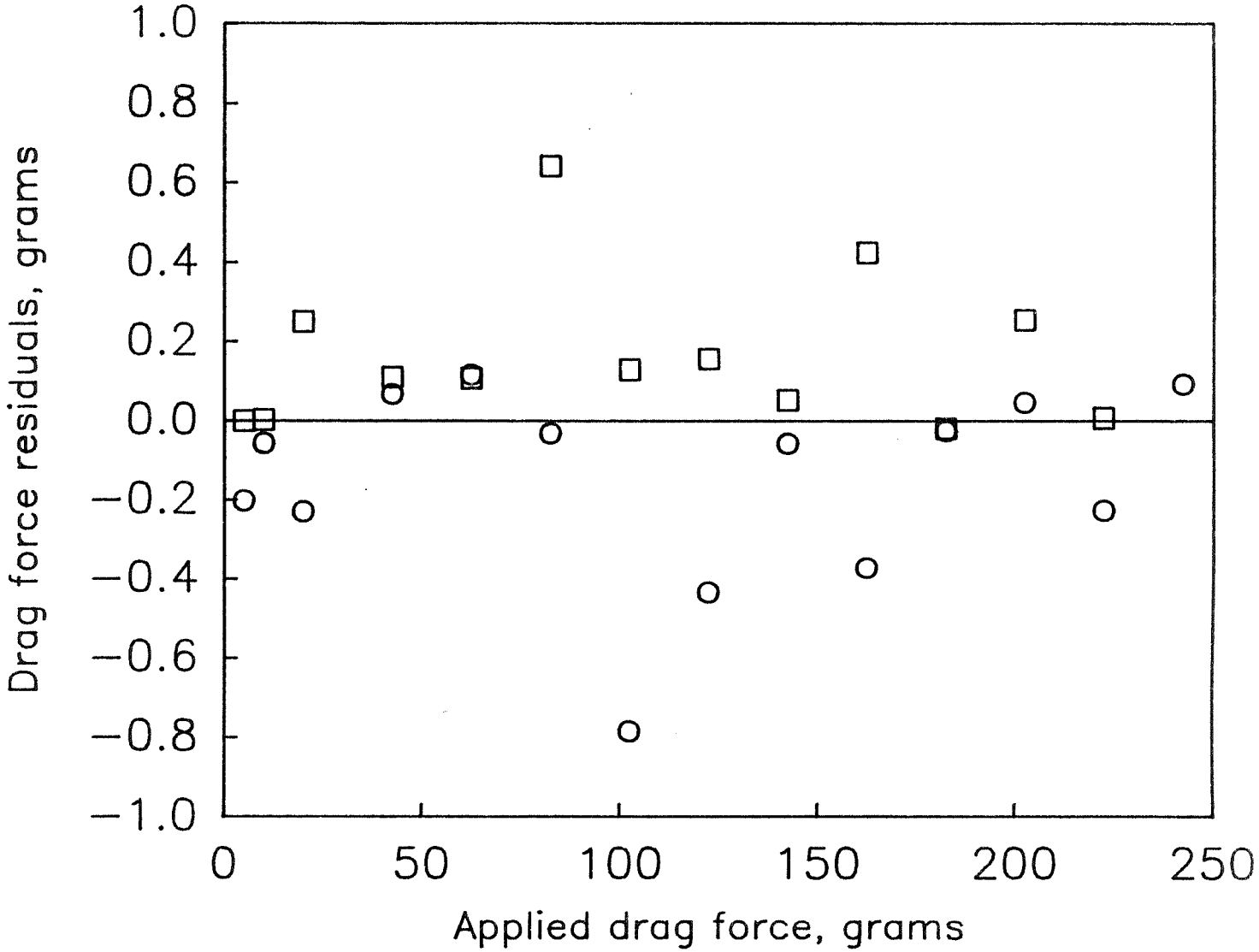

Figure 14. - Residuals of drag force calibration for laminar flow body.

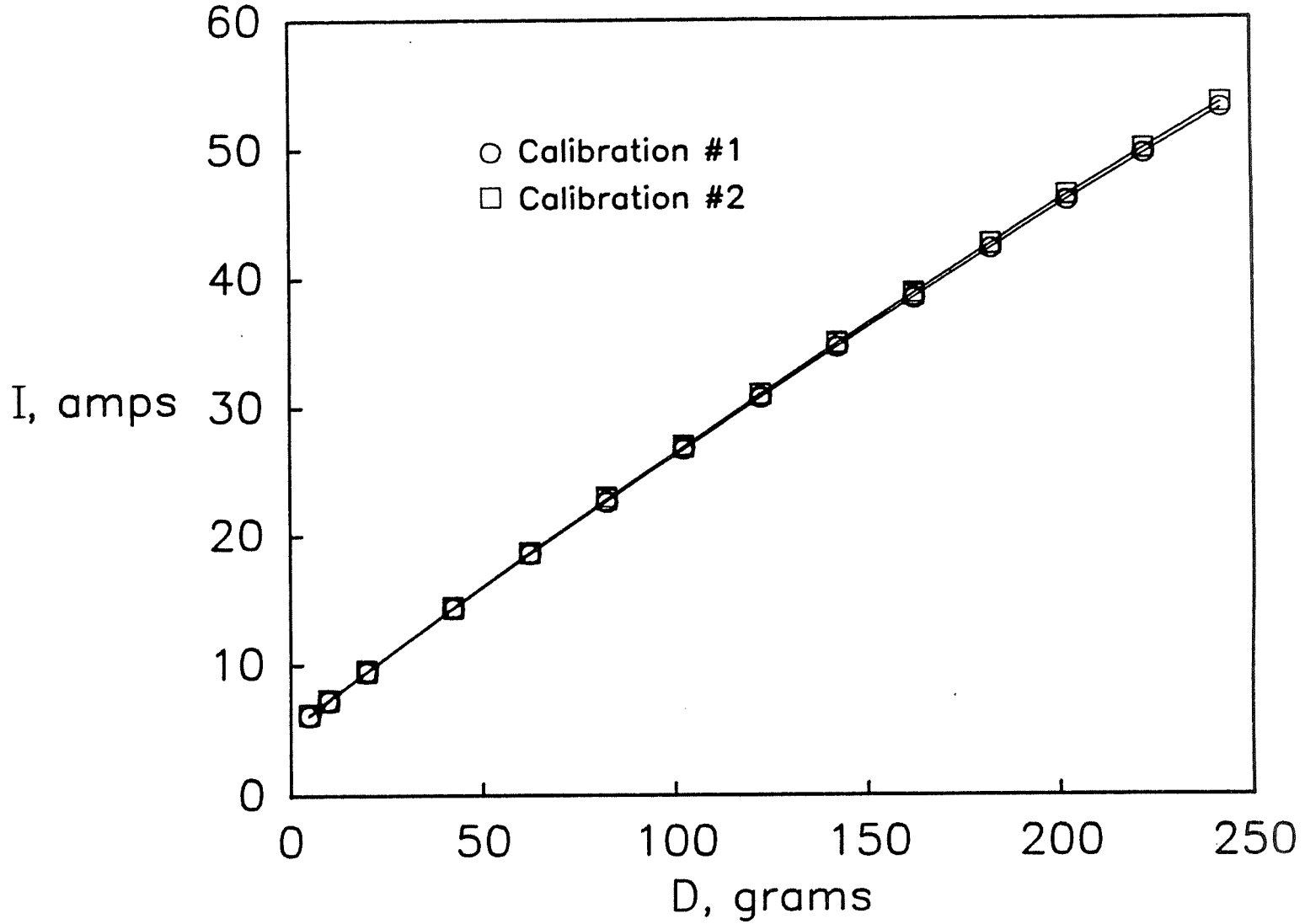

Figure 15. - Repeatability of drag force calibration for laminar flow body.

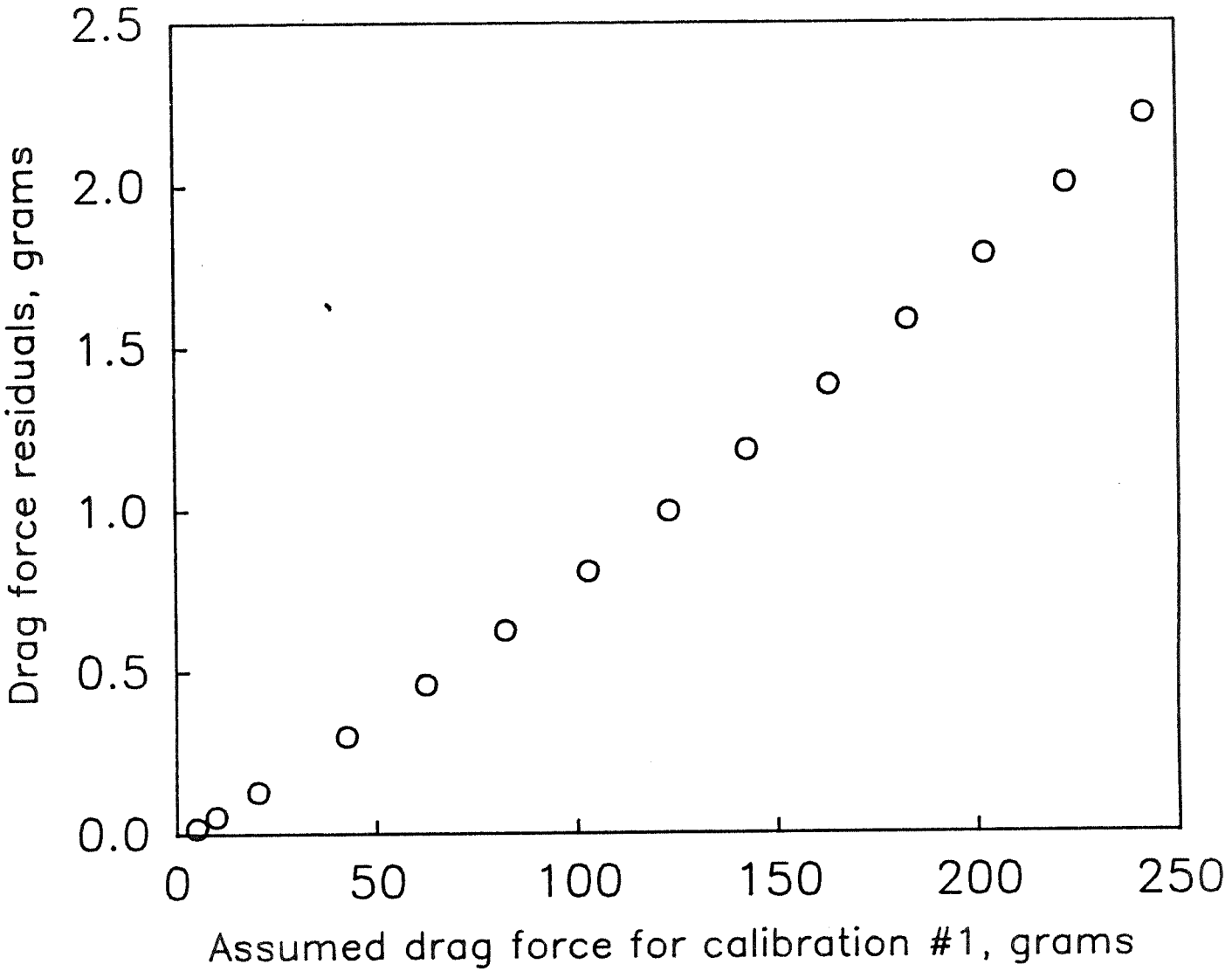

Figure 16. - Comparison of two drag force calibrations for laminar flow body.

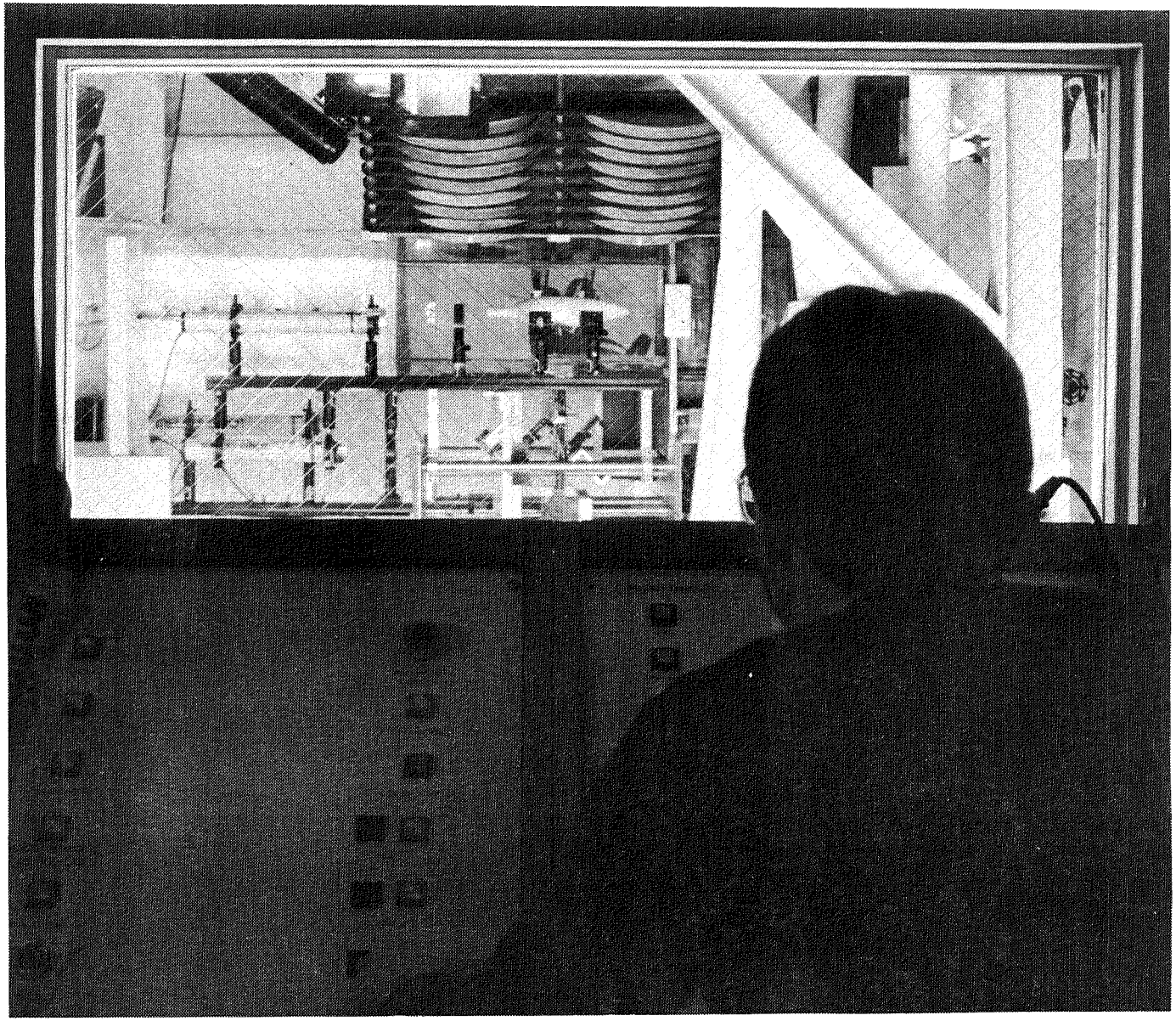

Figure 17. - Photograph of 13″ MSBS. View from control room.

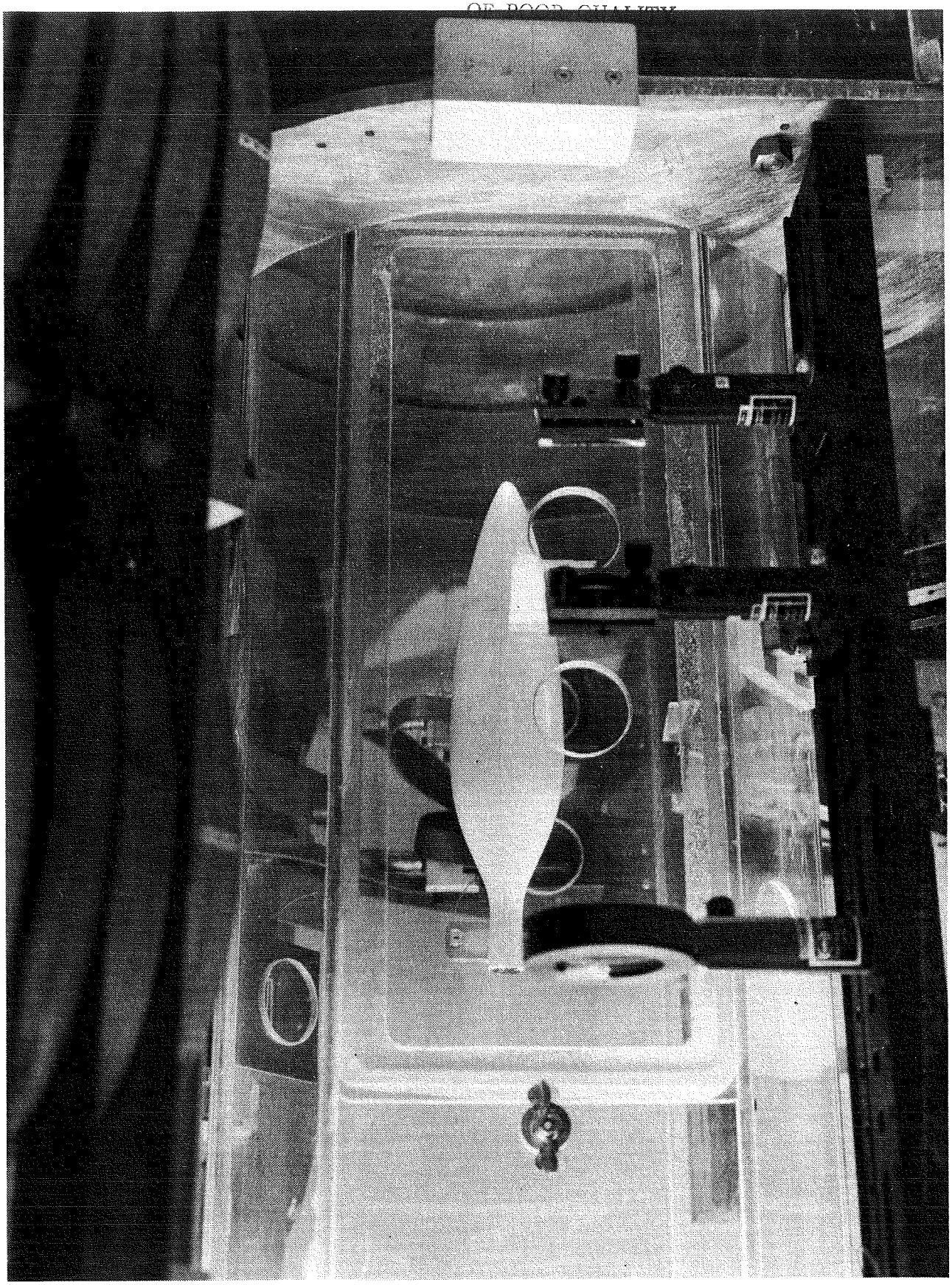

Figure 18. - Photograph of laminar flow body in suspension in 13" MSBS.

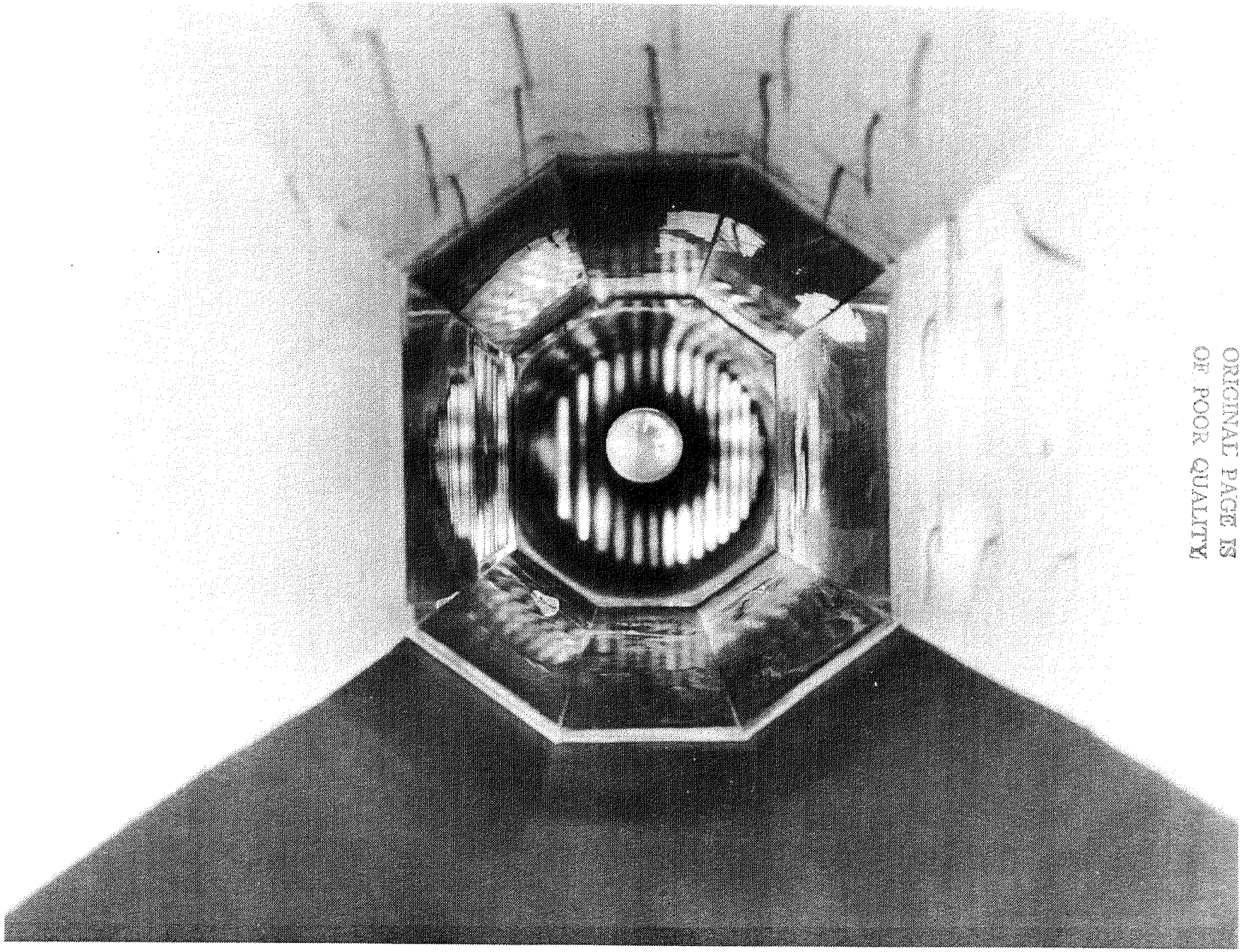

Figure 19. - Photograph of laminar flow body in suspension in 13″ MSBS. View from contraction section of wind tunnel.

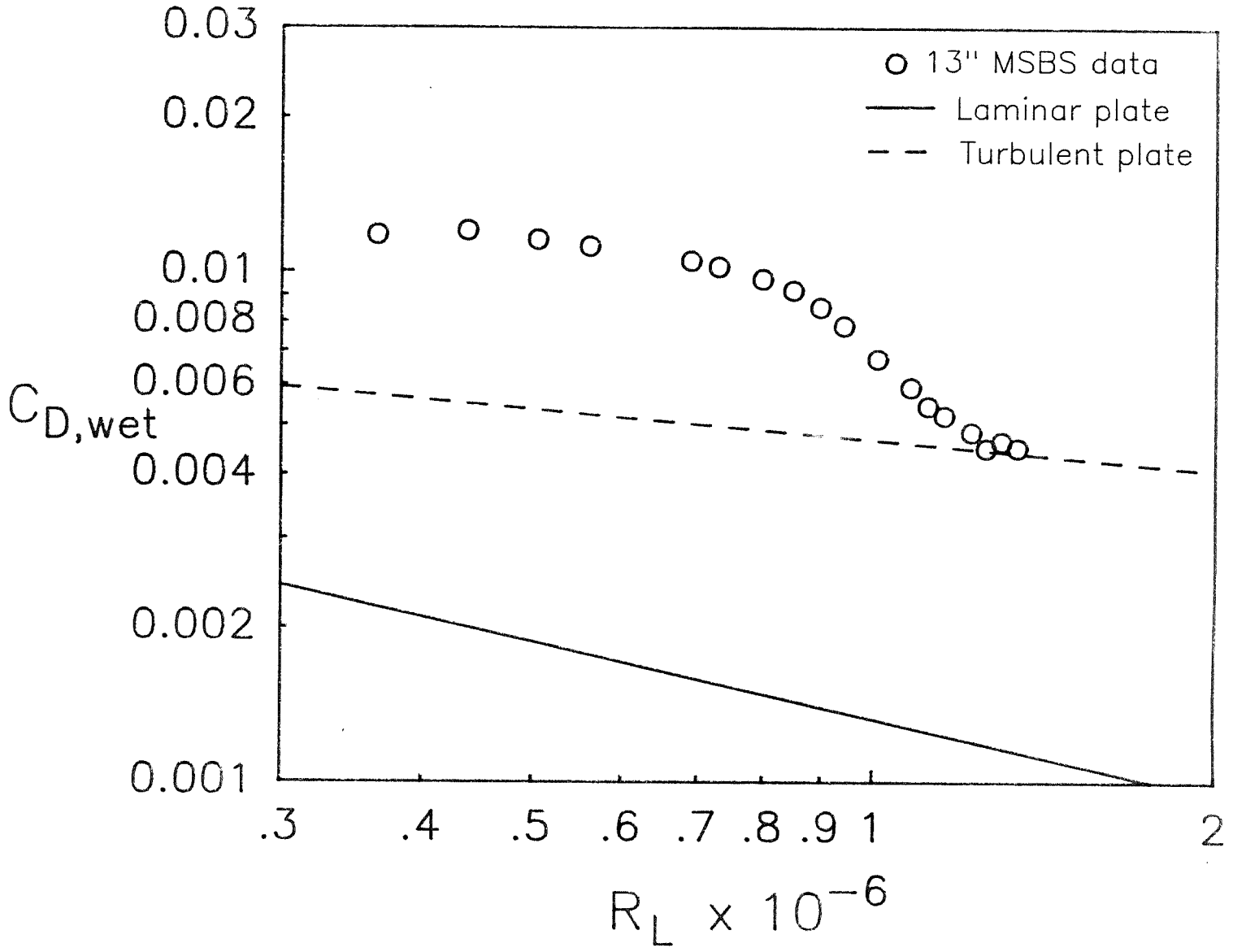

Figure 20. - Drag characteristics of laminar flow body.

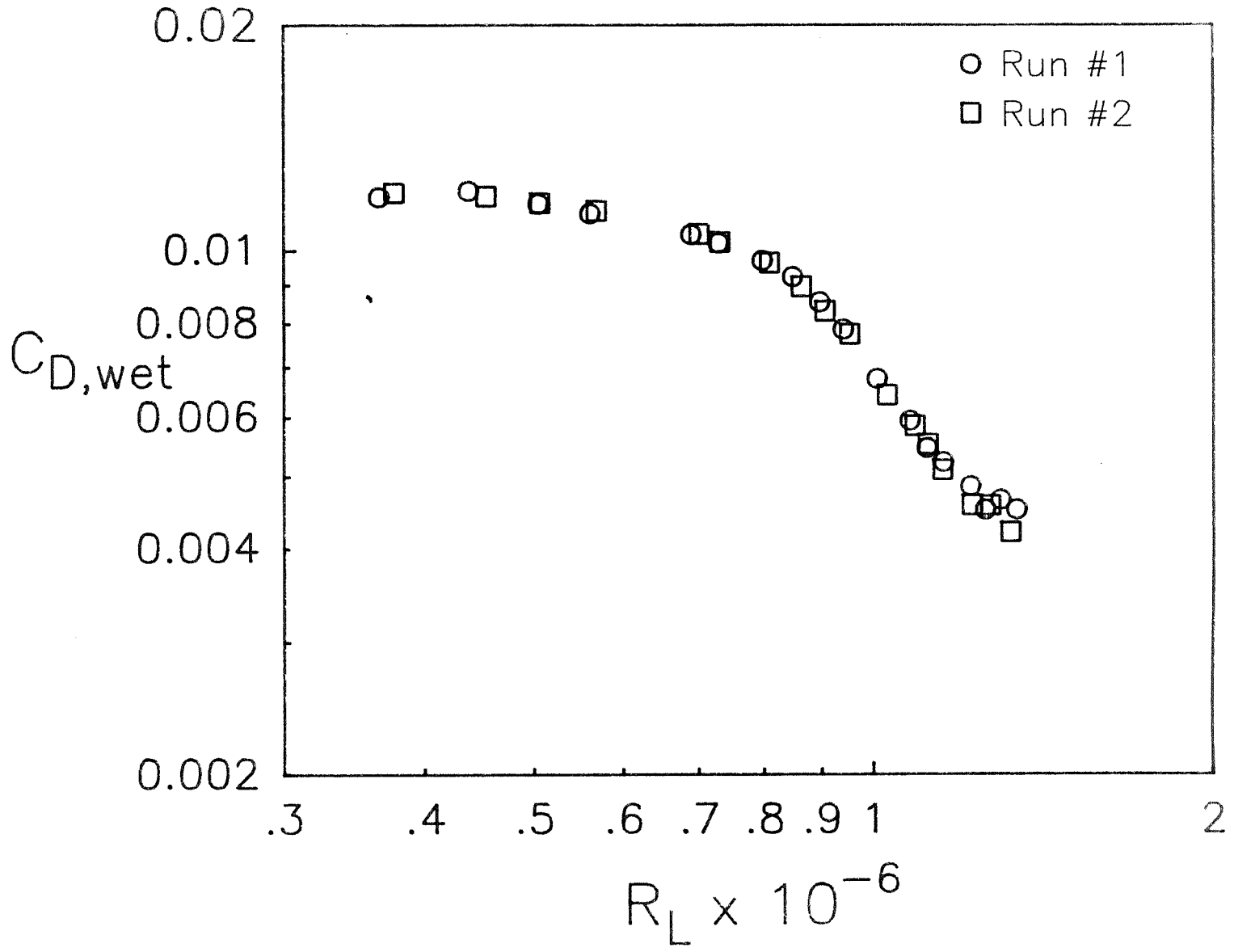

Figure 21. - Repeatabilty of drag characteristics of laminar flow body.

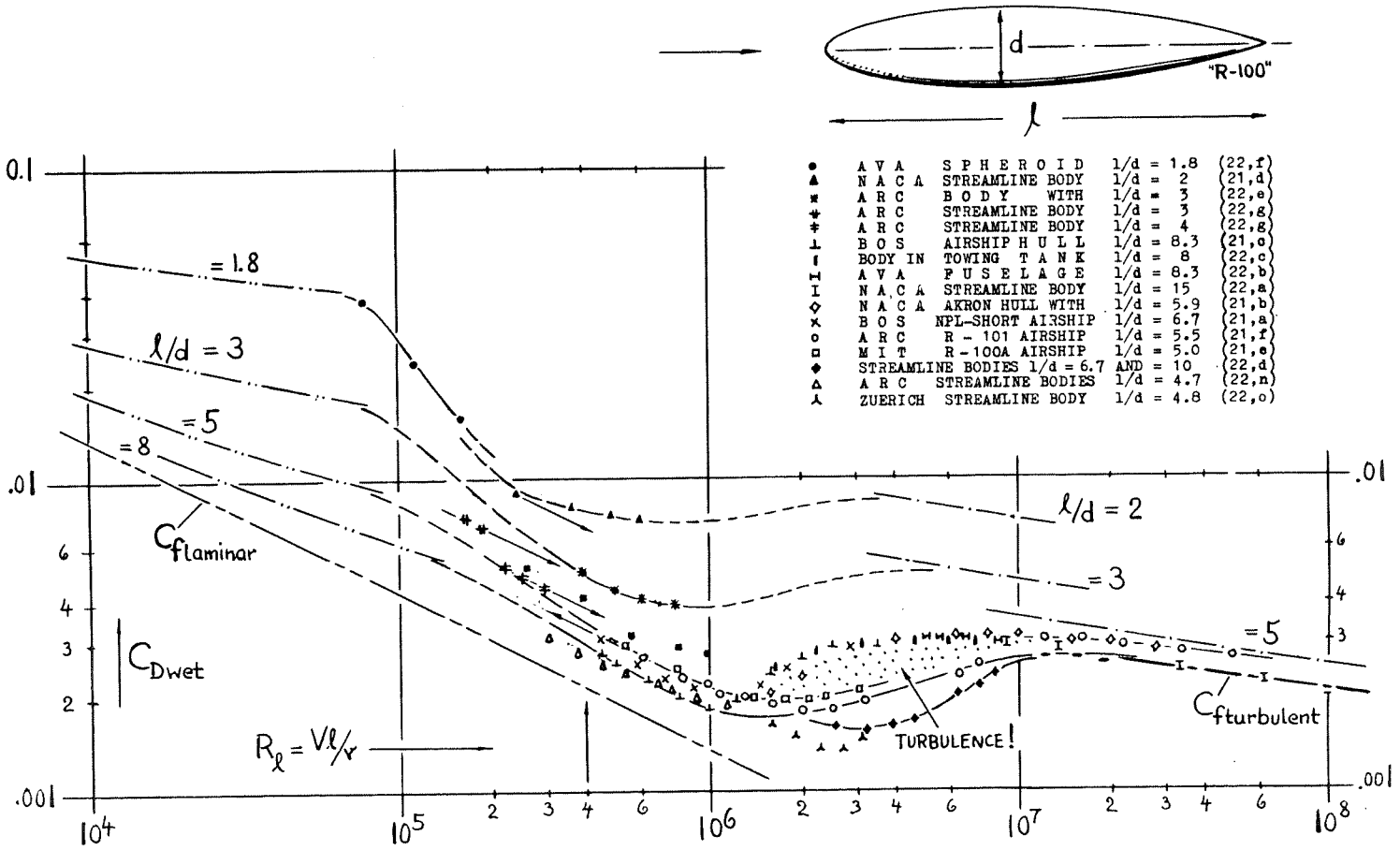

Figure 22. - Drag coefficient trends for streamlined bodies of revolution. (From reference 30.)

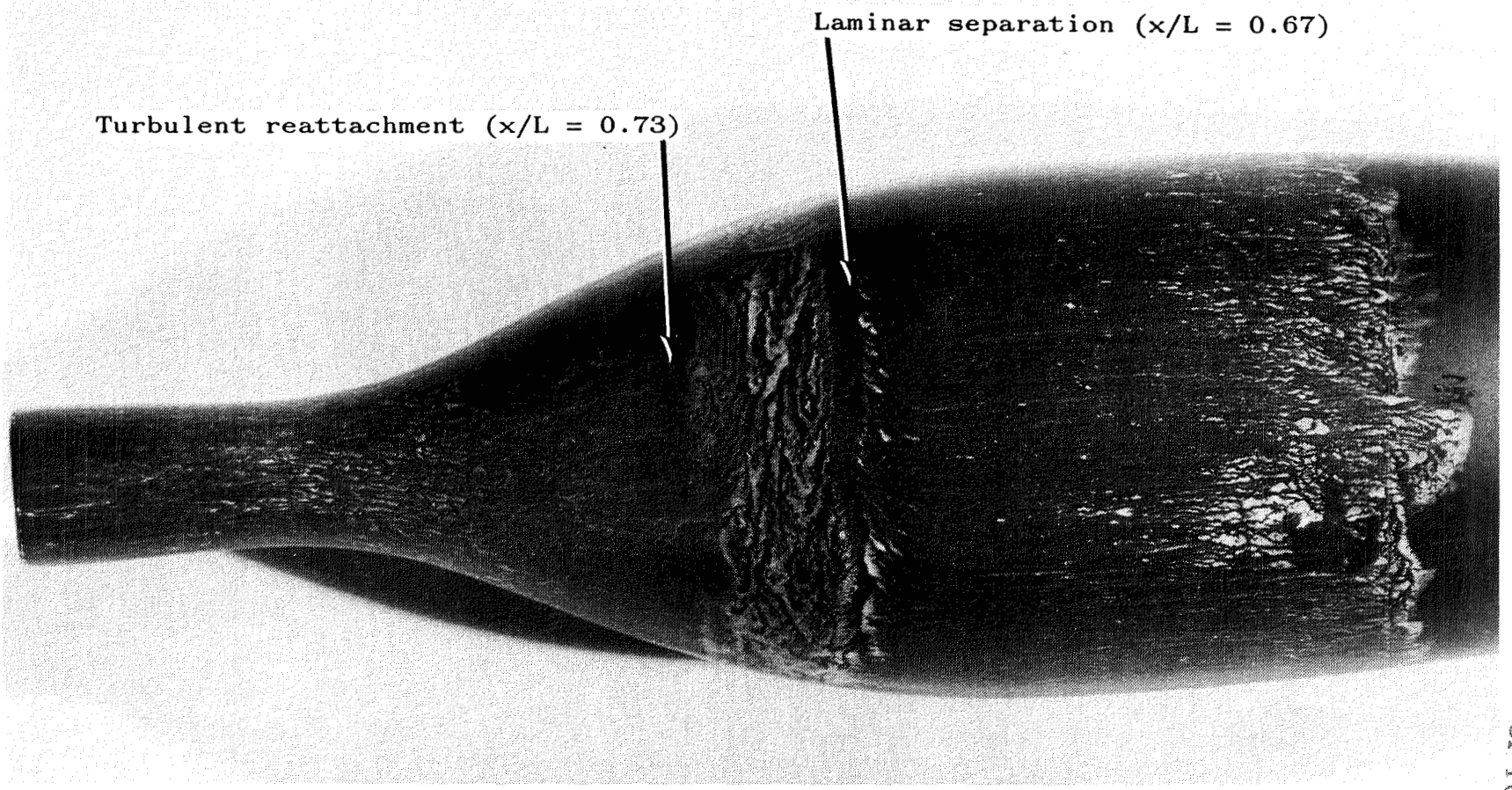

Figure 23. - Photograph of oil flow visualization. Free transition. $R_L = 1.2 \times 10^6$.

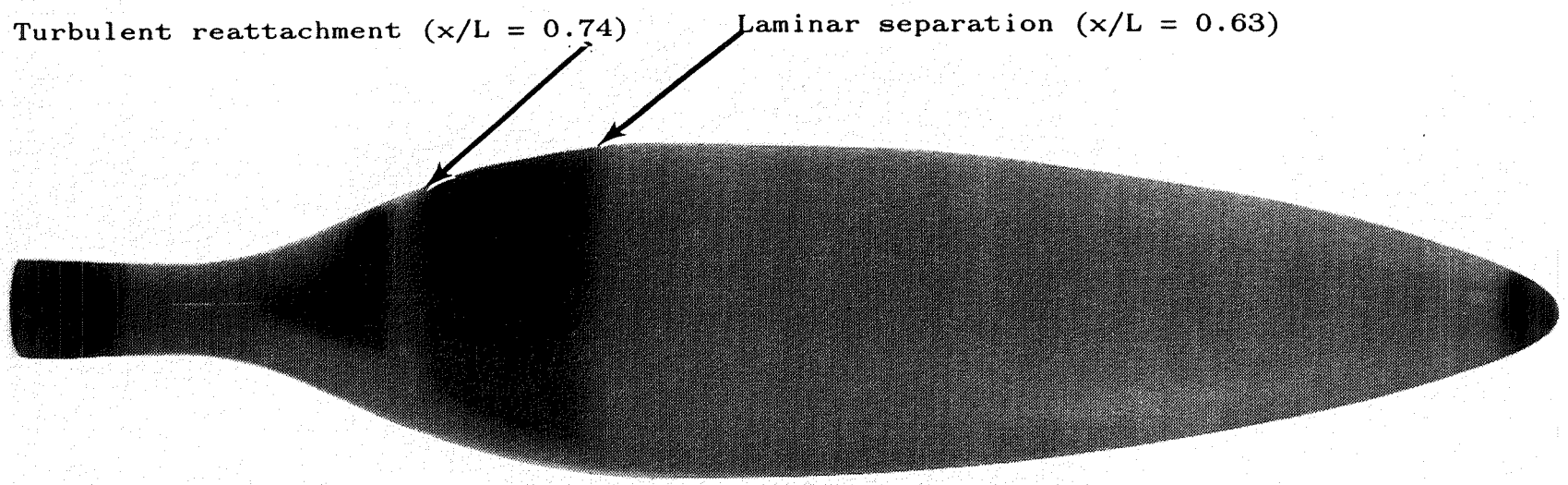

Figure 24. - Photograph of liquid crystal flow visualization. Free transition. $R_L = 1.2 \times 10^6$. (†See footnote on page 21.)

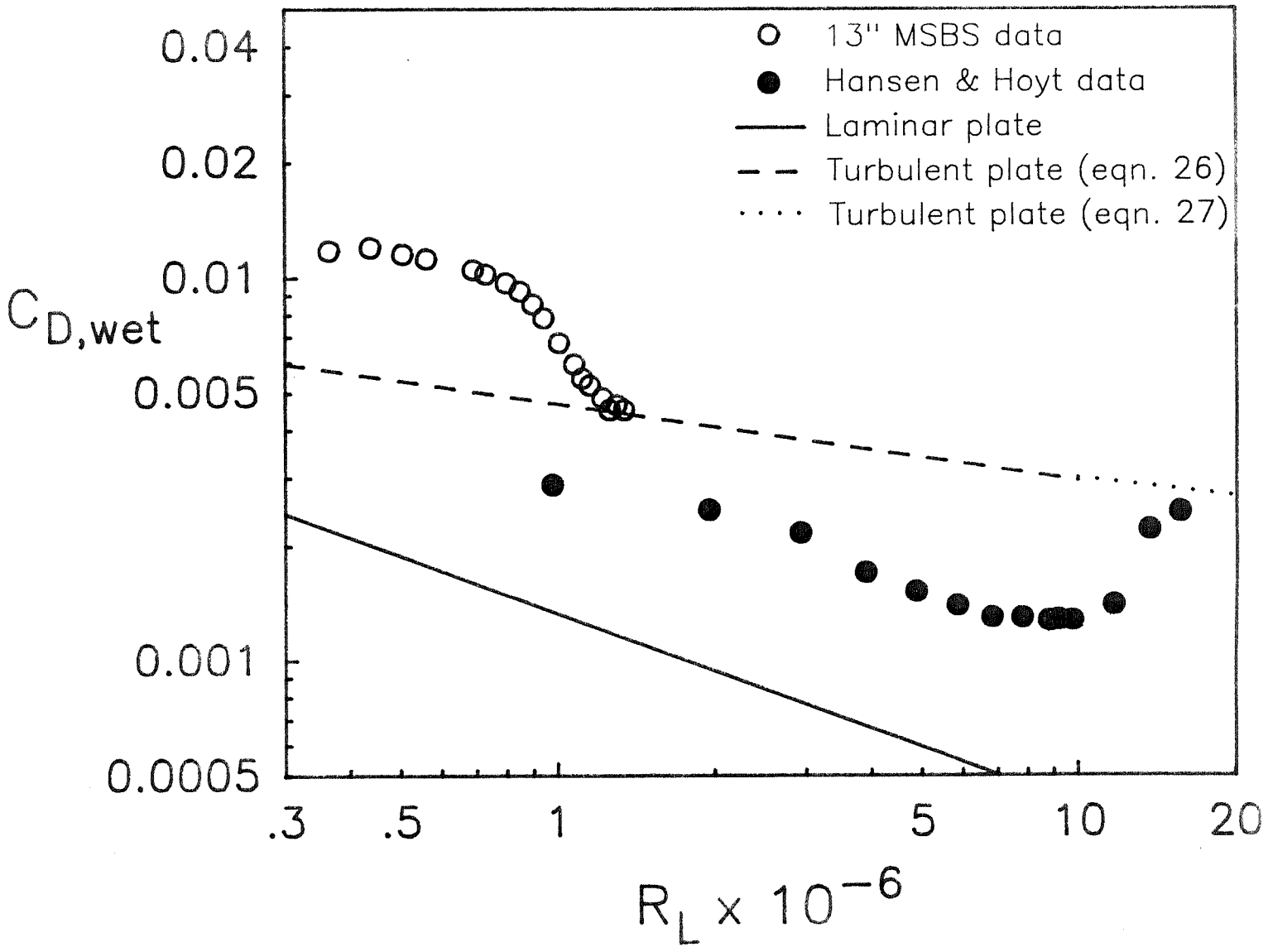

Figure 25. - Comparison of drag characteristics with uncorrected Hansen & Hoyt data.

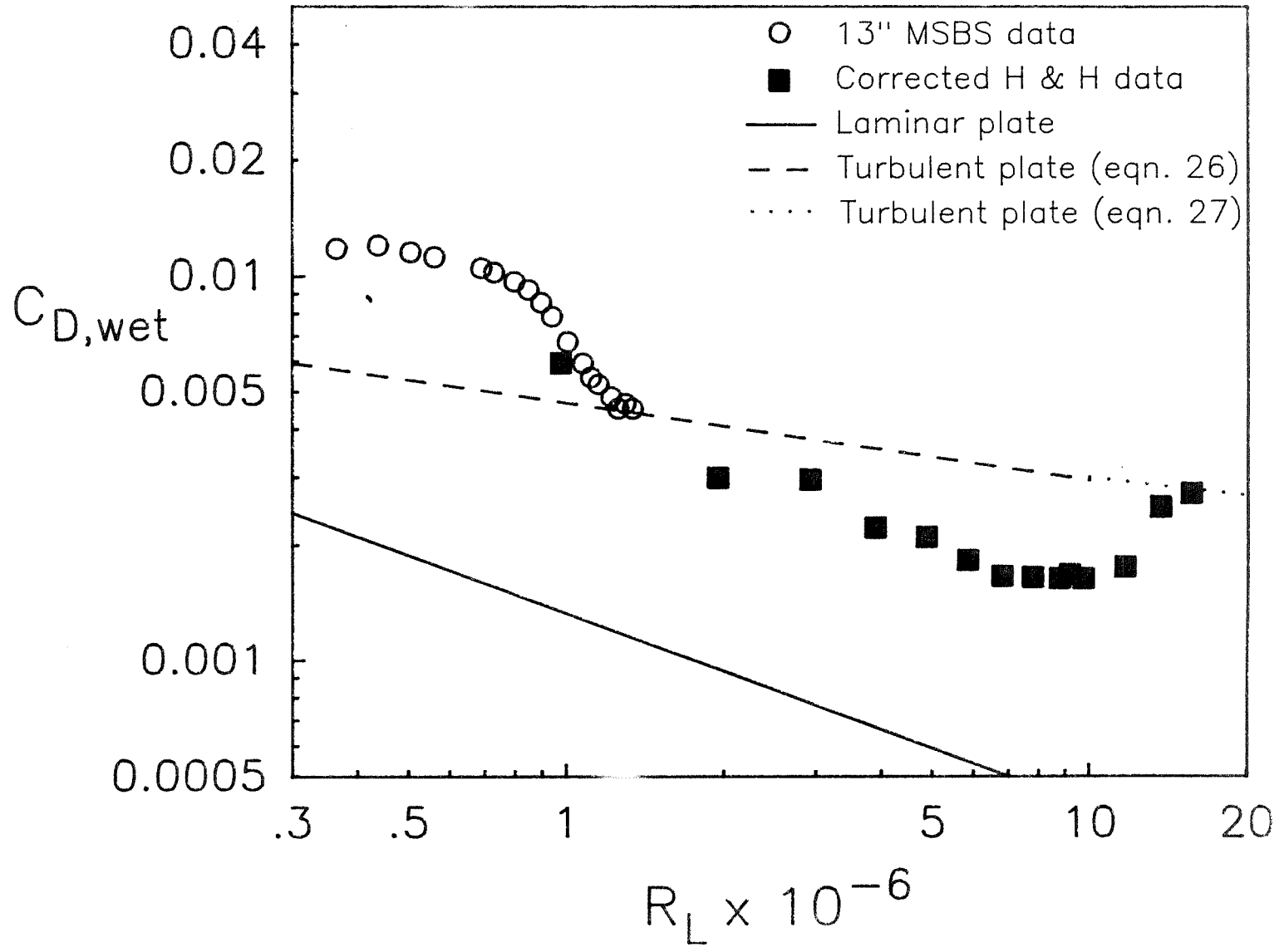

Figure 26. - Comparison of drag characteristics with Hansen & Hoyt data corrected for cavity pressure.

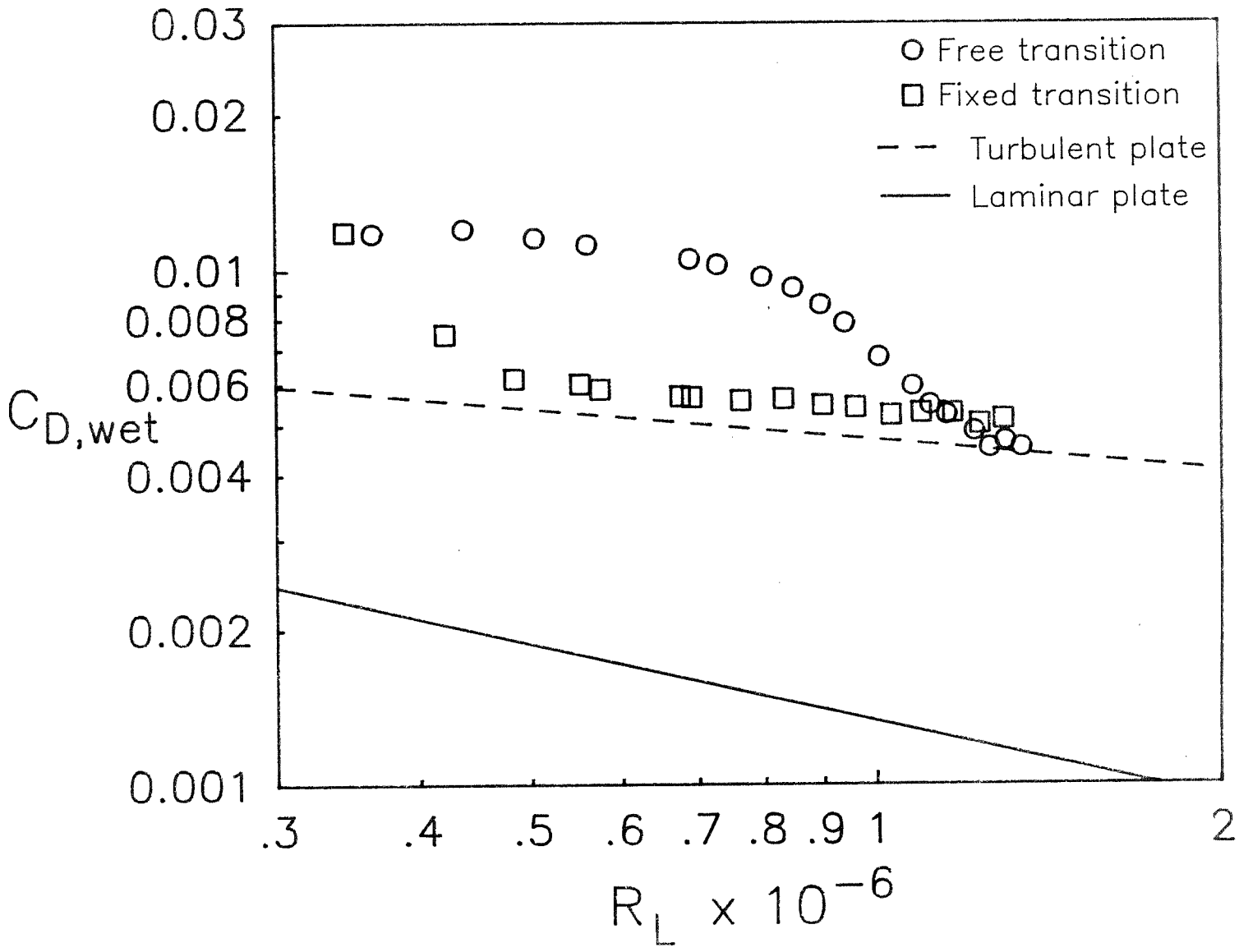

Figure 27. - Drag characteristics of laminar flow body. Comparison of fixed and free transition. Fixed at 17% station with number 60 grit.

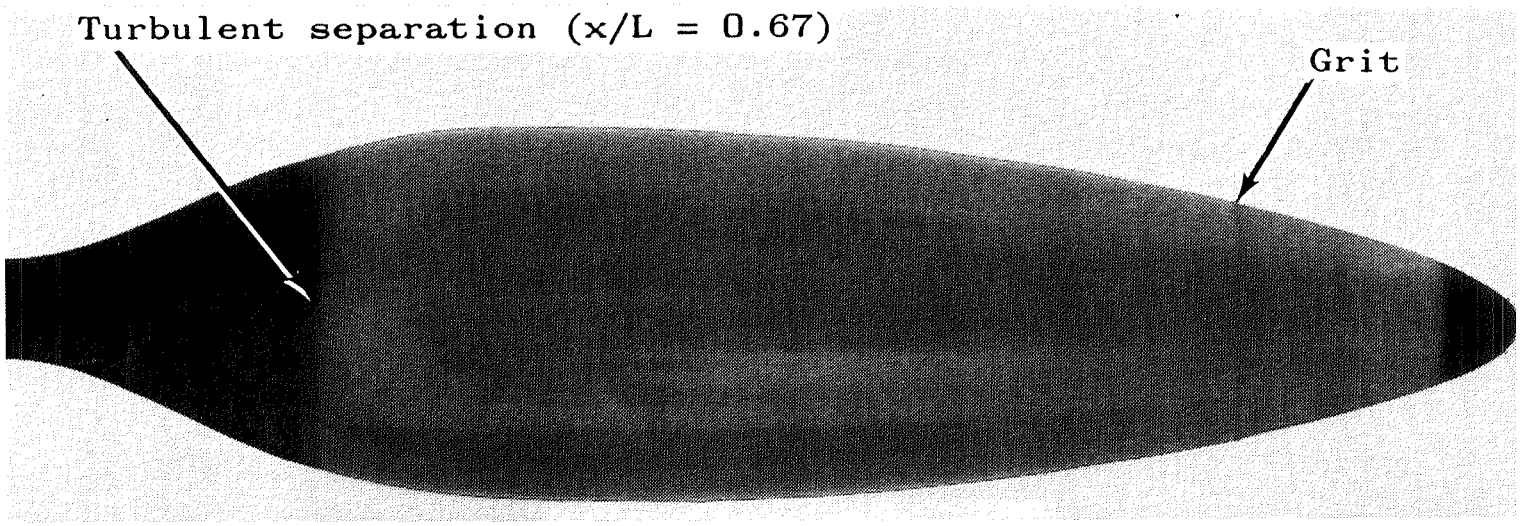

a) $R_L = 7.6 \times 10^5$

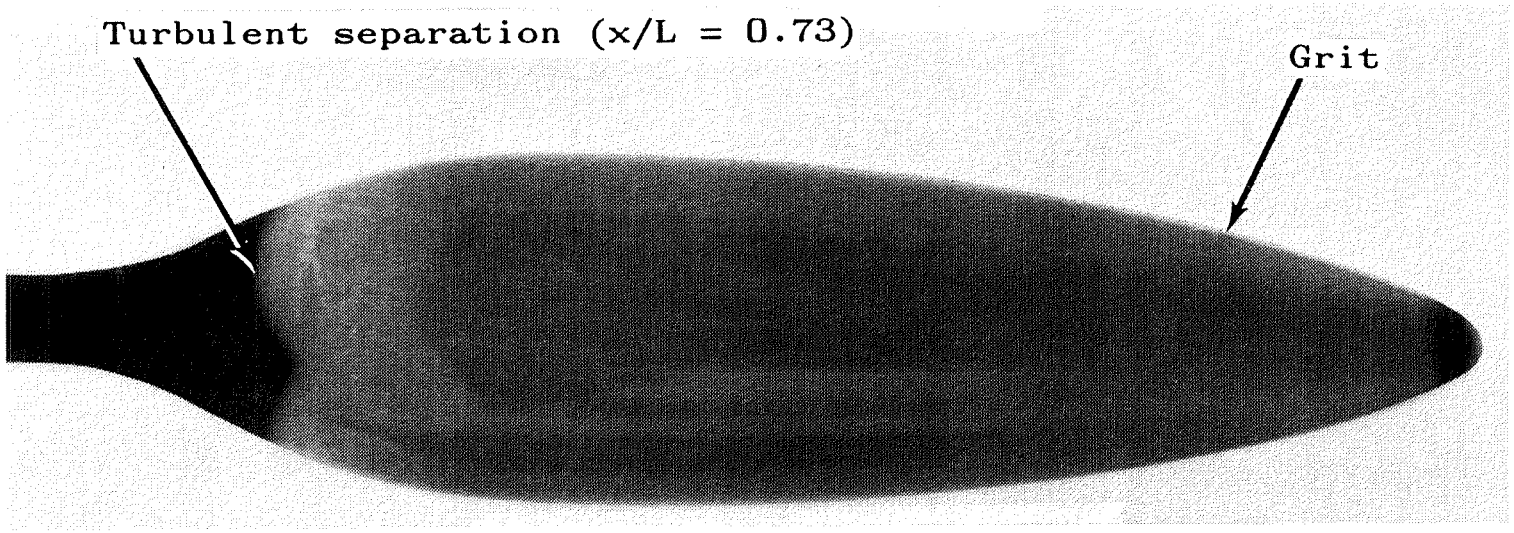

b) $R_L = 1.2 \times 10^6$

Figure 28. - Photographs of liquid crystal flow visualization for fixed transition at 17% station using number 60 grit. (†See footnote on page 21.)

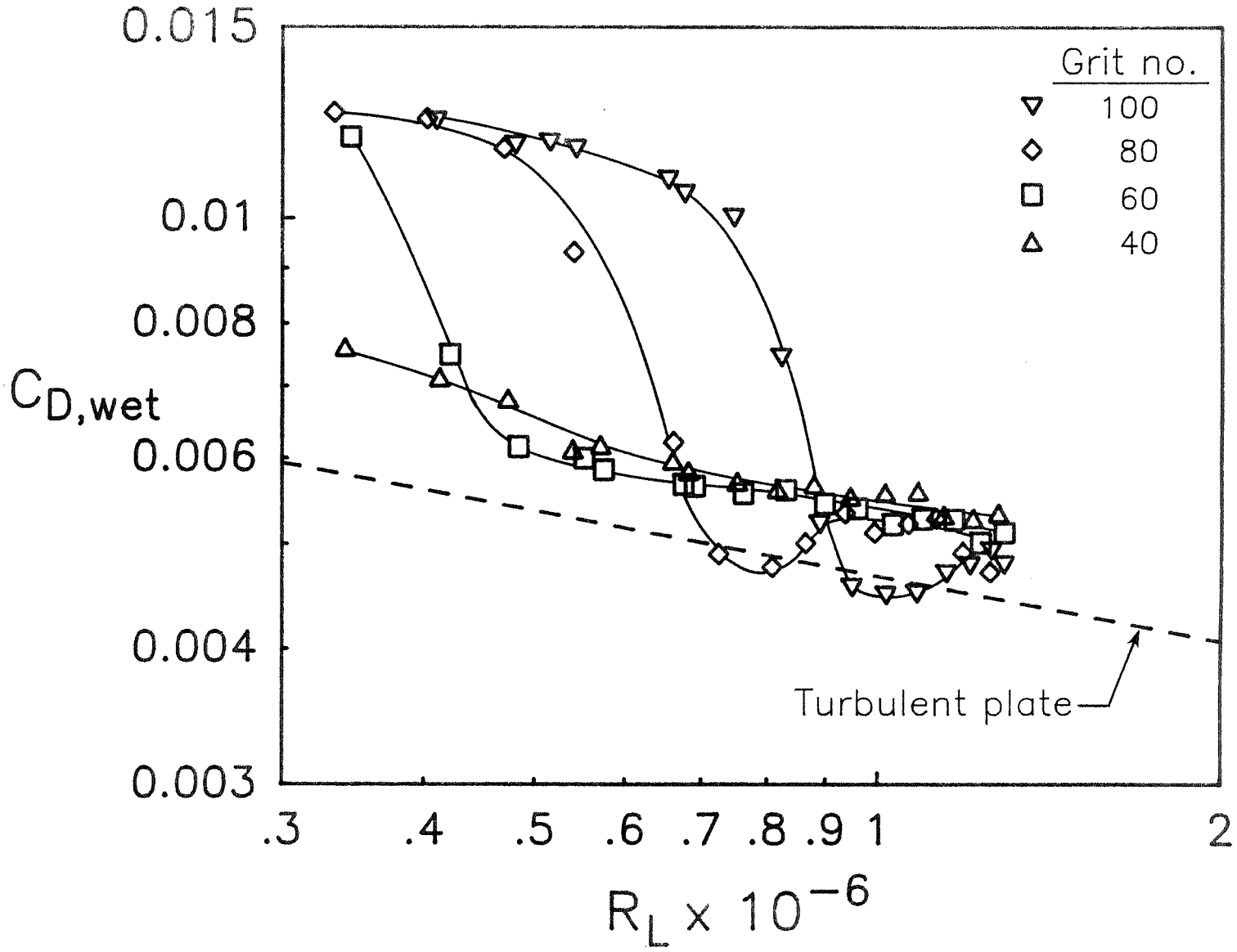

Figure 29. - Drag characteristics of laminar flow body. Fixed transition comparisons at 17% station using four different grit sizes.

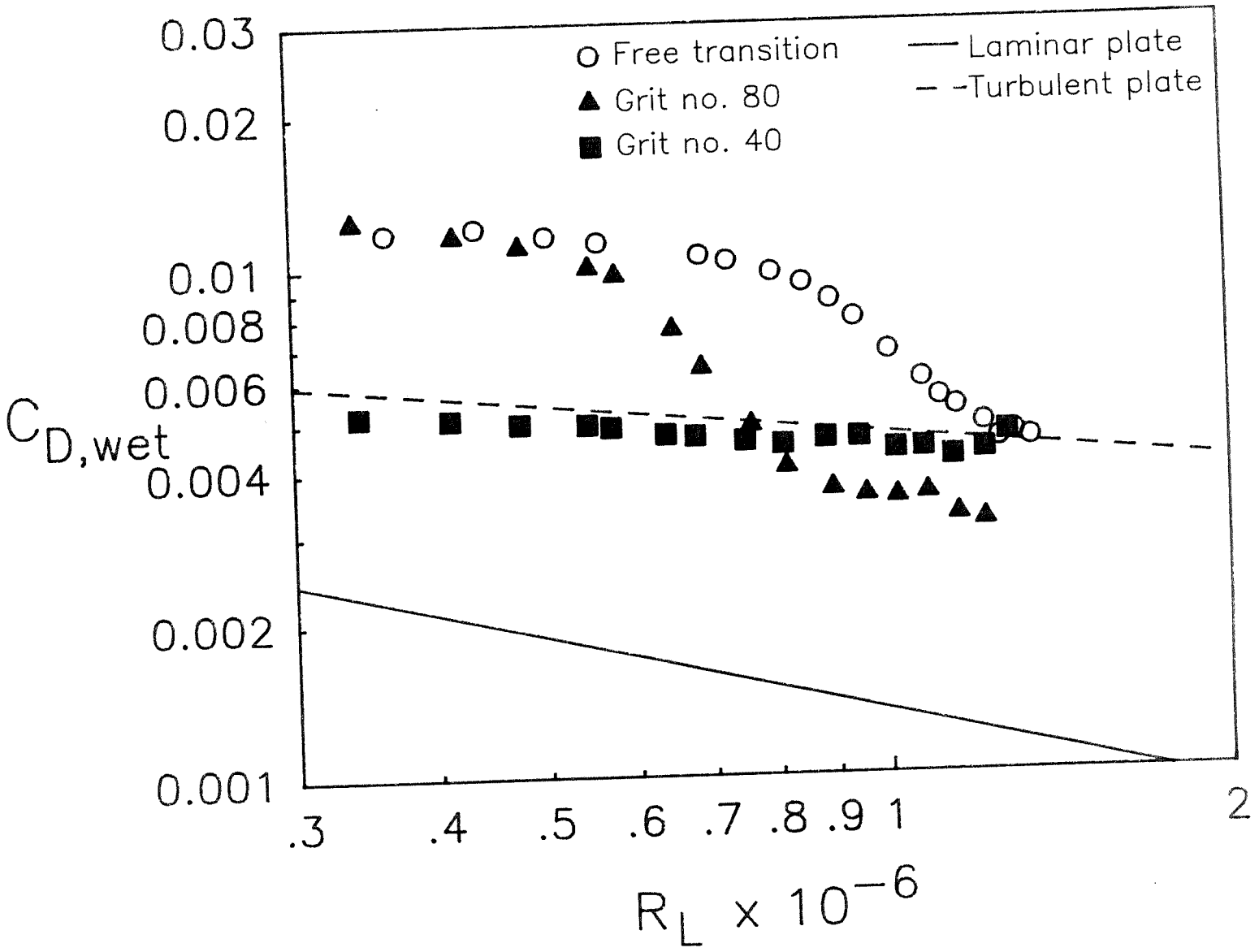

Figure 30. - Drag characteristics of laminar flow body. Comparison of fixed and free transition. Fixed at 50% station with both number 80 grit and number 40 grit.

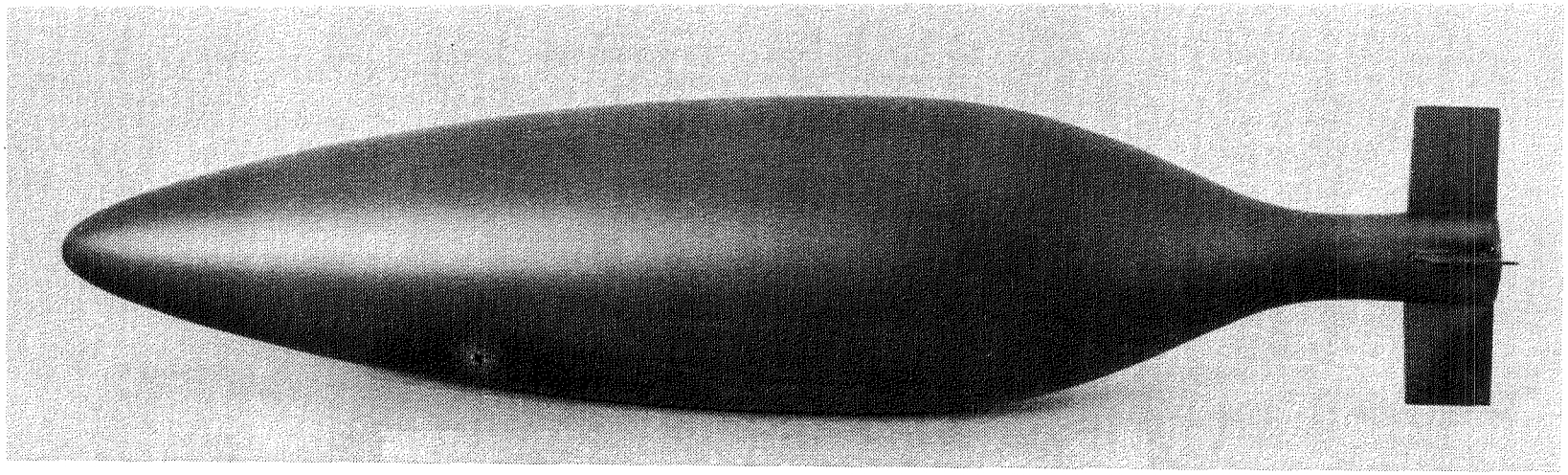

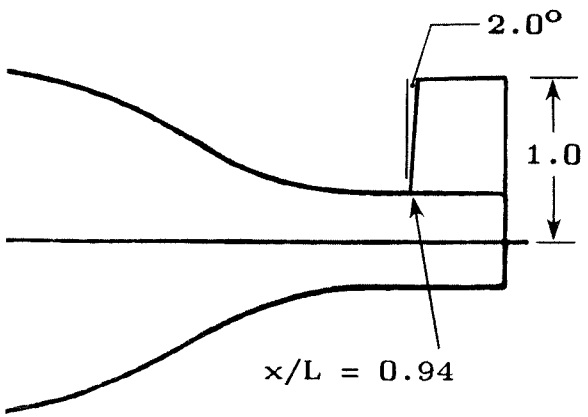

Figure 31. - Photograph and sketch of model with fins.
(Dimensions are in inches.)

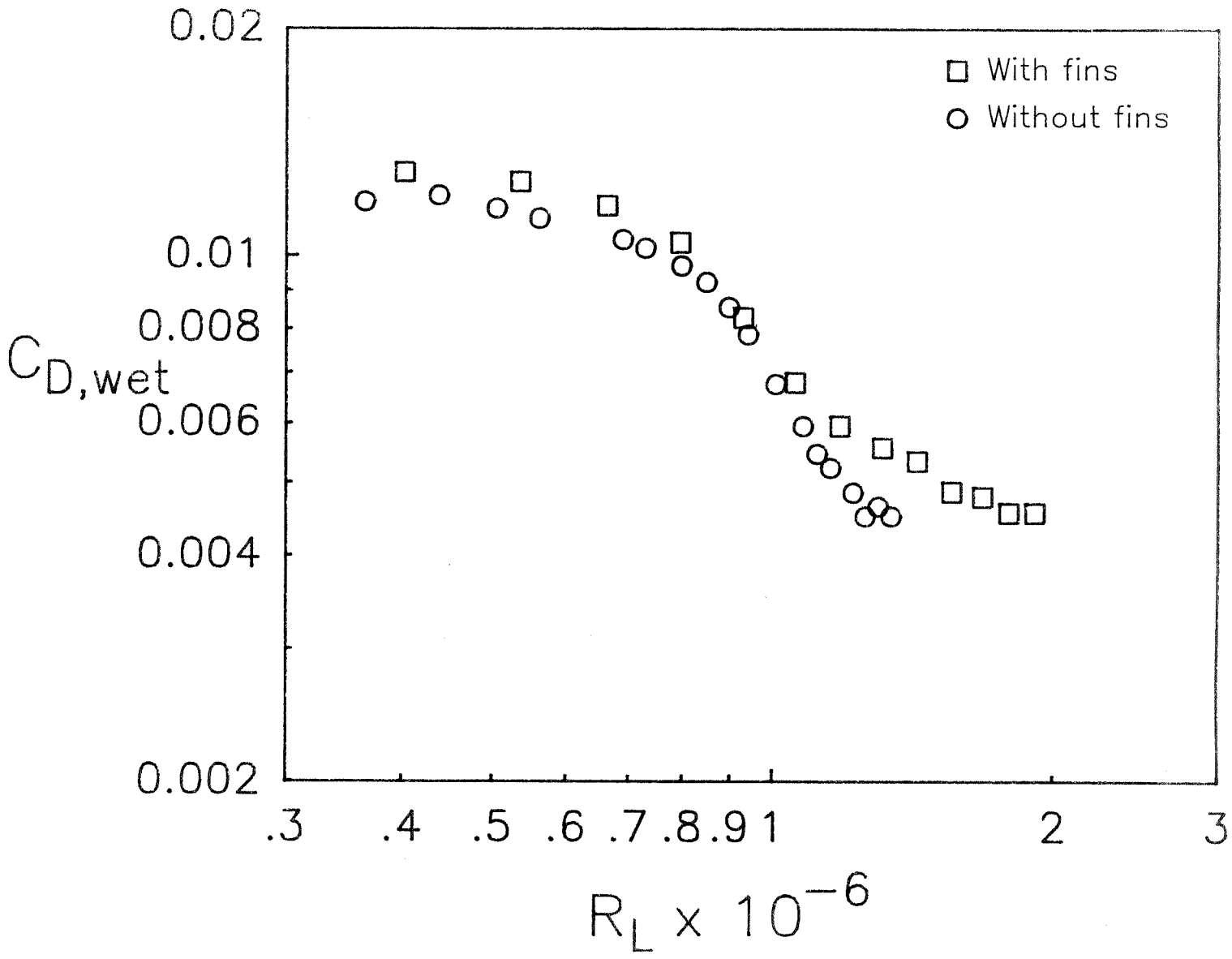

Figure 32. - Drag characteristics of laminar flow body. Comparison with and without fins.

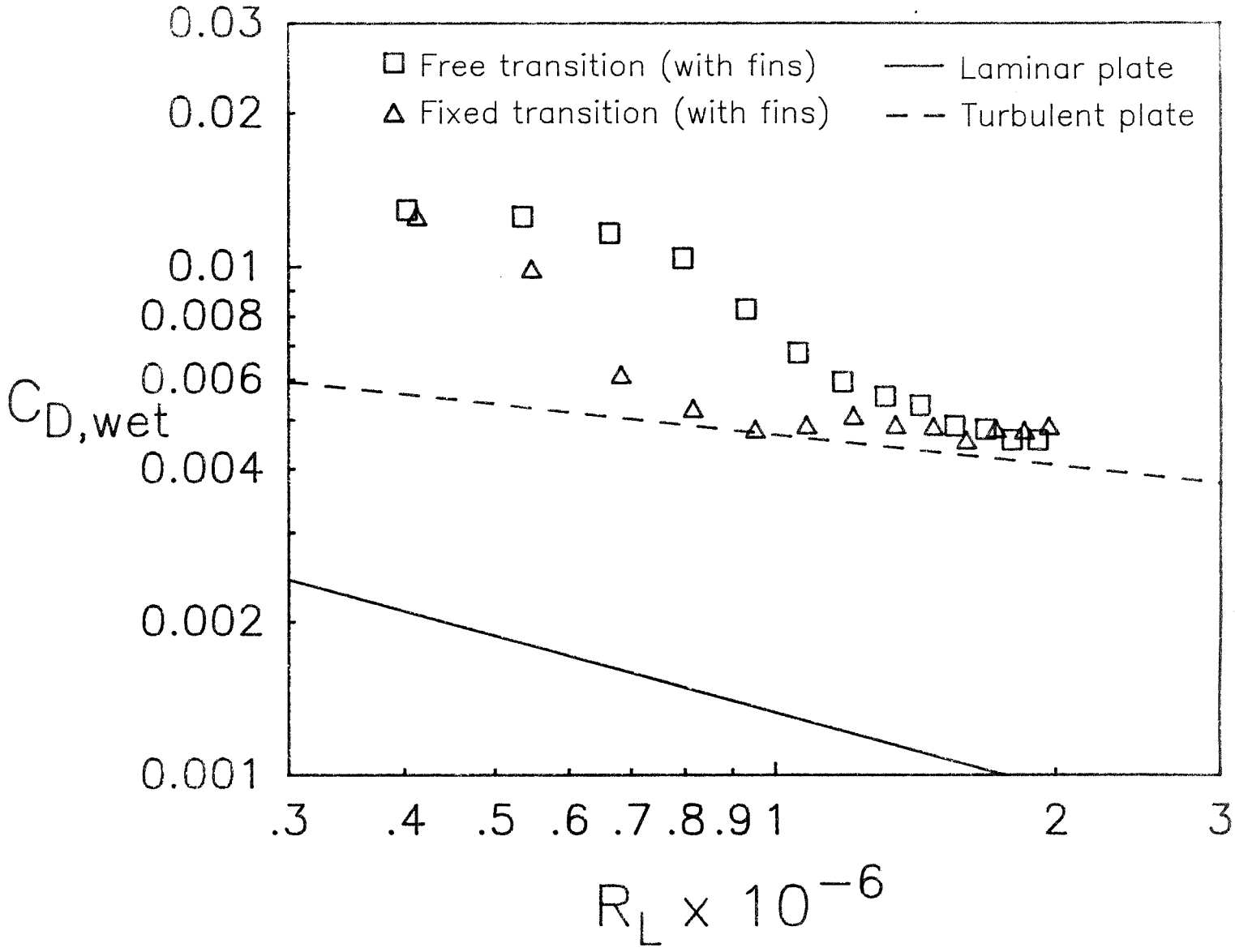

Figure 33. - Drag characteristics of laminar flow body. Comparison with fins for fixed and free transition. Fixed at 50% station with number 80 grit.

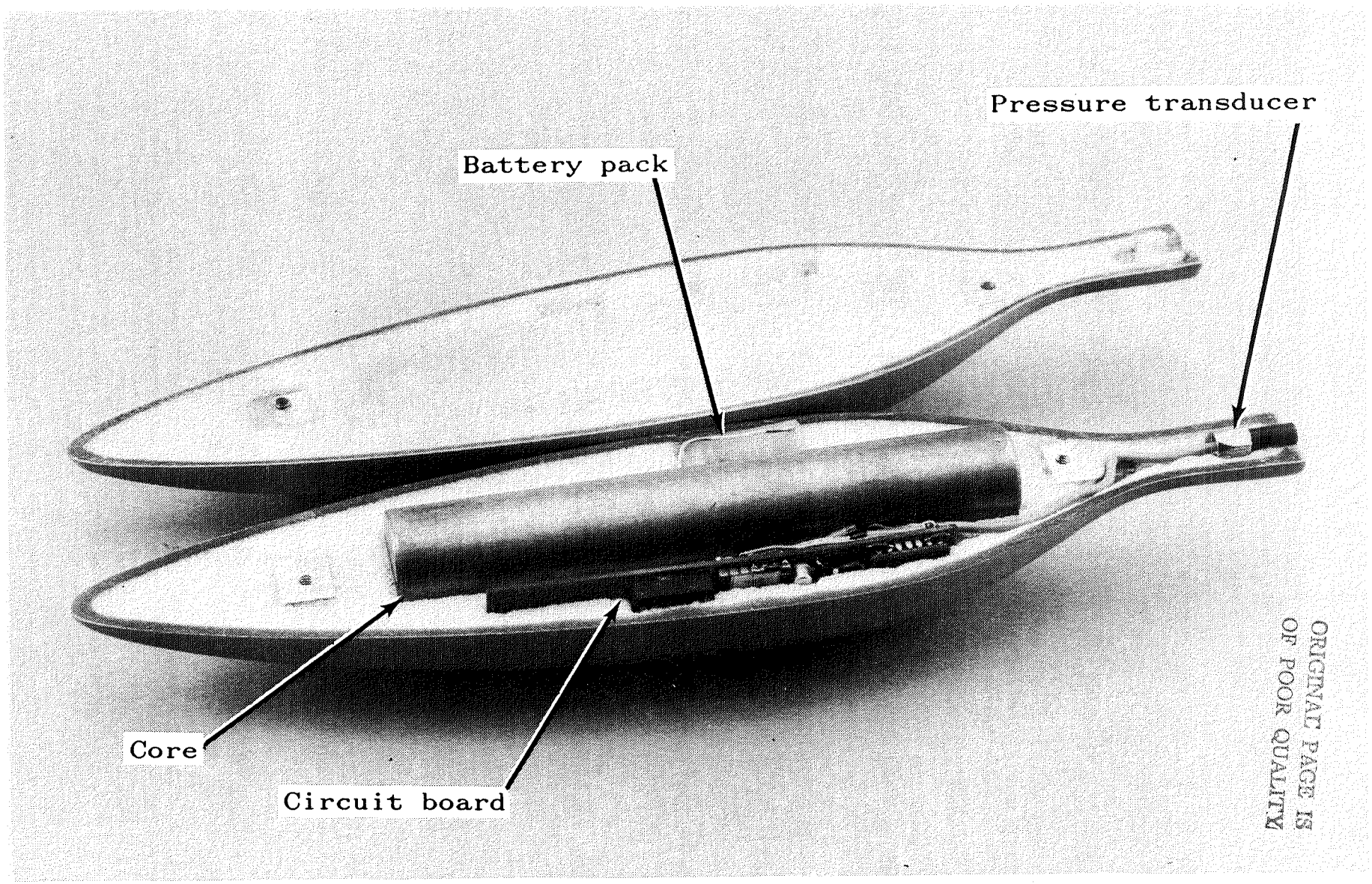

Figure 34. - Photograph of model with telemetry system installed.

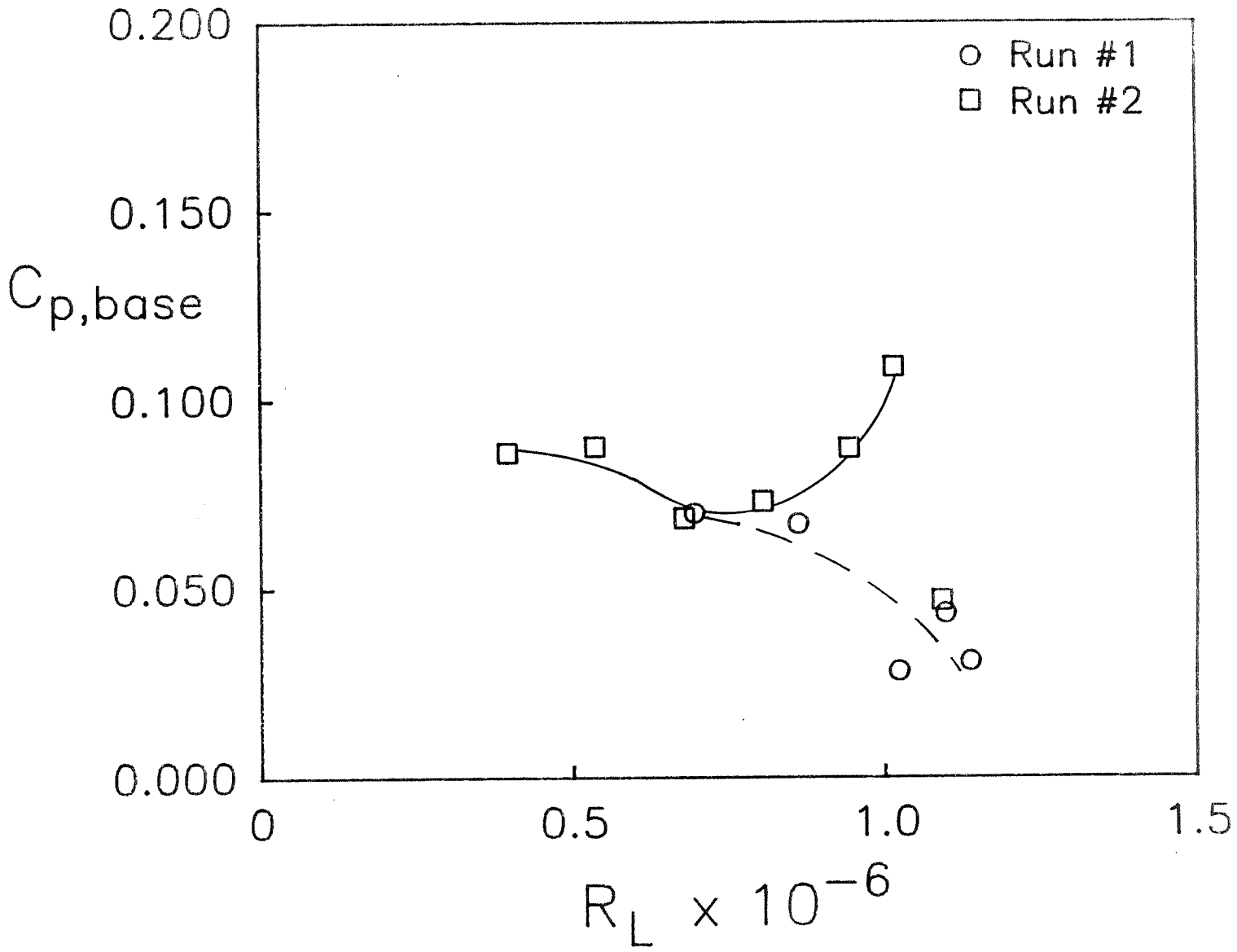

Figure 35. - Base pressure measurements for the laminar flow body.

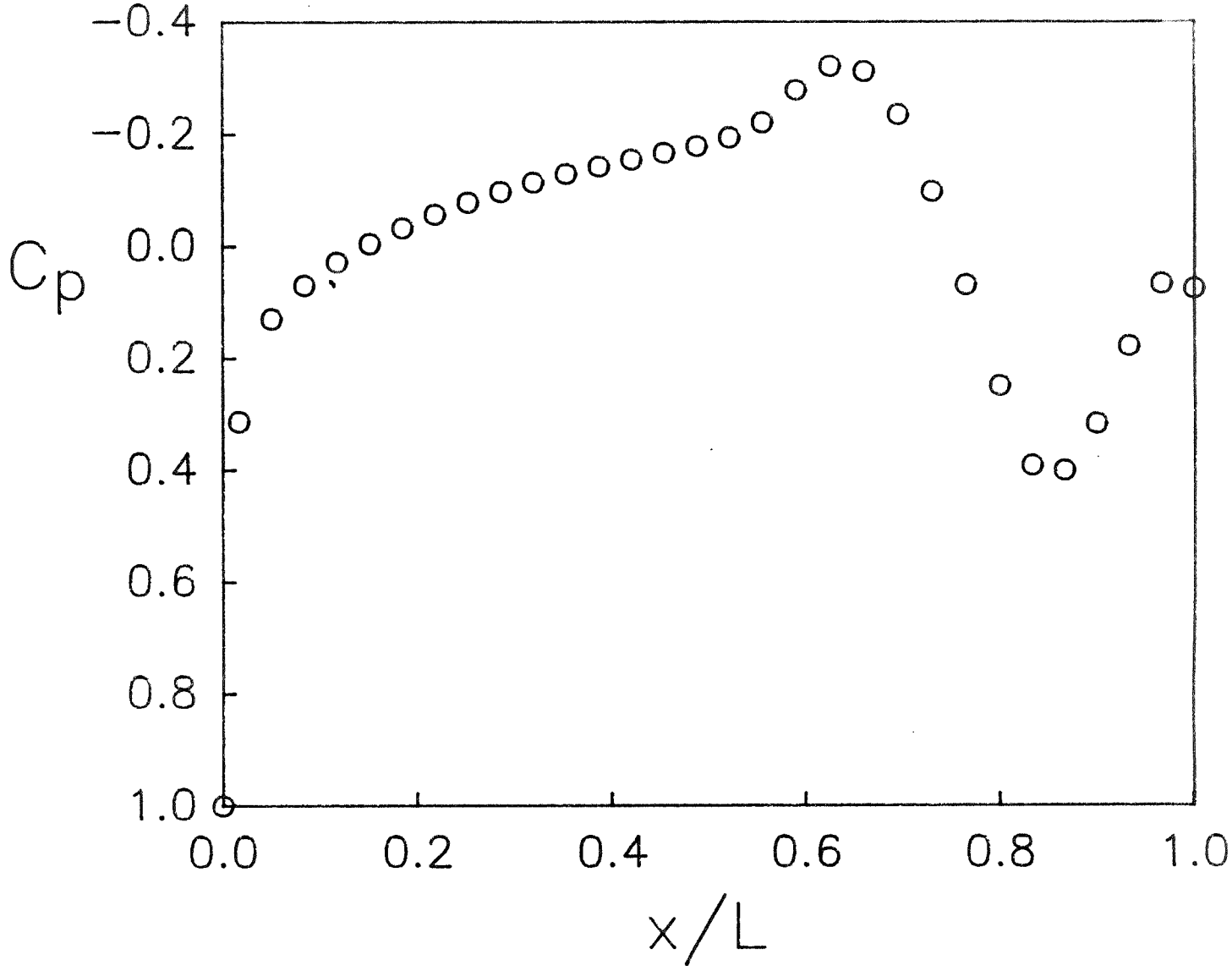

Figure 36. - Potential flow pressure distribution for laminar flow body from SANDRAG.

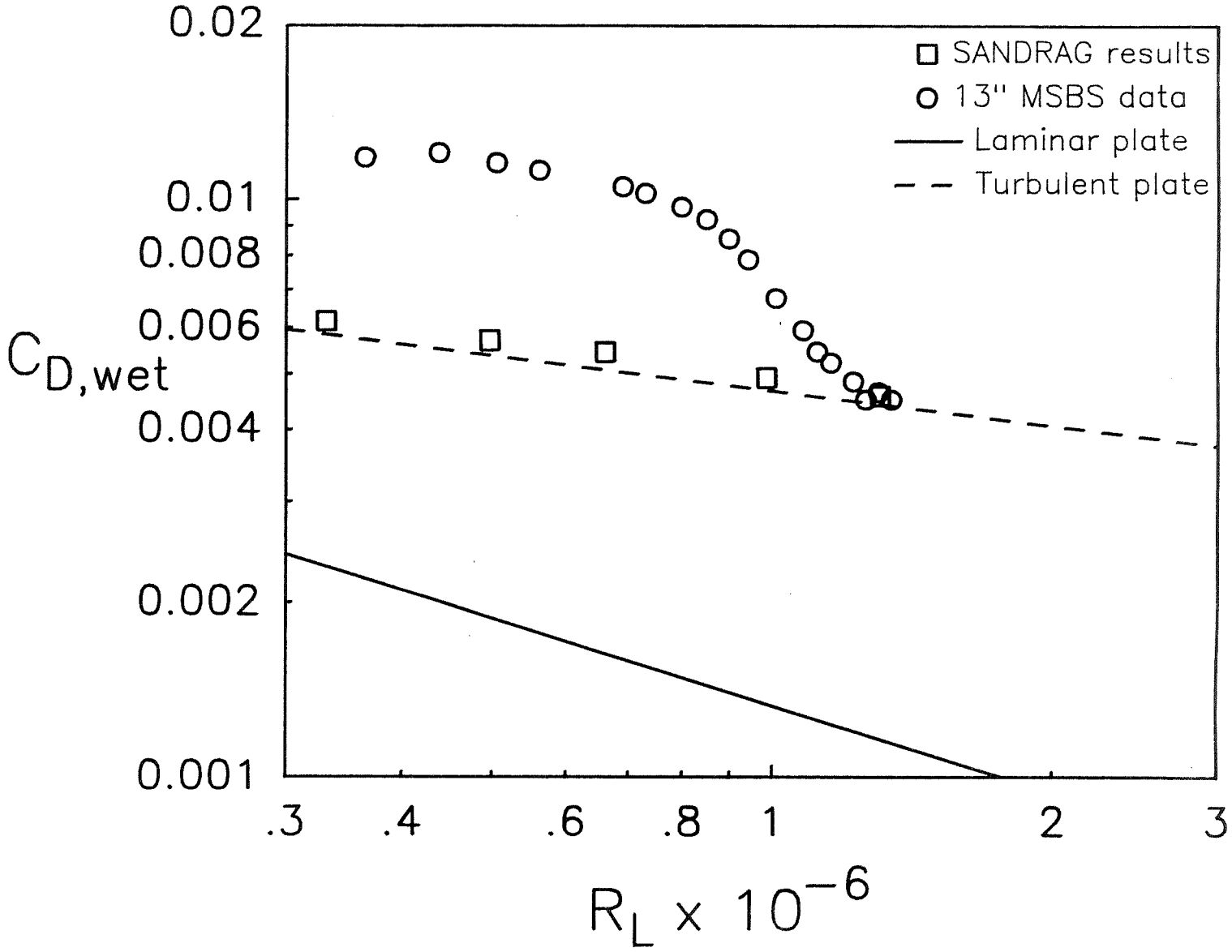

Figure 37. - Comparison of drag characteristics of laminar flow body with SANDRAG computational results. Free transition.

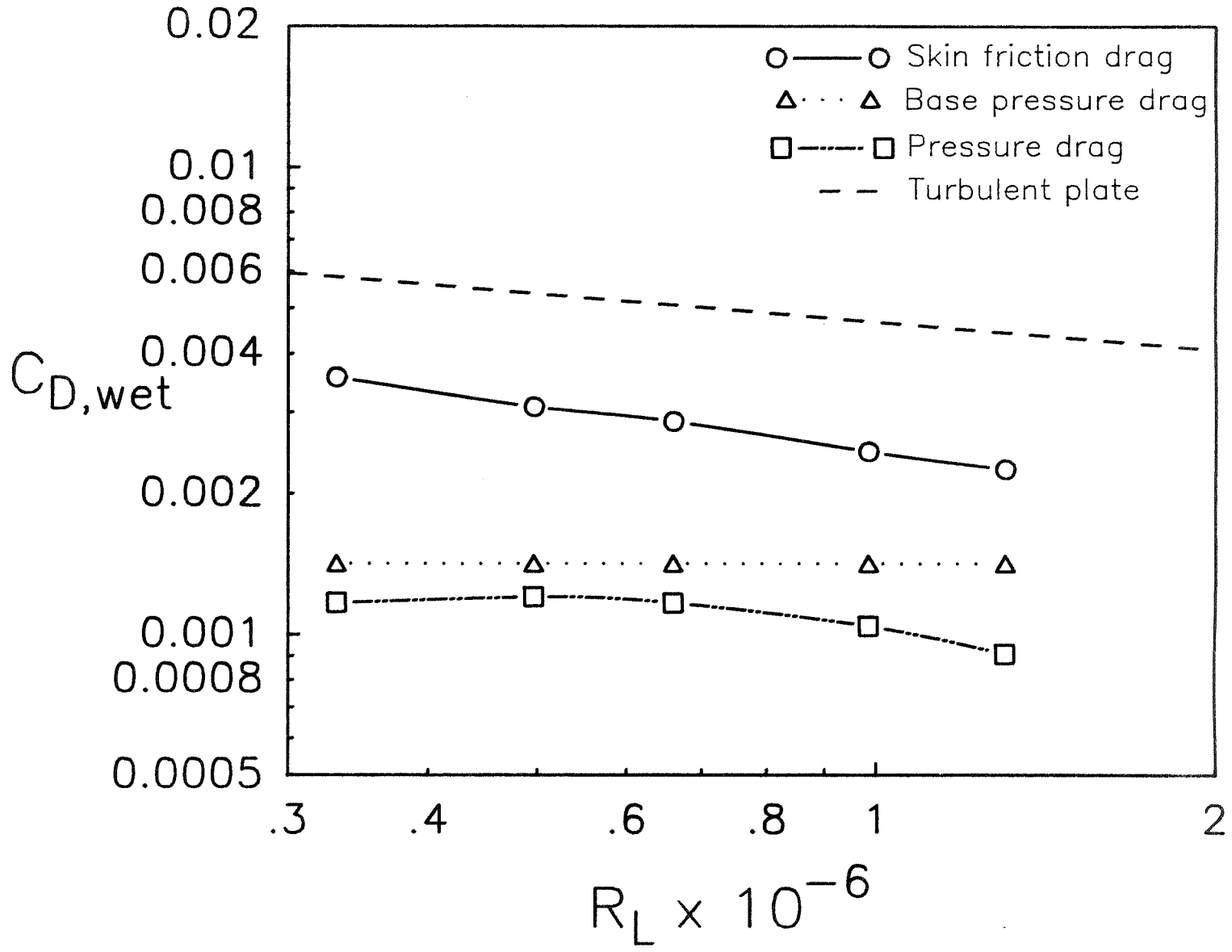

Figure 38. - Breakdown of SANDRAG drag components.

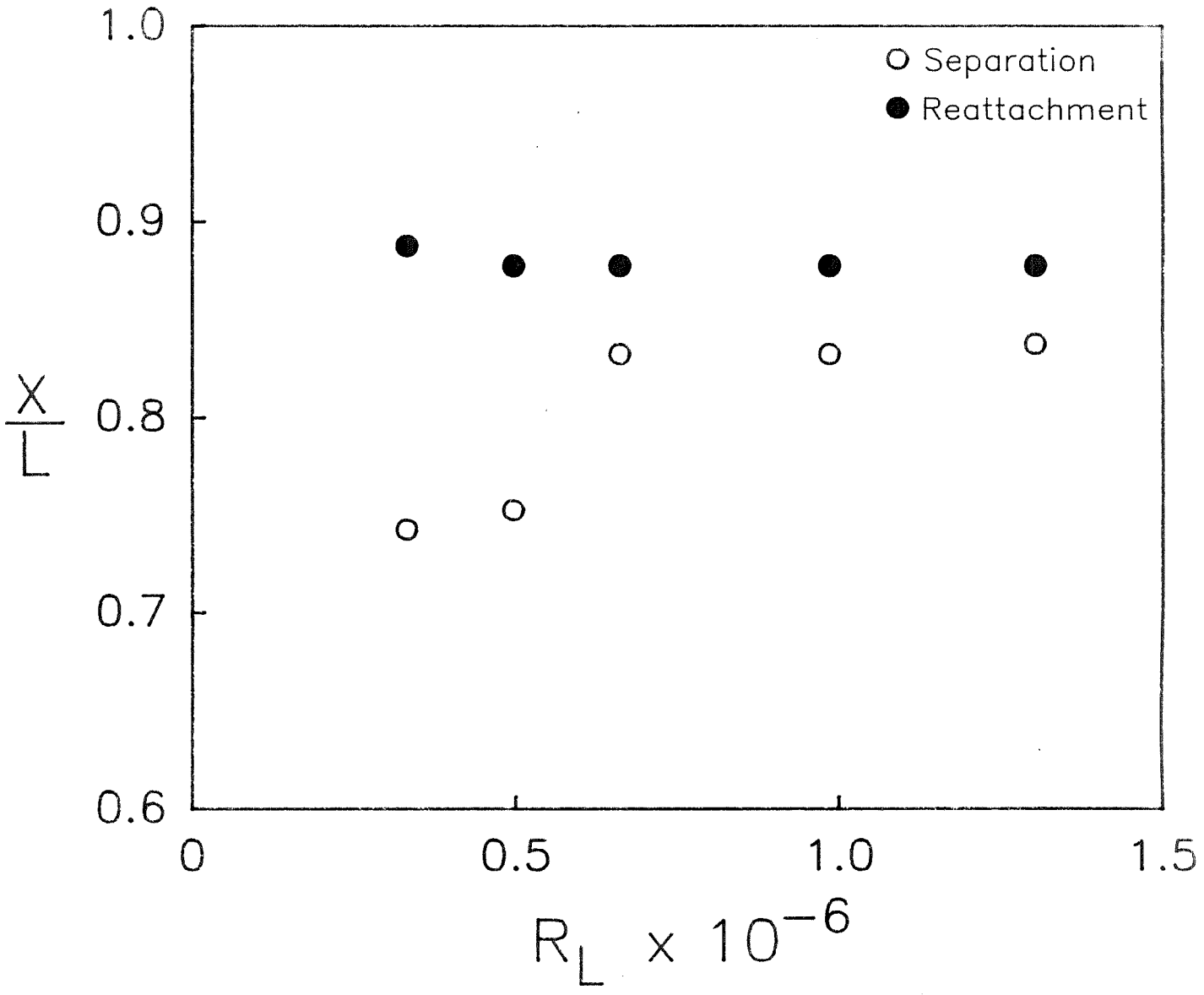

Figure 39. - Turbulent separation and reattachment points from SANDRAG.

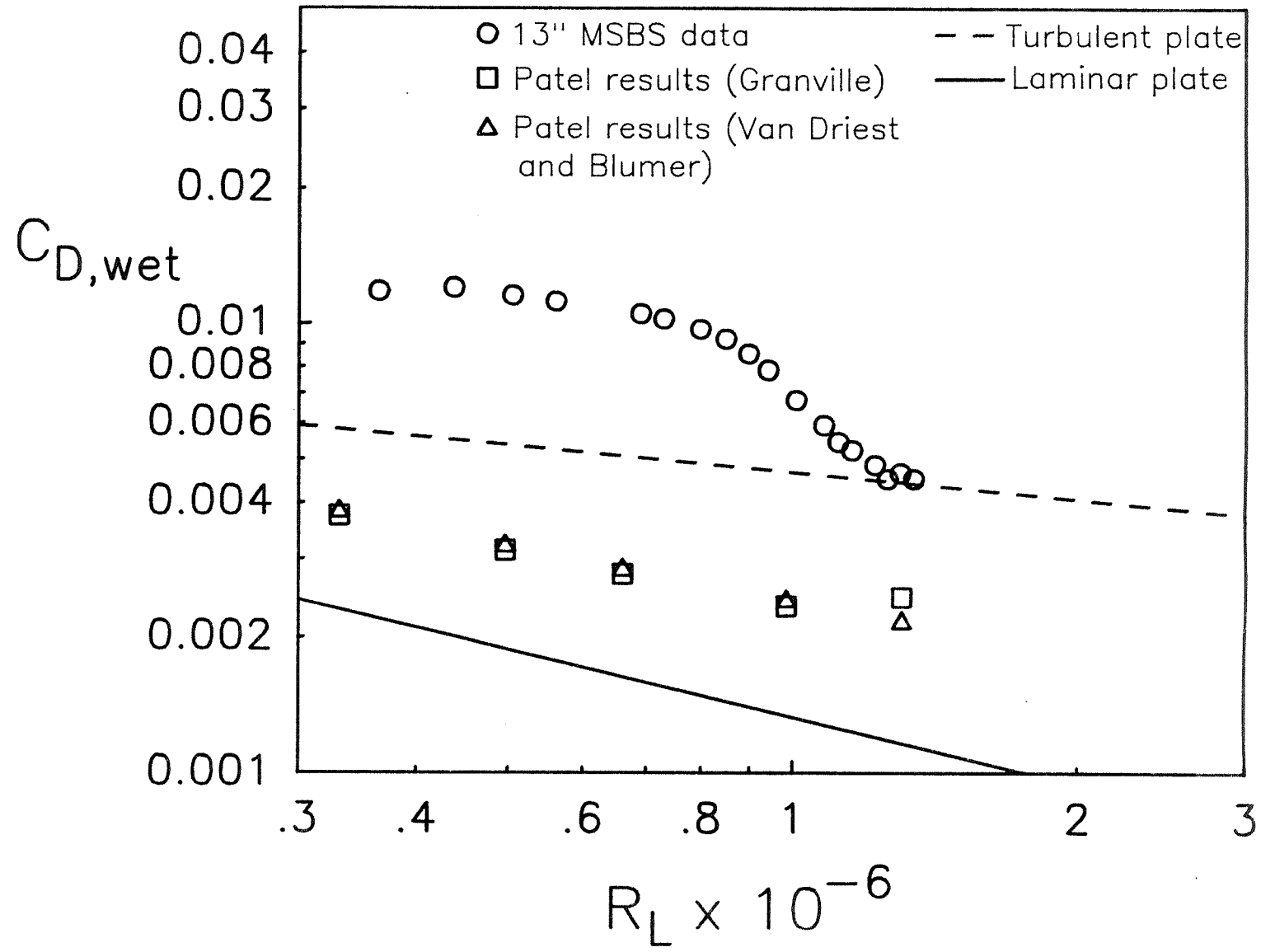

Figure 40. - Comparison of drag characteristics of laminar flow body with Nakayama and Patel computational results. Free transition.

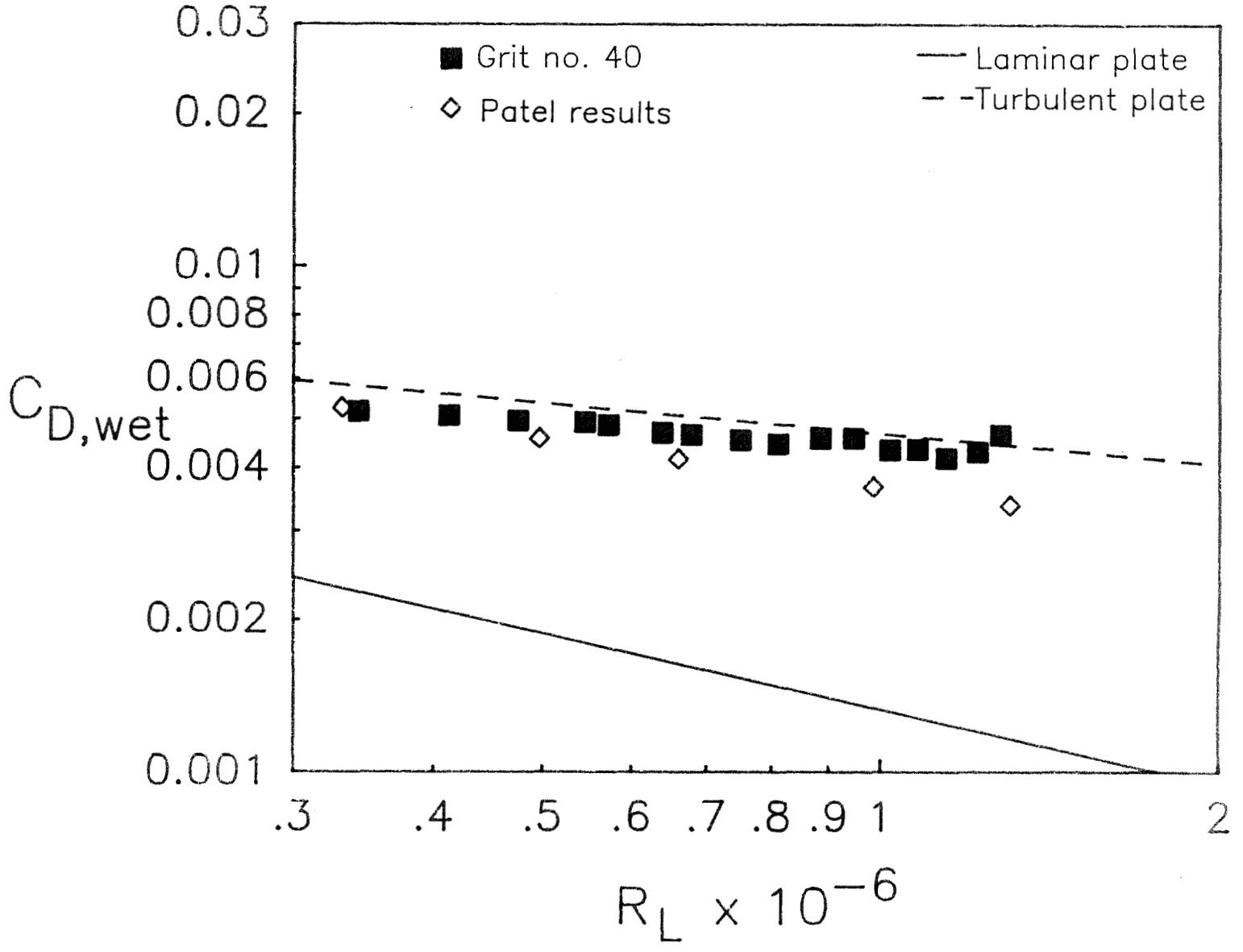

Figure 41. - Comparison of drag characteristics of laminar flow body with Nakayama and Patel computational results based on experimental transition location. Data is for fixed transition at 50% station with number 40 grit.

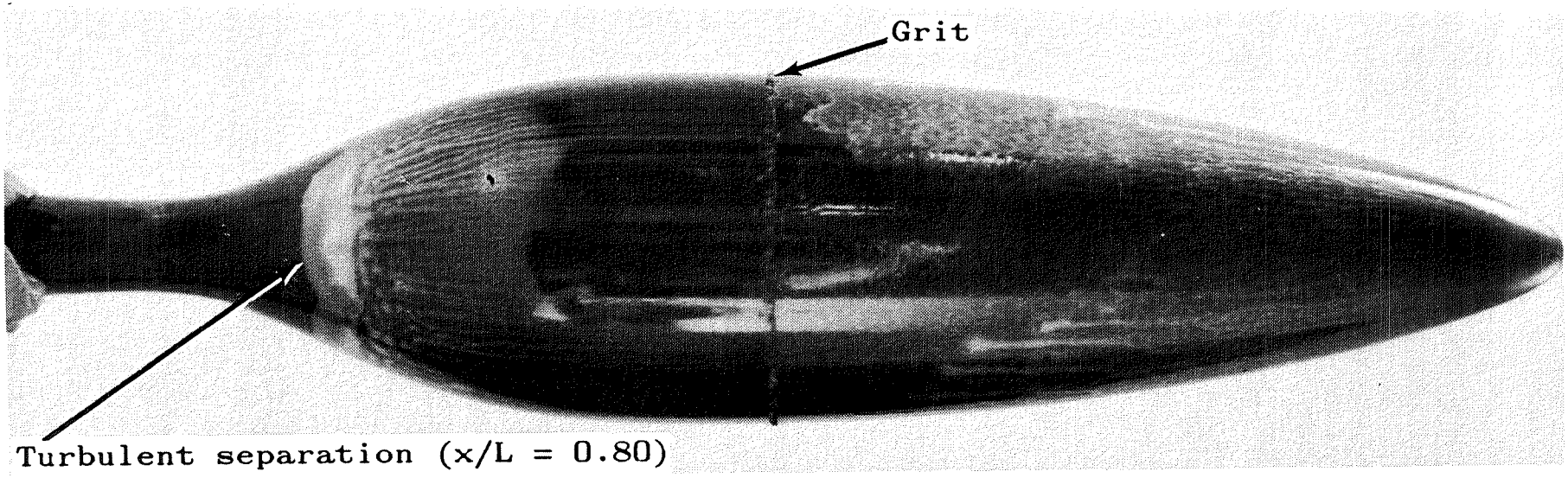

Figure 42. - Photograph of liquid crystal flow visualization for fixed transition at 50% station using number 40 grit.
$R_L = 1.1 \times 10^6$.